Predictability of Epileptic Seizures by Fusion of Scalp EEG and fMRI

Thesis submitted to Cardiff University in candidature for the degree of Doctor of Philosophy.

Min Jing

Centre of Digital Signal Processing
Cardiff University
2008

ProQuest LLC
789 East Eisenhower Parkway
P.O. Box 1346
Ann Arbor, MI 48106-1346

ABSTRACT

The systems for prediction of epileptic seizure investigated in recent years mainly rely on the traditional nonlinear analysis of the brain signals from intracranial electroencephalograph (EEG) recordings. The overall objective of this work focuses on investigation of the predictability of seizure from the scalp signals by applying effective blind source separation (BSS) techniques to scalp EEGs, in which the epileptic seizures are considered as independent components of the scalp EEGs. The ultimate goal of the work is to pave the way for epileptic seizure prediction from the scalp EEG. The main contributions of this research are summarized as follows.

Firstly, a novel constrained topographic independent component analysis (CTICA) algorithm is developed for the improved separation of the epileptic seizure signals. The related CTICA model is more suitable for brain signal separation due to the relaxation of the independence assumption, as the source signals geometrically close to each other are assumed to have some dependencies. By incorporating the spatial and frequency information of seizure signals as the constraint, CTICA achieves a better performance in separating the seizure signals in comparison with other conventional ICA methods.

Secondly, the predictability of seizure is investigated. The traditional method for quantification of the nonlinear dynamics of time se-

ries is employed to quantify the level of chaos of the estimated sources. The simultaneously recorded intracranial and scalp EEGs are used for the comparison of the results. The experiment results demonstrate that the separated seizure sources have a similar transition trend as those achieved from the intracranial EEGs.

Thirdly, simultaneously recorded EEG and functional Magnetic Resonance Imaging (fMRI) is studied in order to validate the activated area of the brain related to the seizure sources. An effective method to remove the fMRI scanner artifacts from the scalp EEG is established by applying the blind source extraction (BSE) algorithm. The results show that the effect of fMRI scanner artifacts has been reduced in scalp EEG recordings.

Finally, a data driven model, spatial ICA (SICA) subject to EEG as the temporal constraint is proposed in order to detect the Blood Oxygen-Level Dependence (BOLD) from the seizure fMRI. In contrast to the popular model driven method General Linear Model (GLM), SICA does not rely on any predefined hemodynamic response function. It is based on the fact that brain areas executing different tasks are spatially independent. Therefore SICA works perfectly for non-event-related fMRI analysis such as seizure fMRI. By incorporating the temporal information existing within the EEG as the constraint, the superiority of the proposed constrained SICA is validated in terms of better algorithm convergence and a higher correlation between the time courses of the component and the seizure EEG signals as compared to SICA.

ACKNOWLEDGEMENTS

First, I would like to give my special thanks to my supervisor Dr. Saeid Sanei for all kinds of support, invaluable guidance and continuous encouragement throughout my PhD study. I also greatly appreciate Prof. Jonathan Chambers and Prof. Kenneth Harris for their enthusiastic support and help, and Prof. Barrie Jervis for insightful advice for the research work.

Second, I am extremely grateful to all my friends for their sincere care and support. Special thanks to John Li, Richard Shea, Chris Chapman and Lay Ong, for always being there for me, sharing all ups and downs, listening to me, encouraging and giving advice, and most important, always believing in me. I also thank all my colleagues in the Centre of Digital Signal Processing, especially Kianoush Nazarpour, Jen-Lung Lo, Mansoureh Ghodsi and Andrew Aubrey for their very kind help and encouragement.

Finally, I would like to give my greatest thanks to my family for their unconditional love and continuous support. And thanks to the universe which always takes care of me and delivers all kinds of support and opportunities when I need them. The inspiration I have received from it will motivate me to keep striving for all dreams till the day when all of them come true.

PUBLICATIONS

Journal Papers

- **M. Jing** and S. Sanei, "A Novel Constrained Topographic ICA for Separation of Epileptic Seizure Signals," *Journal of Computational Intelligence and Neuroscience*, vol. 2007, issue 1, pp. 15-22, 2007.

- L. Spyrou, **M. Jing**, S. Sanei and A. Sumich, "Separation and Localisation of P300 Sources and their Subcomponents Using Constrained Blind Source Separation," *EURASIP Journal on Applied Signal Processing*, vol. 2007, pp. 1-10, 2007.

Conference Papers

- **M. Jing** and S. Sanei, "A novel ICA approach for separation of seizure BOLD from fMRI, constrained by the simultaneously recorded EEG signals," Accepted by The 16th *European Signal Processing Conference (EUSIPCO)* 2008, Lausanne, Switzerland.

- **M. Jing** and S. Sanei, "Seizure Signals Separation Using Constrained Topographic Blind Source Separation," The 15th *European Signal Processing Conference (EUSIPCO)* 2007, September, Poland.

- **M. Jing** and S. Sanei, "Scanner Artifact Removal in Simultaneous EEG-fMRI for Epileptic Seizure Prediction," The 18th *International Conference on Pattern Recognition (ICPR)* 2006, August, Hongkong.

- S. Sanei and **M. Jing**, "Simultaneous EEG-fMRI study: A Blind Approach for Mitigation of Scanner Artifact in the EEGs," *World Congress on Medical Physics and Biomedical Engineering* 2006, Aug.27-Sep.1, 2006, Seoul, South Korea.

- **M. Jing**, S. Sanei, J. Corsini and G. Alarcon, "Incorporating BSS to Epileptic Seizure Predictability Measure from Scalp EEG," The 27th Annual International Conference of the IEEE *Engineering in Medicine and Biology Society (EMBS)* 2005, September, Shanghai, China.

LIST OF ACRONYMS

BCG	Ballistocardiogram
BOLD	Blood Oxygen Level Dependence
BSS	Blind Source Separation
BSE	Blind Source Extraction
ECG	Electrocardiogram
EEG	Electroencephalography
EVD	Eigenvalue Decomposition
fMRI	Functional Magnetic Resonance Imaging
GLM	General Linear Model
HOS	High Order Statistics
HRF	Hemadynamic Response Function
IC	Independent Component
ICA	Independent Component Analysis
ISA	Independent Subspace Analysis
JADE	Joint Approximate Diagonalization of Eigenmatrices
LMS	Least Mean Square
MEG	Magnetoencephalography
MLE	Maximum Likelihood Estimation
MI	Mutual Information

MIP	Maximum Intensity Projection
MRI	Magnetic Resonance Imaging
NMR	Nuclear Magnetic Resonance
PDF	Probability Density Function
PET	Positron Emission Tomography
RT	Repeat Time
ROI	Region of Interest
SIR	Signal to Interference Ratio
SICA	Spatial Independent Component Analysis
SOBI	Second Order Blind Identification
SPM	Statistical Parametric Mapping
STLmax	Short-term Largest Lyapunov Exponent
SVD	Singular Value Decomposition
SVM	Support Vector Machine
TICA	Topographic Independent Component Analysis

LIST OF SYMBOLS

$\lvert\cdot\rvert$	Absolute value
$\lVert\cdot\rVert_2$	Euclidean norm
$\lVert\cdot\rVert_F$	Frobenius norm
$(\cdot)^H$	Hermitian transpose
$(\cdot)^T$	Transpose operation
$(\cdot)^\dagger$	Pseudo-inverse
Λ	Diagonal matrix
$det(\cdot)$	Determinant of a matrix
$E\{\cdot\}$	Expectation operator
$cor(\cdot)$	Correlation
$cov(\cdot)$	Covariance
$cum(\cdot)$	Cumulant
$kur(\cdot)$	Kurtosis
$\Theta(\cdot)$	Heaviside step function
$var(\cdot)$	Variance
∇	Gradient operator
$\mathbf{S}$	Source matrix
$\mathbf{W}$	Estimated unmixing matrix
$\mathbf{X}$	Input data matrix
$\mathbf{Y}$	Estimated output data matrix

CONTENTS

List of Figures

List of Tables

Chapter 1

INTRODUCTION

1.1 Overview

The prediction of epileptic seizures has been investigated in recent years. Most of the developed methods rely on the analysis of brain signals which are obtained from inside the brain. Establishment of a warning system that can predict the onset of seizure based on noninvasive recording of brain signals has attracted much attention recently. The research presented in this thesis investigates the predictability of epileptic seizure from noninvasively recorded data of an epileptic brain by applying effective blind source separation (BSS) techniques, thus paving the way for epileptic seizure prediction.

This chapter mainly focuses on an introduction to the physiological background knowledge and BSS. In the first section, the structure and function of the human brain are introduced and a brief review of epileptic seizure is given. The most widely used brain function monitoring modality, i.e. Electroencephalography (EEG), is introduced. In addition, other modalities such as Magnetoencephalography (MEG) and functional Magnetic Resonance Imaging (fMRI) are briefly introduced. The second section gives an overview of blind source separation techniques including the description of the problem, the principles of

estimation and a survey of BSS algorithms. The structure of the thesis is described in the final section, in which the contributions in each chapter are addressed.

1.2 Physiological Background

1.2.1 Human Brain

The human brain consists of three main parts, the cerebrum, the cerebellum and the brain stem. The two hemispheres of the cerebellum are separated by the longitudinal fissure across which there is a large connective band of fibres called corpus callosum. The outer surfaces of the cerebral hemispheres are composed of nerve cells (neurons) that form the cerebral cortex. These surfaces are separated into regions by a number of fissures. Beneath the cortex, nerve fibres lead to other parts of the brain and body. Because of their colour, the regions composed of neurons, which include the cerebral cortex, are known as grey matter; fibrous tissue is called white matter [3].

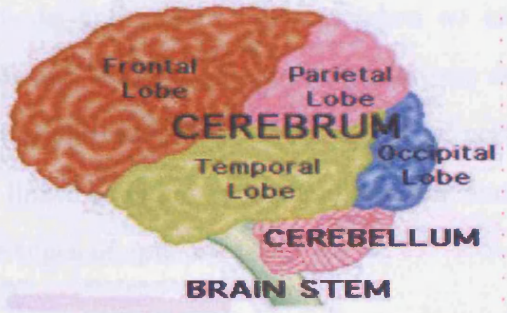

Figure 1.1. Lateral view of the left cerebral hemisphere [1].

The brain is divided into regions that control some specific functions. Mainly, different regions (as illustrated in Fig. 1.1) are respon-

sible for particular tasks. For example, vision information is processed by the occipital lobes, and hearing and language are handled by the temporal lobe. Sensation and movement are in the nearby areas which belong to the parietal lobe. Reading function is located on the boundary area where vision and hearing areas interact. The right hemisphere deals with visual information but the left one does more analytical work; therefore, information is obtained from the right hemisphere and analyzed in the left part [3]. When someone has a brain injury, a certain region might be damaged, and therefore the related function is affected. But other undamaged regions may still function properly. For example, a patient with dyslexia can hear and see things, but has difficulties to read and understand letters.

In a simple way, the brain can be considered as an electrical and chemical machine. Neurons "communicate" with each other by means of electrical or chemical activities. The electrical activity means that information transfer from neuron to neuron via a small electrical charge which is generated by billions of axons. The information can also be transmitted by neurotransmitters. Neurotransmitters are chemicals stored in the axons and can be released when an electrical impulse reaches to the axons. The level of neurotransmitters can be influenced by nervous system diseases. Loss or imbalance of certain neurotransmitters may be linked to brain system malfunction, such as Parkinson's disease or some types of epilepsy [2].

1.2.2 Epileptic Seizure

Epilepsy is a disease known from ancient times and the name is derived from the Greek word "Epilepsia" [4]. Epilepsy covers a group of re-

lated disorders characterized by a tendency for recurrent seizures. The seizures are due to a sudden development of synchronous neuronal firing in the cerebral cortex. The cause of epilepsy still remains unknown. A large number of possible causes can include genetic abnormalities, developmental anomalies, febrile convulsions, central nervous system infections, hypoxia, and tumors [4].

Different types of epilepsy have been discovered. In terms of diagnosis, an epilepsy is usually referred to as idiopathic, cryptogenic, symptomatic, generalized, focal, or partial [46]. The first three classify the epilepsy based on the following reasons. Idiopathic means there is no apparent cause but perhaps a family history. Cryptogenic means there is a likely cause but it has not been identified. Symptomatic means that a cause has been identified. The other three mainly consider whether the whole brain or just part of it is involved. Generalized means that the seizures involve the whole brain at once. Focal or partial means that the seizure originates from one area of the brain.

Different treatments are often considered for different types of epilepsy. For example, the idiopathic generalized epilepsy has no nervous system abnormalities and usually it can be treated by medication. On the other hand, symptomatic partial (or focal) epilepsy, which is the most common type of epilepsy that begins in adulthood, cannot be treated by medication. This type of epilepsy is caused by a localized abnormality of the brain, which may be successfully treated with surgery by removing the abnormal brain area without compromising the function of the rest of the brain [4]. In this research work, only the focal or partial type of seizure is considered, for which seizure prediction is feasible.

The state of an epileptic brain can be considered as having a number of stages [28]. The ictal stage starts at the seizure onset and ends at the seizure's end. The preictal stage is the period before the seizure onset. The postictal stage is the period following the seizure end. The period between the postictal stage of one seizure and the preictal stage of the next seizure is called interictal stage. An example of an intracranial EEG recording from different stages of an epileptic seizure is given in Fig. 1.2. Based on the traditional nonlinear dynamic analysis methods, the seizure can be predicted by evaluating the dynamical changes in these different stages.

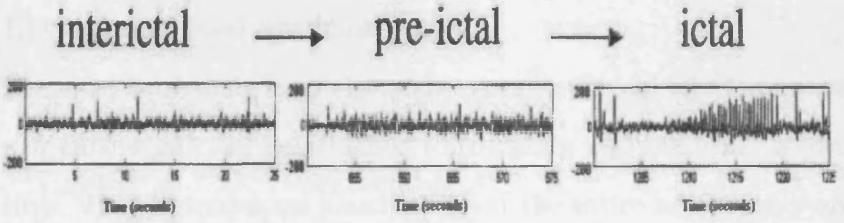

Figure 1.2. An example of a 20-minute intracranial EEG recording before a spontaneous seizure, which shows three different stages of an epileptic seizure [41].

1.2.3 Brain Function Monitoring Modalities

EEG

Introduced by Hans Berger in 1929, EEG represents the electrical activity of the brain which is recorded from electrodes placed on the scalp. It provides a noninvasive means of monitoring brain activity and investigating brain function disorders. EEG plays a very important role in the diagnosis of specific neurological diseases such as epilepsy and it is

a very useful tool in clinical diagnosis and applications.

The EEG is a recording of the electrical current potentials spontaneously generated by cortical nerve cell inhibitory and excitatory postsynaptic potentials. These postsynaptic potentials summate in the cortex and extend to the scalp surface where they are recorded as the EEG signals (EEGs). Generally, the EEG reflects the changes of cerebral function directly and reliably, especially if the structural lesions are localized near the surface of the hemispheres. The EEG recording system basically consists of sensors (electrodes), amplifier circuit, and a computer as the terminal for archiving and displaying the data. The electrical activity is monitored from an array of many electrodes and the EEGs are recorded simultaneously.

The most commonly used electrode types in clinical EEG are metal discs or cups which can be attached to the scalp and the other recording sites. The electrodes are placed to cover the entire head evenly and connected to the amplifying and recording channels (as shown in Fig. 1.3). The most widely used EEG electrode placement is referred to as the International 10-20 system [5]. In this system, each electrode site has a letter to specify the lobe, along with a number to identify the hemisphere. The letters used are: F (Frontal lobe), T (Temporal lobe), C (Central lobe), P(Parietal lobe), and O (Occipital lobe), and Z refers to an electrode placed on the mid-line . Odd and even numbers represent, respectively, the left and right hemispheres. Fig. 1.4 illustrates the electrode placement of the International 10-20 system.

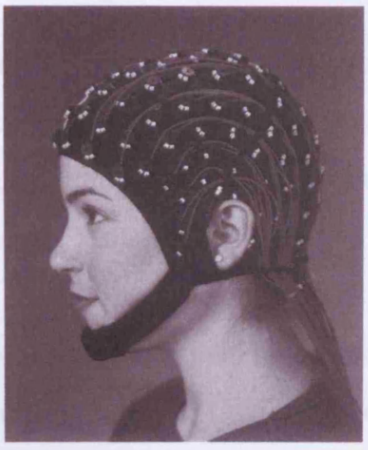

Figure 1.3. An example of the EEG recording system *NeuroScan*, which shows how the electrodes are placed over the head [5].

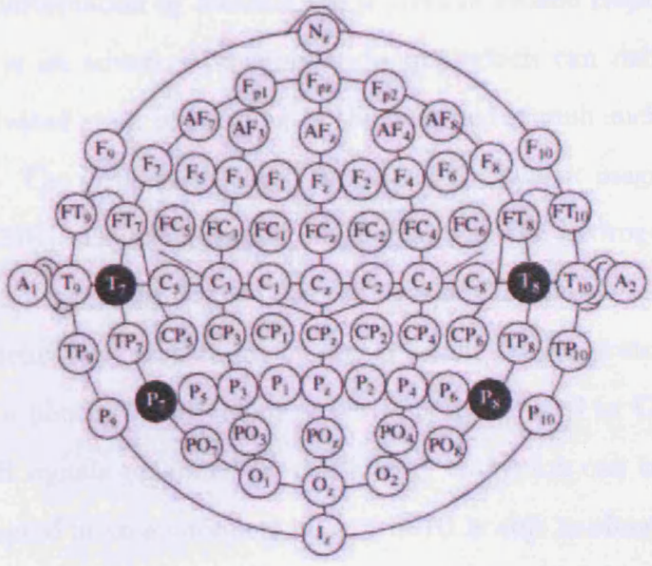

Figure 1.4. The electrode placement of the International 10-20 system. The letters are used to specify the lobe, F (Frontal lobe), T (Temporal), C (Central lobe), P (Parietal lobe), and O (Occipital lobe), and Z refers to an electrode placed on the mid-line [5].

Other Brain Function Monitoring Modalities

With the development of advanced technology, more measurement devices have been made to monitor the small physiological changes in the human brain. Apart from EEG, other recording modalities include MEG, fMRI and Positron Emission Tomography (PET).

MEG is another noninvasive technology for functional brain mapping, which measures the magnetic field emanated by the synaptic currents from the brain. Unlike EEG, in which the spatial resolution is poor due to poor skull conduction, MEG provides much higher spatial resolution than EEG because the magnetic fields are less affected by the changes in electrical conductivity. Compared with fMRI, which provides structural or anatomical images, MEG reveals the functional mapping information by locating the sources of evoked responses [6].

fMRI is an advanced imaging technique which can delineate the brain activated areas responding to the designed stimuli such as sound and light. The principles of MRI are based on nuclear magnetic resonance (NMR). The NMR signal originates from the hydrogen nucleus which has a single proton. When the proton is placed in an external magnetic field, transitions of energy occur as the proton absorbs or emits a photon (more detail of NMR is introduced in Chapter 5). The NMR signals generated by this energy transition can be detected and presented in an anatomical image. fMRI is able to show the blood flow in the activated areas in the images as the blood oxygen level-dependence (BOLD) response, and therefore it can provide valuable spatial information on the brain. But, because it relies on blood flow response rather than electrical activities, it has a relatively slow response to temporal changes [108].

It is seen that each modality has its own advantages. How to integrate various modalities and maximize their advantages in real applications has become a very interesting topic in recent years. For example, EEG reflects the brain changes on a timescale of milliseconds (1kHz or more), which is capable of capturing the dynamic changes of the brain very well. However, it has poor spatial resolution due to being recorded from a limited number of electrodes on the scalp, and the problem of source localization from the EEG still remains a research challenge. On the other hand, fMRI is extremely powerful for investigation of spatial aspects of brain function, but it is slow to follow the brain activities because it relies on the brain blood flow response rather than electrical activities. Therefore, a combined EEG-fMRI system becomes more attractive. Fusion of these two modalities has been of increasing interest to researchers to exploit the temporal and spatial information effectively at the same time. In this work, the fusion of EEG and fMRI is investigated and discussed in Chapter 5 and Chapter 6.

In the next section, one of the most important and widely used tools in brain signal analysis and source separation, namely independent component analysis, is reviewed.

1.3 Independent Component Analysis

1.3.1 Problem Description

Blind source separation (BSS) is an effective technique to recover the unknown signals or sources from an observed signal mixture based on the weak assumption of the mutual independence between the sources. BSS is often performed by means of Independent Component Analysis

(ICA). A famous example describing this problem is the so called *cocktail party problem.* Imagine that in a room there are m people speaking simultaneously, and n microphones are recording the time signals. Each of these recorded signals is the weighted sum of the signals from the m speakers under a certain unknown mixing system. Then the aim of BSS is to extract the signals of each speaker as the independent components (ICs). The term "blind" means that the sources and their combination method are unknown. For the sources, the number and their statistical properties are unknown except that mutual independence between the sources is assumed. For the combination system, the sources could be linearly or nonlinearly combined, or could be instantaneously or convolutively combined.

The simplest ICA model is the instantaneous model which assumes that the source signals arrive at the sensors at the same time. Then the problem can be described mathematically as follows. The n channels of observed data $\mathbf{x}(t) = [x_1(t), x_2(t), ..., x_n(t)]^T$ are linear and instantaneous mixtures of m underlying sources $\mathbf{s}(t) = [s_1(t), s_2(t), ..., s_m(t)]^T$,

$$\mathbf{x}(t) = \mathbf{A}\mathbf{s}(t) + \mathbf{e}(t) \tag{1.3.1}$$

where $\mathbf{A}$ is an $n \times m$ mixing matrix, $\mathbf{e}(t)$ is the observation noise, and t denotes discrete time index. The sources $\mathbf{s}$ can be estimated by a separation matrix $\mathbf{W}$ through inversion of the data model in Eq. (1.3.1),

$$\mathbf{y}(t) = \hat{\mathbf{s}}(t) = \mathbf{W}\mathbf{x}(t) \tag{1.3.2}$$

where $\mathbf{y}(t)$ is the estimated source, and $\mathbf{W} = \mathbf{A}^{\dagger}$ is the pseudo-inverse of the mixing matrix and $\mathbf{WA} = \mathbf{I}$.

Ambiguities in ICA

Since ICA is used to find the solutions for both the mixing matrix $\mathbf{A}$ and the unknown sources $\mathbf{s}$ simultaneously, the solutions are not unique. The product $\mathbf{As}$ can be combinations of different sets of statistically independent signals, because any scalar multiplier in source $\mathbf{s}_i$ can be cancelled by dividing the corresponding column of $\mathbf{A}$ by the same scalar. The ICs can also have an arbitrary permutation of the original sources. These ambiguities can be expressed mathematically as

$$\mathbf{y}(t) = \hat{\mathbf{s}}(t) = \mathbf{WAs}(t) = \mathbf{PDs}(t) \tag{1.3.3}$$

where $\mathbf{P}$ is a permutation matrix and $\mathbf{D}$ is a nonsingular scaling matrix.

The indeterminacies associated with the order and scale of the ICs seem to be the limitations, but in most applications, these limitations are not troublesome since the most relevant information about the source signals is contained in the waveforms of the sources but not in their amplitude or the order in which they are arranged. For example, in the cocktail party problem, which speaker's signal is distinguished first is not that important. In some applications such as speech coding techniques, scaling of the signals can be tolerated since the most important factors concern frequencies rather than magnitudes of the waveforms [69]. In existing ICA algorithms, in order to determine the scales, some constraints can be imposed on the unmixing matrix and estimated sources explicitly or implicitly. In practice, a preprocessing called whitening is usually applied, which not only rescales the data to have unit variance, but also make the unmixing matrix orthogonal and

therefore ensures the recovered sources have unit variance too.

Whitening

Two zero mean real random variables y_i and y_j are said to be uncorrelated if their covariance is zero [65]:

$$cov(y_i, y_j) = E\{y_i y_j\} - E\{y_i\}E\{y_j\} = 0 \tag{1.3.4}$$

where $E\{\}$ is the statistical expectation operator and $cov(\cdot)$ denotes the lag zero covariance between two variables. For the variables with zero mean and unit variance, the covariance is equal to correlation $cor(y_i, y_j) = E\{y_i y_j\}$[1]. A zero-mean random vector $\mathbf{y}$ is said to be white if its elements y_i are uncorrelated and have unit variance, $E\{\mathbf{y}\mathbf{y}^T\} = \mathbf{I}$, with $\mathbf{I}$ the unit matrix. Data whitening can be performed by linear transformation of the observed data $\mathbf{x}$ by linearly multiplying it by a matrix $\mathbf{V}$, i.e.

$$\mathbf{z}=\mathbf{V}\mathbf{x} \tag{1.3.5}$$

where $\mathbf{V}$ is the whitening matrix, and $\mathbf{z}$ is the data vector after whitening with $E\{\mathbf{z}\mathbf{z}^T\} = \mathbf{I}$, for which each element has unit variance. A popular technique for whitening is using the eigenvalue decomposition (EVD) of the covariance matrix, i.e.

$$E\{\mathbf{x}\mathbf{x}^T\} = \mathbf{U}\Phi\mathbf{U}^T \tag{1.3.6}$$

[1]In the statistical literature, correlation is often defined as a normalised version of covariance [65]. In this thesis, this simpler definition of correlation is used, which is given in Eq. (4.3.7), unless otherwise mentioned.

where $\mathbf{U}$ is the orthogonal matrix of unit-length eigenvectors of $E\{\mathbf{x}\mathbf{x}^T\}$ and Φ is the diagonal matrix of its eigenvalues. And the whitening matrix $\mathbf{V}$ is obtained by $\mathbf{V} = \mathbf{U}\Phi^{-1/2}\mathbf{U}^T$. After data whitening,

$$\mathbf{z}=\mathbf{VAs}=\tilde{\mathbf{A}}\mathbf{s} \tag{1.3.7}$$

where $\tilde{\mathbf{A}} = \mathbf{VA}$ is a new mixing matrix and is orthogonal $\tilde{\mathbf{A}}^T\tilde{\mathbf{A}} = \mathbf{I}$. As whitening is essentially a decorrelation process followed by scaling, it is a useful and standard preprocessing for ICA. (In this thesis, all experimental data were preprocessed by removing their mean values and whitening so that the estimated sources had unit variance.)

Number of Sources

Another indeterminacy in ICA is that the number of sources is generally unknown. For simplicity, many learning algorithms for ICA usually assume that the number of sources is equal to the number of sensors, or is known a *priori*. However, in practice, these assumptions do not often hold. When the number of sensors is less than the number of sources ($n < m$), the BSS problem becomes underdetermined. In this case, the source signals are difficult to be completely separated as there are more unknowns than available information. The problem may be solved under some special circumstances, such as assuming the column vectors of the mixing matrix satisfy some special conditions [8]; assuming that the signals are sparse and therefore have a sparse distribution [9]. Some advanced clustering techniques such as k-mean combined with gap statistics have been exploited for detection of the active sources [10]. When the number of sensors is larger than the number of sources ($n > m$), the BSS problem is overdetermined, and the learn-

ing rules become relatively complicated as the unmixing matrix will be related to the pseudo-inverse of the mixing matrix. Several neural network architectures, together with the associated learning algorithms, have been discussed to solve the problem [11]- [16].

For an overdetermined case, in practice, the most popular method to separate the signal and noise subspace is using Principal Component Analysis (PCA). The number of principal components is determined by analysing the eigenvalues of the covariance matrix. The eigenvalue sequence of a covariance matrix for the observed data is usually sharply decreasing, a threshold can be set where the eigenvalues become constant. In some applications, the number of sources is simply chosen as the minimum number of principal components that contain 90% of the variance [65].

Estimation of the number of independent sources is still an open question and the problem becomes more complex when it comes to brain signal separation. Some methods have been investigated in [14]- [16] for estimation of the number of sources in EEG signals for the overdetermined case. In these methods, an approach based on an information theoretic criterion is applied to the eigenvalues of the covariance matrix. As in [14], the information criterion consists of two parts. the first part is a likelihood function that represents the information obtained from the measured data, which are dependent on the assumed number of sources. The second part is a penalty function of the data points in the time domain, which represents the uncertainty of parameters in the probabilistic model with increase of the data points. Then the information criterion value with eigenvalues are calculated based on the proposed method, and the number of sources with minimum infor-

mation criterion value is selected as the estimated number of sources. In this thesis, this method was applied to estimate the number of EEG sources, and the number of sources was assumed to be equal or less than the number of sensors.

1.3.2 Principles of Estimation

Assumption of Independence

The task of BSS is to find a separation system to reconstruct the unknown sources which are as independent as possible based only on the observed data and weak assumptions of independency between the unknown sources. Technically, the independence of the data can be defined by using their probability densities. Consider the random variables $y_1, y_2, ..., y_n$, having a joint pdf of $p(y_1, y_2, ...y_n)$ and marginal pdfs of $p(y_i)$, then $y_1, y_2, ..., y_n$ are said to be independent if their joint pdf can be factorized as:

$$p(y_1, y_2, ...y_n) = \prod_{i=1}^{n} p(y_i) \tag{1.3.8}$$

There are certain assumptions that the basic ICA model must follow [65]: (1) the sources are assumed to be statistically independent; (2) the independent components must generally have *non-Gaussian* distribution; (3) the number of independent components is equal to the number of observed mixtures.

The principle of ICA estimation is to maximize the independence between the outputs as much as possible. Popular approaches include maximization of non-Gaussianity, minimization of mutual information, maximization of likelihood estimation, and tensorial methods [65].

Maximization of Non-Gaussianity

Maximization of non-Gaussianity is based on the Central Limit Theorem, which states that the distribution of a sum of independent random variables tends towards a Gaussian distribution. Therefore, each source is less likely to have Gaussian distribution than the sum of the sources. The classical quantitative measurement of non-Gaussianity are kurtosis and negentropy.

The kurtosis of a random variable y is defined by

$$kur(y) = E\{y^4\} - 3(E\{y^2\})^2 \tag{1.3.9}$$

For simplicity, y is assumed to be centered (zero mean) and has variance equal to one. Thus the kurtosis is simplified as $E\{y^4\} - 3$. For a Gaussian y, the fourth moment equals $3(E\{y^2\})^2$. Thus, kurtosis is zero for a Gaussian variable [65]. Variables with negative kurtosis are referred to as sub-Gaussian and those with positive kurtosis are called super-Gaussian .

Maximization of non-Gaussianity by measuring negentropy is based on a fundamental result of information theory, in which a Gaussian variable has the largest entropy among all continuous random variables of equal variance [7]. Entropy is one of the basic concepts in information theory, which can be interpreted as the degree of information that the observed random variable delivers. The more "random" or unpredictable the variable, the larger is its entropy. For a discrete-valued random variable y, the entropy H is defined as:

$$H(y) = -\sum_i P(y = a_i) log_2 P(y = a_i) \tag{1.3.10}$$

where a_i is a possible value of y and P is the probability that $y = a_i$. The unit of entropy is depended by the base of logarithm, which is *bit* for base of 2, and *nat* for natural logarithm.

The differential entropy H of a continuous random vector $\mathbf{y}$ with density $p(\mathbf{y})$ is defined as:

$$H(\mathbf{y}) = -\int_{-\infty}^{+\infty} p(\mathbf{y}) log_2 p(\mathbf{y}) d\mathbf{y} \tag{1.3.11}$$

Negentropy J is an extension of the differential entropy which is zero for a Gaussian random vector and always non-negative,

$$J(\mathbf{y}) = H(\mathbf{y}_{gauss}) - H(\mathbf{y}) \tag{1.3.12}$$

where $\mathbf{y}_{gauss}$ is a Gaussian random vector.

Minimization of Mutual Information

Mutual information is a measure of the information in common between the various sets of random variables. Information about one variable can therefore reduce the uncertainty about the other. For example, if x and y are independent, then knowing x does not give any information about y and vice versa, so their mutual information is zero. Using entropy, the mutual information I between n scalar random variables y_i, $i = 1, ..., n$, can be given as,

$$I(y_1, y_2, ..., y_n) = \sum_{i=1}^{n} H(y_i) - H(\mathbf{y}) \tag{1.3.13}$$

If we assume that $\mathbf{y} = \mathbf{W}\mathbf{x}$, an invertible linear transformation of mutual information is expressed [65] as:

$$I(y_1, y_2, ..., y_n) = \sum_{i=1}^{n} H(y_i) - H(\mathbf{x}) - log|det\mathbf{W}| \tag{1.3.14}$$

where $|\cdot|$ is the absolute value, and $det(\cdot)$ is the determinant of the matrix. It is noticed that if the estimated sources y_i are constrained to be uncorrelated and of unit variance, the mutual information is equal to the negative sum of negentropy. Thus, minimizing the mutual information is equivalent to maximization of the non-Gaussianity [7].

Maximization of Likelihood Estimation

Maximum likelihood estimation is one of the most common statistical estimation principles which can be used for estimation of the ICA model. Assuming the linear instantaneous ICA model $\mathbf{x} = \mathbf{As}$, the likelihood for the mixtures can be expressed as:

$$p(\mathbf{x}) = |det\mathbf{W}| \prod_{i=1}^{n} p_i(s_i) \tag{1.3.15}$$

As a result, the log likelihood can be written as [65]:

$$\frac{1}{T} logL(\mathbf{W}) = E\{\sum_{i=1}^{n} logp_i(\mathbf{w}_i^T \mathbf{x})\} + log(|det\mathbf{W}|) \tag{1.3.16}$$

where log is generally the natural logarithm operator, and $\mathbf{w}_i$ is the i-th column of $\mathbf{W}$. The likelihood is therefore a function of the unmixing matrix $\mathbf{W}$, which can be estimated by various algorithms.

Tensorial Method

The tensorial method provides a different approach to ICA estimation by using a high-order cumulant tensor. The cumulant tensor is a four dimensional array whose entries are given by the fourth-order cross-cumulant of the data, $cum(x_i, x_j, x_k, x_l)$. The fourth-order cumulant is given as [65]:

$$cum(x_i, x_j, x_k, x_l) = E\{x_i x_j x_k x_l\} - E\{x_i x_j\}E\{x_k x_l\} - E\{x_i x_k\}E\{x_j x_l\} - E\{x_i x_l\}E\{x_j x_k\} \quad (1.3.17)$$

It is seen that the cumulant tensor can be considered as a four-dimensional covariance matrix. By making all its "off-diagonal" elements equal to zero it will give an estimation of the independent components. The problem with the tensorial method is that it is not suitable for high dimensional spaces due to the expensive computation of the coefficients of the fourth-order tensor. However, it provides an efficient alternative solution for low-dimensional problems.

1.3.3 Algorithms

As described in the above section, the main objective for BSS is to find the separation matrix which can separate the mixtures into their constituent statistically independent components. Practically, the solution is based on the optimization of some cost function, also called objective function or contrast function. The cost function is a function of the distribution of the output $\mathbf{y} = \mathbf{W}\mathbf{x}$ and must be designed in such a way that source separation is achieved when the cost function reaches its minimum or maximum value. The cost function can be designed

based on the above estimation principles.

The steps of a general procedure for executing a BSS algorithm are: 1) centring the variables, which means removing the sample mean from the observed variables; 2) "whitening" or "sphering", which will decorrelate the data; 3) dimension reduction, if needed, by choosing the number of principal components; 4) choosing and performing the proper separation algorithm.

There are various well established ICA algorithms which can solve the ICA problem efficiently. For example, FastICA [7] is based on a fixed-point iteration scheme for maximizing non-Gaussianity of the estimated sources; blind source extraction (BSE) [83] can extract the sources one-by-one by maximizing the kurtosis of the output. (BSE is explained in detail in Chapter 5). The contrast function of Infomax [133] is derived from a neural network viewpoint, which was based on maximization of the mutual information between the input and output. The detail of the Infomax algorithm is explained in Chapter 6. An algorithm based on the tensorial method called *joint approximate diagonalization of eigenmatrices* (JADE) [17] is introduced in Chapter 4. There are also some algorithms developed based on the modified ICA model, such as topographic ICA, which relaxes the independence assumption. It assumes that the sources that are geometrically close to each other are less independent, and instead have some dependence which can be defined by high-order correlation. Details of the topographic ICA are given in Chapter 3.

1.4 Organization of the Thesis

In this chapter, the physical background about brain structure and basic functions are first introduced, following the basic knowledge of epileptic seizure. The advanced brain function monitoring modalities such as EEG and fMRI are introduced. The fundamental concept of ICA and the principles of ICA estimation are also given in this chapter. The remainder of this thesis is organized as follows.

In Chapter 2, the traditional methods for epileptic seizure prediction are reviewed. The review focuses mainly on the nonlinear analysis methods in prediction. The theory of chaos is introduced and two chaos quantification techniques, namely the Lyapunov exponent-based and correlation dimension-based methods, are explained. The research approach of the work is addressed in the final section of the chapter.

In Chapter 3, a novel constrained topographic ICA (CTICA) algorithm is proposed. In contrast to other well-known ICA algorithms, CTICA relaxes the assumption of independence and considers that sources geometrically close to each other are less independent. By introducing the spatial and frequency information of seizures as the constraint, the proposed CTICA algorithm achieves a better performance for seizure source separation than other well-known ICA algorithms. The details of the algorithm are given and the results are discussed.

In Chapter 4, the predictability of epileptic seizure is investigated. The algorithms are applied to the simultaneously recorded intracranial and scalp EEGs. The traditional nonlinear method is applied to examine the predictability of the separated seizure sources. It is shown that the predictability measured from the estimated sources using CTICA is comparable with the results obtained from intracranial EEGs. Also

the CTICA is more computationally efficient than the other two algorithms.

In Chapter 5, one technical problem in fusion of EEG and fMRI, scanner artifact in EEGs, is studied. An effective method is introduced to remove the fMRI scanner artifact from the jointly recorded EEG-fMRI data. Blind source extraction is applied to extract the fMRI scanner artifacts, which is more convenient and efficient than the traditional averaging and subtraction approach.

A new approach for analysis of epileptic seizure fMRI is addressed in Chapter 6. Unlike the popular general linear model (GLM) [105], spatial ICA does not rely on the predicted stimuli response and predefined hemodynamic response function (HRF). Instead, unknown sources are assumed to be spatially independent, based on the fact that brain areas executing different tasks are spatially independent [114]. A constrained spatial ICA is developed by incorporating EEG as the temporal constraint. The experimental results show that the seizure activated area is clearly detected.

In the final chapter, the presented work is summarised and the promising perspective of applying the proposed methods to real epileptic seizure prediction is provided. Also the limitations and future work are discussed and the conclusions are given.

Chapter 2

EPILEPTIC SEIZURE PREDICTION: LITERATURE REVIEW

2.1 Introduction

Epilepsy is characterized by sudden occurrences of synchronous activity within relatively large neuronal networks that disturb the normal working of the brain. Such activity may lead simply to a brief impairment of consciousness but also to a more or less complex series of abnormal sensory and motor manifestations, which is usually called a seizure [46]. Because of its unforeseeable occurrence, the seizure may cause fatal hazards to the patient. The pharmacological method is still the primary treatment for epilepsy and patients have to take anticonvulsant drugs daily to avoid seizures. Surgical intervention is an alternative solution, but only patients with focal type seizures (for which the epileptogenic zone can be accurately detected) can be treated by surgery. Also side effects from both pharmacological and surgical treatments have been reported. There are still large numbers of epilepsy patients whose seizures cannot be controlled by any available treatment methods. Therefore,

an advanced warning of the impending seizure which can anticipate clinical attacks becomes very important.

Epilepsy can be considered as a dynamical disease of brain systems. The state of an epileptic brain can be considered as having a number of stages, mainly, interictal (normal brain activity), preictal (prior to seizure onset), ictal (seizure onset) and postictal (after seizure) [28]. The transition between interictal and ictal can either occur as a continuous sequence of phases in some cases of focal seizures, or as a sudden leap in most cases of absence seizures [46]. In the case of the gradual transition, the seizures could be anticipated in an early phase by applying some mathematical tools.

In this chapter, firstly, the concept of chaos is introduced and two nonlinear system quantification methods, namely Lyapunov exponent and correlation dimension, are explained. Then, a literature review of seizure prediction based on nonlinear analysis approaches is presented. In the third section, the main approach of this research is addressed.

2.2 Nonlinear Dynamic System

2.2.1 Chaos and Dynamic System Reconstruction

Chaos

In physical science, chaos is the term used to describe irregular but deterministic motion [25]. A chaotic system can be considered as a system that consists of a set of variables, which change according to certain dynamic equations. The system can be multidimensional. The space constructed by these variables is called a *phase space.* The path through which the variables move is referred to as the *trajectory.* The

trajectory to which the system converges is the equilibrium state and is called an *attractor*. The number of independent geometric coordinates in the phase space is defined as the *embedding dimension*, which is needed to capture the behaviour of an attractor [23] [25].

Dynamic System Reconstruction

A system with chaotic behaviour can be considered as a nonlinear dynamic system that changes with time, but can not be modelled by any transfer function as for a linear system. Dynamic modelling is aimed at finding a model of the system to illustrate the underlying nonlinear dynamics that cause its chaotic behaviour. In order to build a model, the dynamic state space requires to be reconstructed from a given chaotic time series. The dynamic system reconstruction can be carried out based on the *delay-embedding theorem* [24].

The *delay-embedding theorem* was introduced by Takens and Mane in 1981 [24]. According to this theorem, an unknown dynamical system in discrete time is described as [23]:

$$\mathbf{x}(t+1) = F(\mathbf{x}(t)) \tag{2.2.1}$$

where $\mathbf{x}(t)$ is the d-dimensional state vector of the system at time t, and $F(\cdot)$ is the vector-valued function. The output of the system $\mathbf{y}(t)$ is defined in terms of the state vector $\mathbf{x}(t)$ as follows:

$$y(t) = h(\mathbf{x}(t)) + e(t) \tag{2.2.2}$$

where $h(\cdot)$ is a scalar-valued function, and $e(t)$ denotes additive noise. Eq. (2.2.1) and Eq. (2.2.2) describe the state-space behaviour of the

dynamical system. According to Takens' theorem, the reconstruction of a dynamic system can be obtained by unfolding the output y with $e(t) = 0$ in a D-dimensional space. The space constructed from the new vector $\mathbf{y}_R(t)$ can be written as:

$$\mathbf{y}_R(t) = [y(t), y(t-\tau), ..., y(t-(D-1)\tau)]^T \tag{2.2.3}$$

where T denotes the transpose, and τ is a positive integer called the embedding delay. The *delay-embedding theorem* states that it is possible to reconstruct the dynamical system under the condition that $D \geq 2d + 1$, where d is the dimension of the attractor. The procedure to look for D is called *embedding*. The system can be reconstructed when D reaches its minimum integer value. This minimum of D is referred to as the *embedding dimension* [23].

2.2.2 Nonlinear System Quantification

Lyapunov Exponents

Lyapunov exponents measure the average exponential rates of convergence or divergence of nearby trajectories within the phase space [26]. The mathematical definition can be explained as in an n-dimensional phase space, an infinitesimal n-sphere under initial conditions will become an n-ellipsoid after the long time evolution due to the local deforming nature of the attractor. As an example, Fig. 2.1 shows a circle under initial condition evolving into an ellipse after a certain evolution time. The circle has radius d_0 in the initial state. After a continuous transition time t', the circle is deformed into an ellipse with major axis length $d_1 = d_0 e^{\lambda_1 t'}$ and minor axis length $d_2 = d_0 e^{\lambda_2 t'}$. The i^{th}

Lyapunov exponent is then defined by:

$$\lambda_i = \lim_{t' \to \infty} \frac{1}{t'} \ln(\frac{d_i(t')}{d_0}) \tag{2.2.4}$$

The Lyapunov exponent determines whether a system is chaotic or not. If the system trajectory attracts to a stable fixed point, then it will have a negative Lyapunov exponent, in which case the system exhibits asymptotic stability and is called the dissipative or non-conservative system. A system with zero Lyapunov exponent is conservative, in which the orbits would maintain a constant separation. If the Lyapunov exponent is positive, then the system is chaotic and unstable, whereby the nearby points will diverge to any arbitrary separation. By convention, Lyapunov exponents are ordered from largest to smallest as $\lambda_1 > \lambda_2 > \lambda_3$.... Each dimension contains one Lyapunov exponent. The sum of the Lyapunov exponents is the time averaged divergence of the phase space velocity. It is common just to refer to the largest one, because it determines the predictability of a dynamical system.

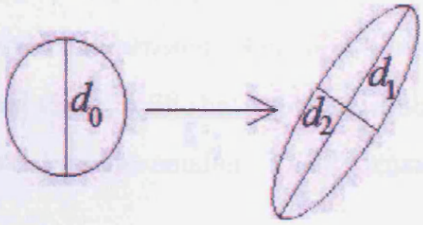

Figure 2.1. An example to illustrate the evolution of a circle under initial conditions into an ellipse due to the deforming nature of the attractor, where d_0 is the radius of the circle in the initial state, d_1 and d_2 are the major axis length and minor axis length of the ellipse.

Correlation Dimension

In mathematics, dimensions are the parameters required to describe the position and relevant spatial characteristics of any object within a conceptual space. As in Euclidean geometry, points have dimension $d = 0$. The dimension d equals 1, 2, 3 for lines, a plane surface and a solid, respectively. Standard objects in Euclidean geometry have integer dimensions, but in a dynamical system, the dimension of the attractors can be non-integer. In chaos theory, an attractor with non-integer dimension is called a strange attractor [23] and its dimension can be defined by a fractal dimension. A fractal is generally "a rough or fragmented geometric shape that can be split into parts, each of which is (at least approximately) a reduced-size copy of the whole" and fractals are often considered to be infinitely complex [27]. The fractal dimension is a statistical quantity that gives an indication of how completely a fractal appears to fill a space, when the fractal zooms down to finer and finer scales [26].

One simple example to quantify the fractal dimension of a space is called the *box-counting dimension.* This is a measure of how many balls with radius ϵ are taken to fill that space, and how this measure is changed as the radius ϵ becomes smaller. The dimension D is quantified [26] as:

$$D = \lim_{\epsilon \to 0} \frac{log_2 N(\epsilon)}{log_2 \epsilon} \tag{2.2.5}$$

where N is the number of balls with radius ϵ. The *box-counting dimension* is also referred to as D_0. Another alternative is the *correlation dimension* D_2, which is defined [32] as:

$$D_2 = \lim_{r \to 0} \frac{log_2(C(r))}{log_2 r} \tag{2.2.6}$$

where $C(r)$ is the correlation integral (also called correlation sum) and r is a distance threshold. In chaos theory, the correlation integral is the mean probability that a randomly selected pair of points is separated by a distance less than r,

$$C(r) = \lim_{N \to \infty} \frac{1}{N^2} \sum_{i,j=1}^{N} \Theta(r - \|\mathbf{y}_R(i) - \mathbf{y}_R(j)\|_2) \tag{2.2.7}$$

where $\|\cdot\|_2$ is the Euclidean norm, and $\Theta(\cdot)$ is the Heaviside step function ($\Theta(k) = 0$, if $k \leq 0$; $\Theta(k) = 1$, if $k > 0$). N is the number of points embedded in a reconstructed dimension, and $\mathbf{y}_R$ is already defined in Eq. (2.2.3).

2.3 Literature Review

Before the early 1940s, the general belief in the medical community was that epileptic seizure could not be predicted. Seizures were assumed to occur randomly over time. In the 1940s, reports from clinical practitioners pointed out that patients could sense various feelings of auras before the seizure [19], which provided evidences that seizures might be predictable. The early investigations on predictability of seizures were conducted by Vigilone et al. in the 1970s [20]. The experiments were based on the analysis of scalp EEG recordings by applying pattern recognition techniques in order to capture the preictal (brain stage prior to seizure onset) features of EEG in the frequency domain. The research project was abandoned due to too many false warnings. In the early 1980s, it was reported that there were consistent changes of

spike activity prior to seizure onset [21] [22]. Lange et al. showed that the spatial pattern of spikes changed progressively and the number of spikes increased significantly prior to seizure. But their experiments were performed by counting spikes visually, therefore the analysis was too difficult to be carried out in long-term continuous EEG recordings due to the time consuming nature of the analysis method.

After the 1980s, with the development of new signal processing methodologies, more methods for seizure prediction were developed, including frequency-based method [43], wavelet decompositions [44], and nonlinear dynamic analysis of EEG signals [28]- [31]. In this work, the focus is on the nonlinear dynamic approach. The nonlinear dynamic methodologies rely on evaluation of the chaotic behaviour of the epileptic brain by quantification of the nonlinear dynamics of the recorded data time series. The nonlinear techniques are mainly based on reconstruction of the dynamic system, and then apply the nonlinear quantification methods to characterize the system. Examples of these quantification methods include the Lyapunov exponent (the mean rate of divergence of initial neighbouring states), the correlation dimension (the quantification of the system complexity), and Kolmogorov entropy.

The first group which reported the application of nonlinear dynamics to EEGs for epileptic seizure prediction was led by Iasemidis, Sackellares and Williams. They reported that EEG during epileptic seizure could be better modelled as an output of a nonlinear system than a linear system [28]. Their research was based on analysis of continuous multichannel EEG at different stages (preictal, ictal and postictal), by quantifying the dynamic changes of epileptic seizures by means of short-term largest Lyapunov exponent (STLmax). The core finding

was that the focal seizure can cause transition of the epileptic brain from less ordered (chaotic) to more ordered, and then back to less ordered, referring to this as a chaos-to-order-to-chaos transition [4]. This transition may start from seconds, minutes or hours before the clinical seizure onset [29]. In their latest research, they applied the nonlinear measurement to continuous long-term EEG recordings, and seizure prediction was carried out by an adaptive algorithm when the time of the first seizure was known. The results raised the hope that nonlinear dynamic techniques could be applied for real diagnostic and therapeutic applications.

Since the 1990s, Lehnertz and Elger have examined the spatio-temporal dynamic of the epileptogenic area by investigating the complexity changes in neuronal behaviour [32] [33], with complexity defined by means of the correlation dimension. In their results, pronounced changes of the dimension in time were found, with a gradual decrease observed as the distance from the focal area increased. Also, the complexity was observed to decrease during the transition of epileptic seizure. The lowest complexity was found in the focal area during the ictal state. This study showed the spatio-temporal dynamical changes during the progress of seizure.

Quyen et al. [35] proposed a new method to analyse the long-term non-stationary EEGs by measuring the similarities in dynamics between different parts of the time series. The similarity measures the correlation integral of the EEGs within a sliding window with a reference EEG segment. The reference was chosen far away from the seizure segments. (More detail of similarity can be found in [35]). They showed that the method can track, in real time, the spatio-temporal changes in

the brain dynamics several minutes prior to seizure. Their results were accordant with other nonlinear analysis findings, in which the similarity gradually decreases prior to seizure onset and the lowest value of similarity corresponds to the seizure. The results from all these approaches provide evidences that there are measurable differences in the EEG prior to seizure onset, which can be exploited for epileptic seizure prediction.

So far, most seizure prediction techniques have been based on the analysis of intracranial EEG signals in which surgical operation is required to implant the electrodes in the brain. In order to capture the seizures, the electrodes must be implanted close to the epileptogenic zone, otherwise the seizure can not be captured and prediction may not be accurate. Also, the surgery may be hazardous to the patients. Therefore, a warning method based on analysis of the noninvasive recording of scalp EEG is highly desirable.

It has been reported that the scalp EEG contains sufficient dynamic information which can be used for analysis of changes prior to seizure [36] - [42]. The seizure transition in scalp EEG has been investigated by Iasimidies' group [36] [37]. They observed a similar preictal transition in scalp EEG as in the intracranial EEG recordings, which suggested the possibility of prediction by the analysis of scalp EEG. Quyen et al. [41] evaluated scalp EEG recordings based on measurement of similarity from 26 patients with temporal lobe epilepsy. In most cases (25 out of 26), the measurements showed the predictability of the seizure by several minutes prior to seizure. Although their work demonstrated that scalp EEG can be used for dynamic changes, it was also pointed out that the potential produced by scalp electrodes may also be driven

by events generated by deeper cerebral structures and more studies were required using source localization methods.

However, seizure prediction from standard scalp EEG has faced certain difficulties. It is well-known that the neural electrical potentials recorded from scalp EEG are not only attenuated by the skull and scalp, but are also subject to noise and artifacts, which remain as major problems for seizure prediction from scalp EEG. A novel approach proposed by Corsini et al. [42] applied blind source separation (BSS) to separate the seizure sources from the EEG mixtures prior to chaos measurement and therefore to investigate the predictability from the scalp EEG. This work provided very encouraging results. In this method, seizures were considered as contributing sources of EEGs, which can be separated using BSS techniques. Then, traditional nonlinear methods (Lyapunov exponent) were applied to the separated sources. They demonstrated that the largest Lyapunov exponent for some sources shows a decreasing trend prior to seizure. Although there are unsolved problems, such as seizure source identification and expensive computational cost, this approach opened a new field for seizure prediction.

2.4 The Research Approach

In this chapter, the background knowledge of nonlinear dynamic system has been introduced and two nonlinear quantification methods have been explained. Literature review of seizure prediction based on nonlinear analysis methods has been presented.

The objective of this research was to continue the exploration of predictability of seizure from scalp EEG by using BSS techniques and incorporating spatial information of fMRI, which allowsed both the sep-

aration and the localization of seizure from the multi-channel EEGs. The challenge of this research was, (1) to develop a separation algorithm which can separate the seizure sources effectively; (2) to solve the problem of seizure source identification by fusion of EEG and fMRI; and (3) to investigate the predictability of seizure by evaluating the nonlinear dynamics of the estimated sources within a long time multi-channel EEGs.

Chapter 3

CONSTRAINED TOPOGRAPHIC ICA FOR SEPARATION OF EPILEPTIC EEG

3.1 Introduction

ICA for EEG Signal Separation

Independent component analysis (ICA) has been increasingly employed for brain signal analysis and has been fruitful for decomposition of multichannel EEGs to obtain the desired source signals [47]. Application of ICA to EEG has been used for many purposes, such as source localization [48] [49], seizure signal separation [52] - [54], tracking of epileptiform activity [55], and removal of artifacts [56]- [58].

For conventional ICA, the identification of ICs, especially those approximating the desired sources, is a problem to be solved. In the most commonly used method, the desired ICs are selected by a post-processing based upon the special statistical features of the sources. Shoker et al. [56] proposed a method which combined BSS and support

vector machine (SVM) to remove the eye blink artifacts from the EEGs. The components related to eye blink artifacts were identified from the estimated sources based on classification of the features corresponding to the eye blink. The artifact-free EEG signals were reproduced by setting the artifact components to zero and remixing the remaining signals. Nakamura [57] applied four ICA algorithms to separate the EEG signals for removing ballistocardiogram (BCG) artifacts from EEG. The BCG artifacts were selected by first visually checking the time course of the ICs, then bandpass filtering the ICs with a certain frequency range (11Hz - 17Hz) for BCG artifacts. The artifact-free EEGs were recovered by back projection of sources after removal of the BCG components. In the applications to epileptic seizure separation, the seizure components can be identified by examining the rhythmical activity of the components provided that the frequency range of the epileptic seizure is known as a *priori* [52] [53]. A method of nonlinear analysis has also been exploited to distinguish the seizure components. In [53] [54], complexity measurement proposed by Roberts [51] was applied to investigate the nonlinear dynamic change of the components prior to seizure onset. The ICs for which the complexity decreased prior to seizure and the rhythmical activity matched with the seizure frequency range were selected as the seizure components. These post-processing methods involve redundant computation due to examining the unnecessary signals, which can be time consuming especially in high dimensional applications.

A practical alternative to extract the desired ICs is to incorporate the available knowledge (prior information) of the desired sources as the constraint into the ICA separation process, which is referred to as

the constrained ICA [61]. In the general framework of the constrained ICA, the prior information can be added into the original cost function in the form of equality or inequality constraints. The optimal solution of the overall constrained function can be found by using the Lagrange multiplier method [61] [69]. In some applications [49] [50] [62] [64] [69] [125], the prior information of the desired source was used to construct a rough template or a reference signal. Then the optimal solution of the constrained ICA is the IC closest, in the Euclidean distance sense, to the reference.

Topographic ICA

Theoretically, the conventional ICA model is built based on statistical assumptions: 1) the source signals are statistically independent; 2) at most one of the constituent sources has Gaussian distribution; 3) the number of independent components is less than or equal to the number of input channels [65]. However, practically, the assumption of statistical independence between the sources can not hold in some real applications such as that for brain signal separation. Generally, the multichannel EEG recordings reveal the sum of the electrical current potentials spontaneously generated by cortical nerve cells, and those cells "communicate" with each other by means of electrical or chemical activities. Once a neural cell is fired, the information is transferred to the nearby cell via a small amount of electrical charge or by releasing chemicals. Therefore, physiologically, the neural cells which are geometrically close to each other have very sophisticated connections. However, this kind of connection is usually ignored in most existing ICA models by simply assuming that all sources are statistically inde-

pendent. Hence, a model which can take such dependency between the nearby ICs into account is more reasonable for brain signal separation.

Topographic ICA (TICA) proposed by Hyvärinen et al. [66] is a modified ICA model, which is also considered as a generalization of the model of independent subspace analysis (ISA) [67]. TICA relaxes the assumption of statistical independency of the components, considering that the components geometrically close to each other are not completely independent but have certain dependencies, which can be defined by a certain neighbourhood function. In the output, the nearby sources are grouped together. In this study, TICA was applied for the separation of the epileptic seizure EEGs, and the performance was improved by introducing novel spatial and frequency constraints in TICA. In the following sections, the constrained TICA is denoted as CTICA.

This chapter is organized as follows. First, the principle of the TICA model is explained. Then the CTICA model is developed. The experimental results obtained by applying the proposed method to the simulated data and real epileptic seizure EEG are then presented. The discussion and conclusion are provided in the final section.

3.2 Method

3.2.1 Topographic ICA

Recall that the conventional noise-free ICA generative model can be expressed as:

$$\mathbf{x}(t) = \mathbf{A}\mathbf{s}(t), \tag{3.2.1}$$

where $\mathbf{x}(t) = [x_1(t), x_2(t), ..., x_n(t)]^T$, $\mathbf{x} \in \Re^n$ is the vector of observed signals at time t, $(\cdot)^T$ denotes transpose operation, $\mathbf{s}(t) = [s_1(t), s_2(t), ...,$

$s_m(t)]^T$ is the unknown independent source vector ($\mathbf{s} \in \Re^m$ and $m \leq n$), and $\mathbf{A} \in \Re^{n \times m}$ is the mixing matrix. The estimated sources $\mathbf{y}(t) = [y_1(t), y_2(t), ..., y_m(t)]^T$ can be obtained by a separation matrix $\mathbf{W}$ through inversion of the above mixing model,

$$\mathbf{y}(t) = \mathbf{W}\mathbf{x}(t) \tag{3.2.2}$$

where in an ideal case $\mathbf{W} = \mathbf{A}^\dagger$ is the pseudo-inverse of the mixing matrix and $\mathbf{WA} = \mathbf{I}$. In conventional ICA, the sources are assumed to be completely statistically independent, and the estimated signals have no particular order. In TICA, the assumption of independence of the components is relaxed, meaning that the sources geometrically far from each other are considered approximately independent and those close to each other are assumed to have certain dependencies. The dependency can be defined by higher-order correlation between the estimated sources, such as the correlation of their energies [66]:

$$cov(s_i^2, s_j^2) = E\{s_i^2 s_j^2\} - E\{s_i^2\}E\{s_j^2\} \neq 0 \tag{3.2.3}$$

where $cov(\cdot)$ is the covariance of the two sources s_i and s_j, and $E\{\cdot\}$ is the statistical expectation operator. Therefore, the estimated sources from the TICA are still uncorrelated, but their energies are not.

The concept of addressing the dependency using the high order features is similar to independent subspace analysis (ISA) [67], in which the components in each subspace are assumed to be dependent, and the feature subspace can be represented by a set of orthogonal basis vectors. The value of the feature can be calculated as $\sum_{i=1}^{d}(\mathbf{w}_i^T\mathbf{x})^2$, where d is the dimension of the subspace. In ISA model, for the data vector

$\mathbf{x}(t), t = 1, ..., N$, the logarithm, generally natural, of the likelihood can be expressed as [65]:

$$logL(\mathbf{W}) = \sum_{t=1}^{N} \sum_{j=1}^{N_s} logp(\sum_{i=1}^{d} (\mathbf{w}_i^T \mathbf{x}(t))^2) + Nlog(|det\mathbf{W}|) \quad (3.2.4)$$

where N_s is the total number of subspaces, $\mathbf{w}_i$ is the i-th column of $\mathbf{W}$, and $p(\cdot)$ refers to the probability density function.

The TICA model is illustrated in Fig. 3.1. In the model, the variances of components are not constant, but instead, they are generated by some high-order independent variables $u_i, i = 1, 2, 3$. These variables are mixed linearly in the topographic neighbourhood, which is defined by a neighbourhood function $h(i, j)$, $i, j = 1, 2, 3$. The mixtures are then transformed by a nonlinearity function $G(\cdot)$. The components s_i with different variance σ_i^2 are finally linearly mixed to form the observed variables x_i. Based on this model, the estimated components in the same neighbourhood are energy correlated.

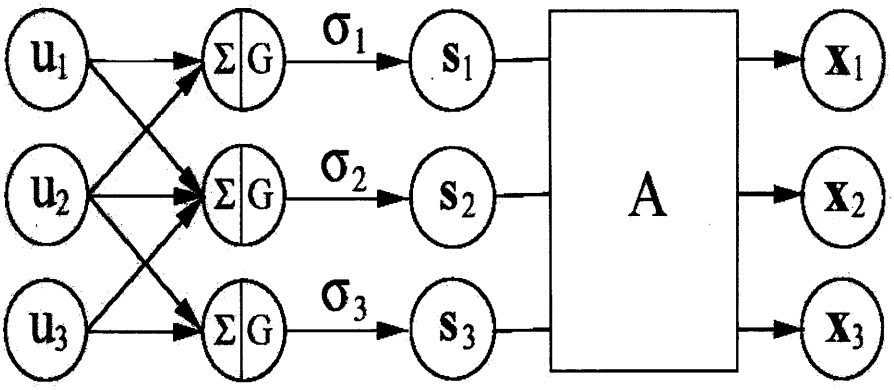

Figure 3.1. Illustration of TICA model. The component s_i is generated by the nonlinear transformation of the variables u_i, which are mixed linearly according to the neighbourhood function [66].

In this work $G(\cdot)$ is selected as defined in [66]:

$$G(y) = -\alpha\sqrt{\epsilon + y} \tag{3.2.5}$$

where α and ϵ are scalar constants. The neighbourhood function $h(i,j)$ which specifies the geometrical relationship between sources s_i and s_j in topography is usually defined as a monotonically decreasing function of some distance measurement. In this study, a simple neighbourhood function is applied, such that

$$h(i,j) = \begin{cases} 1 & \text{if } |i-j| \leq m \\ 0 & otherwise. \end{cases} \tag{3.2.6}$$

where m is the width of the neighbourhood.

In TICA model, the approximation of the joint density of the vector of sources $\mathbf{s}$, denoted as $\tilde{p}(\mathbf{s})$, is then expressed as [66]

$$\tilde{p}(\mathbf{s}) = \prod_{j}^{n} exp(G(\sum_{i}^{n} h(i,j)s_i^2)), \tag{3.2.7}$$

where $h(i,j)$ is the neighbourhood function, $\mathbf{s} = [s_1, s_2, ..., s_n]^T$, n is the number of sources, and $G(\cdot)$ is the scalar function defined by Eq. (3.2.5). For the whitened data, the approximation of the log-likelihood of TICA model, denoted as $\tilde{L}(\mathbf{W})$, is given as

$$log\tilde{L}(\mathbf{W}) = \sum_{t=1}^{N}\sum_{j=1}^{n} G(\sum_{i=1}^{n} h(i,j)(\mathbf{w}_i^T\mathbf{z}(t))^2) + Nlog(|det\mathbf{W}|) \tag{3.2.8}$$

where $\mathbf{z}(t)$ is the vector of whitened measurements as defined in Eq. (1.3.5). It is noticed that the difference between ISA and TICA is that TICA considers each neighbourhood as one subspace; the dependence is not only inside the d subspace but among all neighbouring components.

Therefore, the optimal solution $\mathbf{W}_{opt}$ for estimation of TICA is obtained when the above log-likelihood function is maximized. It is noticed that the unmixing matrix needs to be constrained to be orthogonal such that the second term of the above equation can be ignored as the determinant of an orthogonal matrix is one. Thus, the log-likelihood of Eq. (3.2.8) can be maximized by:

$$\frac{\partial}{\partial \mathbf{W}} log\tilde{L}(\mathbf{W})|_{\mathbf{W}=\mathbf{W}_{opt}} = 0 \tag{3.2.9}$$

The computation of the gradient is reduced to calculation of the gradient of

$$F_j(\mathbf{W}) = G(\sum_{i=1}^{n} h(i,j)(\mathbf{w}_i^T \mathbf{z}(t))^2) \tag{3.2.10}$$

with respect to the component $\mathbf{w}_k$, which is the k-th column vector of $\mathbf{W}$,

$$\nabla_{\mathbf{w}_k} F_j = 2g(\sum_{i=1}^{n} h(i,j)(\mathbf{w}_i^T \mathbf{z}(t))^2) h(k,j)(\mathbf{w}_k^T \mathbf{z}(t))\mathbf{z}(t) \tag{3.2.11}$$

where $g(\cdot)$ is the first order derivative of the scalar function $G(\cdot)$. The final gradient of Eq. (3.2.8) is obtained as:

$$\nabla_{\mathbf{w}_k}(log\tilde{L}(\mathbf{W})) = 2\sum_{t=1}^{N} \mathbf{z}(t)(\mathbf{w}_k^T \mathbf{z}(t)) \sum_{j=1}^{n} h(k,j) g(\sum_{i=1}^{n} h(i,j)(\mathbf{w}_i^T \mathbf{z}(t))^2) \tag{3.2.12}$$

Based on the model, one advantage of TICA is that it can group the nearby sources due to the relaxation of the assumption of independency. However, the performance of TICA has certain limits, such as the effect of grouping ICs may not be that significant unless the nearby sources

are active at the same time. In [66], in order to demonstrate the effect of grouping sources, the experiment was designed to generate some typical high energy sources such as by biting teeth for 20 seconds to create myographic artifacts. But in most real applications, the energy of the active sources may not be very significant, or there may be only one or two active desired sources. Then the performance of grouping the nearby sources may not be that significant. However, the performance can be improved to some extent by introducing certain constraints into the separation process of TICA.

3.2.2 Constrained Topographic ICA

CTICA

Adding prior information as a constraint to conventional ICA has been previously explored in EEG signal separation and analysis [50] [62] [63]. For EEG signal separation, incorporating suitable prior knowledge into the separation process can help to reduce the indeterminacies and thereby extract the desired sources. The general form of the constrained TICA can be expressed as:

$$\max\ J_m(\mathbf{W})\ \text{ subject to }\ J_c(\mathbf{W}) \tag{3.2.13}$$

where $J_m(\mathbf{W})$ is the main cost function, which is based on the TICA model as in Eq. (3.2.8). $J_c(\mathbf{W})$ is the constraint cost function, which is defined as the function of the closeness between the estimated sources y_i and a reference signal y_r. The common and simple measurement of closeness of two signals can be their Euclidean distance norm, over some time interval, or the correlation between them, which requires both y_i

and y_r to be normalized to have the same mean and variance [64] [69]. The optimal solution of the constrained algorithm provides the sources as close to the reference signal as possible.

In this study, the constrained cost function $J_c(\mathbf{W})$ is defined as the squared Euclidean norm between the estimated sources and the reference signal:

$$J_c(\mathbf{W}) = \sum_{t=1}^{N} \sum_{i=1}^{n} \|\mathbf{w}_i^T \mathbf{z}(t) - y_r(t)\|_2^2 \tag{3.2.14}$$

where $\mathbf{z}(t)$ is the vector of whitened data, the reference signal $y_r(t)$ is defined based on the spatial and frequency constraints, and $\|\cdot\|_2$ denotes Euclidean norm. The idea behind generation of the reference signal is explained in the following section. The overall cost function is then written as:

$$J(\mathbf{W}, \Lambda) = J_m(\mathbf{W}) + J_c(\mathbf{W}, \Lambda) \tag{3.2.15}$$

where $\Lambda = diag\{\Lambda_{ii}\}, i = 1, ..., n$, is a diagonal weight matrix, which is updated iteratively based on

$$\Lambda = p \cdot diag\{|cor(y_r(t), y_1(t))|, ..., |cor(y_r(t), y_n(t))|\} \tag{3.2.16}$$

where $y_1(t), ..., y_n(t)$ are the estimated sources, $|\cdot|$ is the absolute value, and $cor(\cdot)$ denotes the correlation measured by the correlation coefficient. In this equation, p is a positive weight parameter to adjust the contribution of the constraint term to the overall cost function. Both $y_r(t)$ and $y_i(t)$, $i = 1, ..., n$, are normalised to have unit variance and zero mean. To form $J_c(\mathbf{W}, \Lambda)$, Eq. (3.2.14) is modified to become

$$J_c(\mathbf{W}, \Lambda) = \sum_{t=1}^{N} \sum_{i=1}^{n} \Lambda_{ii} \|\mathbf{w}_i^T \mathbf{z}(t) - y_r(t)\|_2^2 \tag{3.2.17}$$

The optimal solution can be found by using the steepest descent adaptive learning algorithm [83], and the update equation is:

$$\mathbf{W}(k+1) = \mathbf{W}(k) - \mu\{\frac{\partial J_m(\mathbf{W})}{\partial \mathbf{W}} + \frac{\partial J_c(\mathbf{W}, \Lambda)}{\partial \mathbf{W}}\} \tag{3.2.18}$$

where μ is the empirically chosen learning rate, k is the iteration number, and $\frac{\partial J_c(\mathbf{W},\Lambda)}{\partial \mathbf{W}}$ is calculated as $\Lambda(k)(\mathbf{Z}(\mathbf{W}^T(k)\mathbf{Z} - \mathbf{Y}_r)^T)$, where $\mathbf{Z} = [\mathbf{z}(1), \mathbf{z}(2), ..., \mathbf{z}(N)]$, and $\mathbf{Y}_r = [\mathbf{y}_r(1), \mathbf{y}_r(2), ..., \mathbf{y}_r(N)]$, which is a matrix with the reference signal $\mathbf{y}_r$ in each row.

Fig. 3.2 shows a block diagram of the CTICA algorithm. The source signals $\mathbf{s}(t)$ are first mixed by an unknown mixing matrix $\mathbf{A}$, the mixed signals and noise $\mathbf{n}(t)$ are recorded at sensors $\mathbf{x}(t)$. Then the observed data are preprocessed by removing the mean and prewhitening (by performing PCA). The whitened data $\mathbf{z}(t)$ have unit variance. A reference signal $\mathbf{y}_r(t)$ is constructed based on the observed data. The adaptive learning algorithm updates the unmixing matrix $\mathbf{W}$ based on the CTICA model until the optimal solution is obtained.

Reference Signal

In this work, a reference signal as an approximation of the desired source, is introduced into the constrained learning process. The reference can be a signal which carries some information to distinguish the desired components but is not necessarily identical to the desired sources [61] [64]. In some applications, it may be very difficult to find an ideal template for the desired source. For example, in some applica-

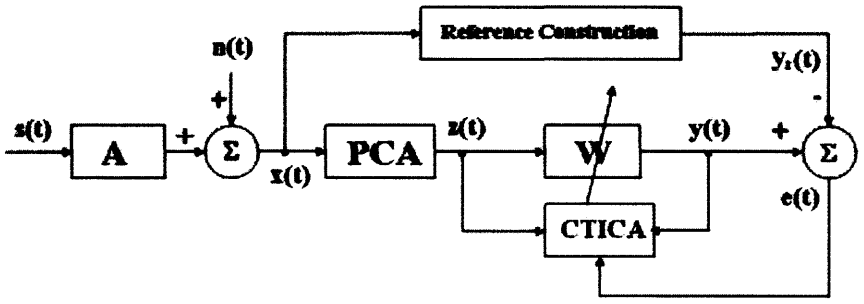

Figure 3.2. Block diagram illustrating the generation of the sources, the whitening process, the CTICA algorithm together with the reference generation.

tions of event-related fMRI in which the designed stimulus is applied, the stimulus is directly used as the reference and the desired sources are selected by evaluating the correlation between the estimated sources and the reference signal [64] [125].

Here, the reference constructed from scalp EEGs was introduced as a 'rough' template of the seizure source, which was built based on averaging the filtered scalp EEGs obtained from the seizure area. In practice, it is difficult to obtain an ideal seizure template. Although EEG recorded from the scalp contains the noise and artifacts, it still carries very valuable information about the seizure. So far, EEG is still the most powerful tool for the diagnosis of epileptic seizure in the clinical field [81] [96]. The sources obtained by CTICA are not only separated from artifacts and noise, but also enforced to be close to the reference.

In this work, the reference signal was built based on averaging the filtered scalp EEGs obtained from the epileptogenic zone (seizure area). Two factors were considered based on spatial and frequency information of the seizure signals. Firstly, in focal epileptic seizure, the approximate location of seizure sources, "epileptogenic zone", is often known as the prior information. Secondly, it has been known that the seizure signals manifest themselves within a certain frequency band [74]. Based on research findings the frequency band of the epileptic seizure onset is normally from 2.5 Hz to 15.5 Hz, although this range may vary or be narrowed for different types of seizures [74]- [76]. The reference signal built in this way is the signal which includes both spatial and frequency information. Therefore, the desired source is the one that not only falls within a frequency range, but also reflects the dynamical changes within

the epileptogenic zone.

3.3 Experiments

Three experiments were carried out to investigate the performance of the CTICA algorithm. The first experiment is the simulation test to demonstrate how TICA works for grouping the nearby sources, which is the main advantage of TICA over conventional ICA algorithms. Five sources were generated and mixed by a designed mixing matrix as explained in the following section, such that three sources were geometrically close to each other. The simulation results show that these three sources are grouped together at the output. Signal-to-noise-ratio (SNR) and performance index (PI) were employed to evaluate the separation performance of TICA and CTICA. The comparison of TICA and CTICA for separation of real EEG data with epileptic seizure was carried out in the second experiment. The seizure components were identified by a hybrid system including the complexity measurement of components [51] [53] [54], time-frequency analysis, and component back projection (topographic map). The results demonstrate that CTICA achieves better separation performance than TICA. In the third experiment, CTICA was compared with other ICA algorithms. The results show as expected that the component extracted from CTICA has the highest correlation with the reference signal.

In all experiments, the mean of data was removed first. Then preliminary whitening was performed to make the data have unit variance before further separation processing. The unmixing matrix was initiated as a random matrix, which was constrained to be orthogonal by performing $(\mathbf{W}\mathbf{W}^T)^{-1/2}\mathbf{W}$ in each learning iteration, thus the second

term in Eq. (3.2.8) can be cancelled [66]. Hence, the unmixing matrix has unit norm and unit variance. The parameters used in all experiments were set up as follows: In Eq. (3.2.5), parameters α and ϵ of the scalar function $G(\cdot)$ are chosen respectively as 1 and 0.005 according to [66]. The adjusting parameter p in Eq. (6.3.14) was chosen between 6 and 10 based on the algorithm performance. The width of the neighbourhood was used as $m = 1$.

3.3.1 Experiment I

The simulation test was carried out in the following steps: (1) designing a mixing system which can present the locations of the sources; (2) generating the sources based on the TICA model such that the sources which are geometrically close to each other are energy correlated; (3) comparing the results from TICA and CTICA in terms of SNR and PI.

In the simulation, the accuracy of the recovered ICs compared to the sources was evaluated in terms of signal-to-noise-ratio (SNR) in dB as [69]

$$SNR = 10log_{10}(\frac{var(\mathbf{s}(t))}{MSE}) \tag{3.3.1}$$

where $var(\cdot)$ denotes the variance of the source, and MSE denotes the mean square error between the generated and recovered signals. The separation performance was measured by the performance index (PI) [69] as

$$PI = \frac{1}{n}(\sum_{i=1}^{n}(\sum_{j=1}^{n}\frac{|p_{ij}|}{max_k|p_{ik}|} - 1) + \sum_{j=1}^{n}(\sum_{i=1}^{n}\frac{|p_{ij}|}{max_k|p_{kj}|} - 1)) \tag{3.3.2}$$

where p_{ij} is the $(i,j)th$ element of the permutation matrix $\mathbf{P}=\mathbf{WA}$. PI is close to zero if all components are perfectly separated.

Mixing System

In this experiment, a mixing system based on the real EEG 10-20 recording system was first constructed. By using the coordinate of the real EEG recording system, the sources were arranged in some pre-defined locations. An example of such arrangement is given in Fig. 3.3. Five sources were generated, in which $\mathbf{s}_1$, $\mathbf{s}_2$ and $\mathbf{s}_3$ were arranged to be close to each other, and $\mathbf{s}_4$ and $\mathbf{s}_5$ were far away from each other. The mixed signals were recorded at the five sensors $\mathbf{x}_1$ to $\mathbf{x}_5$. The locations of the sensors $\mathbf{x}_1$ to $\mathbf{x}_5$ were based on the coordinates of the electrodes F7, F3, Fz, F4 and F8 in the real EEG 10-20 recording system, respectively. The placement of the electrodes can be found in Fig. 1.4. Table 3.1 provides the coordinates of the sensors which can be found from the open source software EEGLAB [70], and Table 3.2 gives the coordinates of the generated sources. In the coordinates, x is towards the nose, y is towards the left ear, and z is towards the vertex.

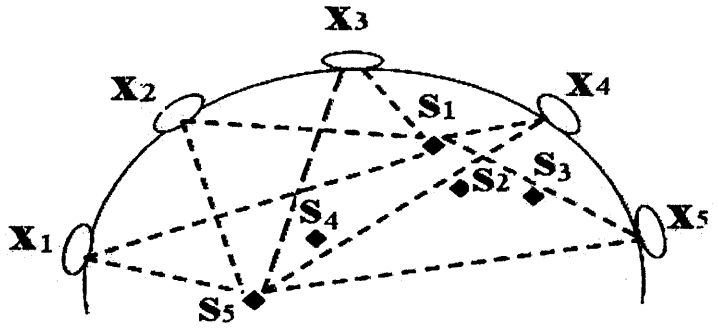

Figure 3.3. Schematic diagram of a brain mixing system including the sources $\mathbf{s}_1$-$\mathbf{s}_5$ and the sensors $\mathbf{x}_1$-$\mathbf{x}_5$.

The mixing matrix $\mathbf{A}$ is specially designed in order to model the source signal propagation process. The entries of the mixing matrix are defined as $\mathbf{A}_{ij} = 1/d_{ij}^2$, where d_{ij} is the distance between the i^{th}

Table 3.1. The coordinates of the sensors.

Sensors	$\mathbf{x}_1$	$\mathbf{x}_2$	$\mathbf{x}_3$	$\mathbf{x}_4$	$\mathbf{x}_5$
X	0.586	0.677	0.714	0.677	0.587
Y	0.804	0.567	0.000	-0.567	-0.804
Z	-0.088	0.469	0.699	0.469	-0.088

Table 3.2. The coordinates of the generated sources.

Sources	$\mathbf{s}_1$	$\mathbf{s}_2$	$\mathbf{s}_3$	$\mathbf{s}_4$	$\mathbf{s}_5$
X	0.520	0.605	0.487	0.055	-0.123
Y	-0.650	-0.595	-0.536	0.087	0.325
Z	0.125	0.278	0.207	0.179	0.332

sensor and the j^{th} source. This design is based on the conjecture of signal propagation that the source signal strength decreases with the square of the distance from the sensor. A similar model for the signal propagation has been used in [71] [72].

Generation of the Sources

Special consideration has been taken for generating the energy correlated sources. According to the simulation in [66], the signals were generated based on the TICA model (as shown in Fig. 3.1). The variables u_i were firstly generated by taking absolute values of the Gaussian variables, then mixed according to the model. The neighbourhood function and the nonlinear function G were used as defined in Eq. (3.2.6) and Eq. (3.2.5) with $\alpha = 1$ and $\epsilon = 0.005$. The sources $\mathbf{s}_1$ and $\mathbf{s}_2$ generated in this way are energy correlated ($cov(\mathbf{s}_1^2, \mathbf{s}_2^2) \neq 0$).

Results

Fig. 3.4 shows five artificial simulated sources. $\mathbf{s}_1$ and $\mathbf{s}_2$ were energy correlated with the covariance $cov(\mathbf{s}_1^2, \mathbf{s}_2^2) = 35.88$ and the other three sources were uncorrelated. In order to demonstrate the performance of

TICA, $\mathbf{s}_1$, $\mathbf{s}_2$ and $\mathbf{s}_3$ were arranged to be close to each other and close to the sensors $\mathbf{x}_3$, $\mathbf{x}_4$ and $\mathbf{x}_5$. $\mathbf{s}_4$ and $\mathbf{s}_5$ were located far away from the sensors (as in Fig. 3.3). Five sources were mixed by the above designed matrix $\mathbf{A}$ and the mixed signals are shown in Fig. 3.5. The estimated sources are given in Fig. 3.6, which shows that IC1, IC2 and IC3 are grouped together. Here, $\mathbf{s}_3$ was set to be close to $\mathbf{s}_1$ and $\mathbf{s}_2$. It is noticed that although $\mathbf{s}_3$ is energy uncorrelated with $\mathbf{s}_1$ and $\mathbf{s}_2$, it is still grouped with them. It shows that TICA can group the sources if they are geometrically close to each other although they might not be reasonably energy correlated.

In order to test CTICA, a sensor signal $\mathbf{x}_5$, which has the highest correlation coefficient with $\mathbf{s}_1$, was selected to be the reference signal. The comparison of separation performance is given in Table 3.3, with the results obtained by averaging five trials. (The reason of running a number of trials is to take into account the random initial condition of the unmixing matrix.) The SNRs were computed for the recovered and original sources. It can be seen that the value of PI from CTICA is less than that from TICA. The results of SNRs and PI indicate that a better separation is obtained from CTICA.

Table 3.3. Comparison of SNR and PI for TICA and CTICA algorithms.

	SNR(dB)					PI
	$\mathbf{s}_1$	$\mathbf{s}_2$	$\mathbf{s}_3$	$\mathbf{s}_4$	$\mathbf{s}_5$	
TICA	17.7912	9.5819	35.7823	8.6754	21.6763	0.6440
CTICA	21.7270	11.6819	33.9634	11.2131	22.4799	0.4226

The correlation coefficients between five recovered sources and the reference signal are given in Table 3.4. It can be seen that the source IC1 (recovered for $\mathbf{s}_1$) has the highest correlation with the reference

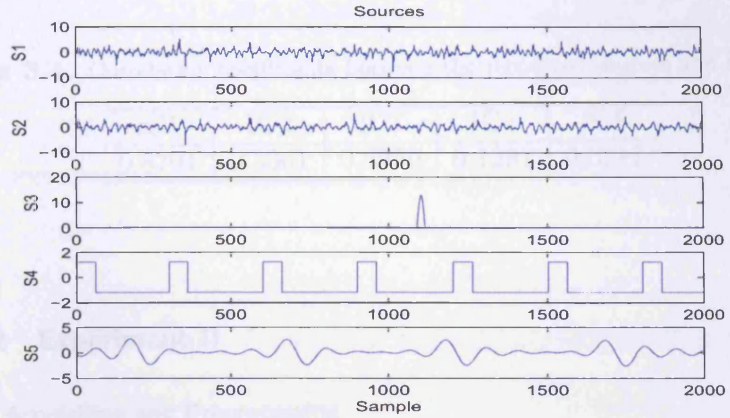

Figure 3.4. Simulated source signals

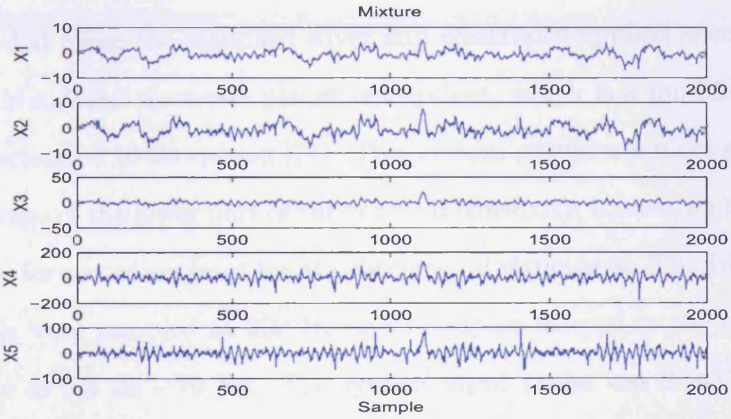

Figure 3.5. The mixture of the simulated sources.

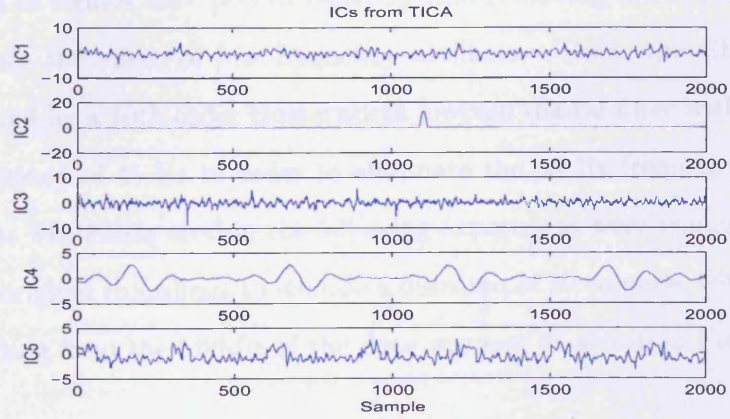

Figure 3.6. The estimated source signals obtained by TICA.

signal.

Table 3.4. Correlation coefficients between the recovered sources and the reference.

IC1	IC2	IC3	IC4	IC5
0.8701	0.3361	0.3359	0.1291	0.0217

3.3.2 Experiment II

Data Acquisition and Preprocessing

The multichannel EEGs with the frontal focal epileptic seizure were recorded using the standard silver cup electrodes applied according to the 'Maudsley' electrode placement system, which is a modification of the extended 10-20 system [77]. This system provides a more extensive coverage of the lower part of the cerebral convexity, increasing the sensitivity for recording from basal subtemporal structures. The 16-channel EEGs were sampled at 200 Hz and bandpass filtered in the frequency range of 0.3 Hz - 70 Hz. The system input range was 2 mV and the data were digitized using a 12-bit analog-to-digital converter [42].

The signals were preprocessed by first removing the baseline to alleviate the effect of low frequency artifacts. Then, the EEGs were filtered by a $10th$ order Butterworth lowpass digital filter with an edge frequency of 45 Hz in order to eliminate the 50 Hz frequency component. The EEGs used in the following experiment were truncated from the original recordings to include a duration of 10 seconds, with seizure starting from the middle of the data segment as shown in Fig. 3.8.

Number of Sources

Generally, it is difficult to estimate the exact number of brain sources. But as Cichocki pointed out [11], it is not always necessary and desirable in ICA to separate all the sources contained in the matrix, especially in the situation for which only a few most powerful sources are of interest, which is the case in this work where only the seizure components are of interest. In a number of experiments for epileptic seizure separation [52] - [54] where the number of sensors were taken as 30, 25 and 12, the number of detected seizure sources were 3, less than 5 and less than 3, respectively. In these results, the number of seizure components was much less than the number of input channels, and one only needed to identify a few seizure components from the output of ICA.

In this work, in order to investigate this problem, the method proposed by Bai and He [14] was applied to estimate the number of sources. This method applied an information theoretic criterion to the eigenvalues of the covariance matrix of EEGs to estimate the number of sources. (This method has been introduced in the first chapter and the detail can be found in [14]). This method involves the following steps. Firstly, all the eigenvalues of the covariance matrix were obtained by using singular value decomposition (SVD). Secondly, the information criterion value (ICV) with the eigenvalues was calculated based on the proposed method. Lastly, according to the rule of the information criterion method, the number of sources with minimum ICV was selected as the estimated number of sources. By applying this method, the estimated number of sources was 10 (as shown in Fig. 3.7). This shows that the number of sources should be taken as 10 or more. In this experiment, the number of input channels is 16. In order to use the

available information in EEGs as much as possible and fully investigate the separated sources, the number of sources in this experiment was selected as 16.

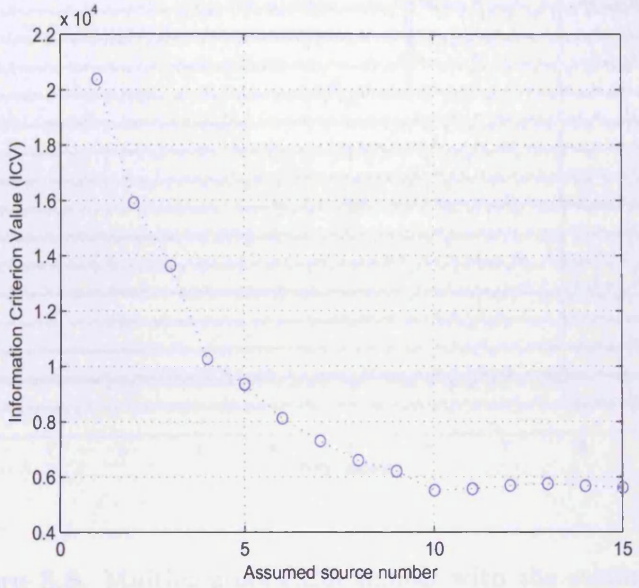

Figure 3.7. Estimation of the number of sources by applying information criterion method [14].

Selection of Seizure Components

The separation result from TICA is given in Fig. 3.9. The seizure components were selected based on the following steps:

(1) Visually checking the time course of each component. Some artifacts, may be easily distinguished in the first check due to exhibiting different rhythmic activity with the seizure.

(2) Looking for the change in the complexity which coincides with the seizure onset. The detail of the complexity measurement is explained in the Appendix. Based on the nonlinear characteristics of the seizure signal, the complexity is expected to gradually drop prior to the

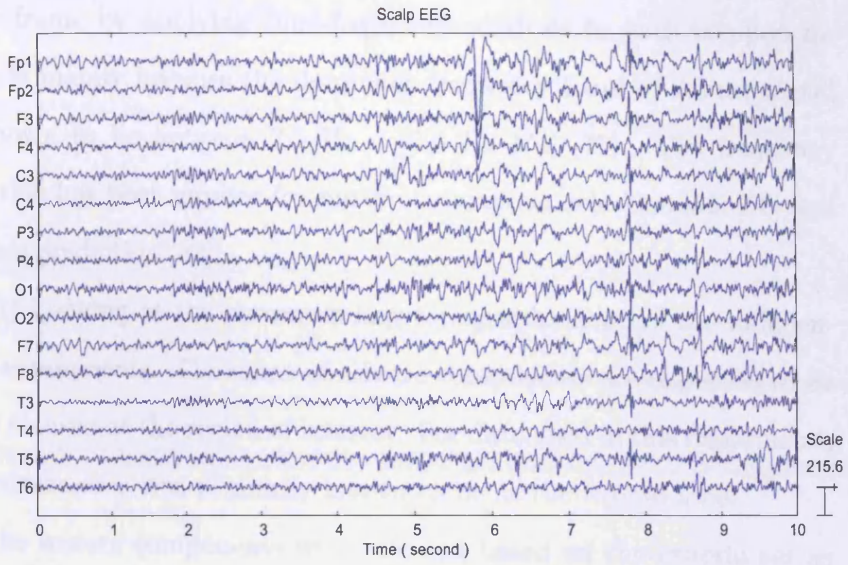

Figure 3.8. Multichannel EEG signals with the seizure onset.

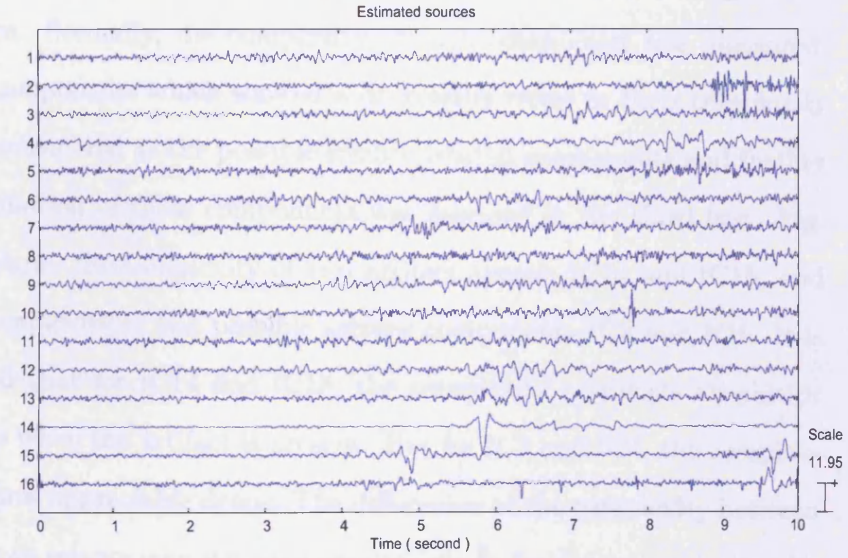

Figure 3.9. The source signals estimated by TICA.

seizure onset.

(3) Looking at the rhythmic activity (frequency) in the appropriate time frame by applying time-frequency analysis to each component. This is mainly because the dominant frequency band of seizure signal is known to be between 2.5 Hz - 15.5 Hz [74] [75]. The frequency criterion has been applied for seizure component selection [52] [63] and seizure prediction [43].

(4) Looking at the corresponding topographic map of the independent components. The maps of seizure components are expected to be more focused at the region of interest. For data used in this experiment, the seizure area was primarily known to be at the frontal lobe.

The seizure components were selected based on the criteria set as above. Firstly, by examining the time course of the components, some components such as IC14 and IC15 obviously do not belong to the seizure. Secondly, the complexity of each component was measured. The components which showed a decreasing trend in their complexity were considered as the possible seizure-related components and further confirmation of these components was assessed in the third test. Fig. 3.10 shows the complexity of two artifact signals IC14 and IC15, and the complexity of two possible seizure components IC3 and IC4. It is noticed that for IC14 and IC15, the complexity manifests an abrupt change when the artifact is present. But for IC3 and IC4, the complexities show appreciable drops. The differences of the complexity between these two seizure components can also help in further investigating the possible evolution of the seizure. The results of complexity changes related to artifacts and seizure components are also accordant with those presented in the literature [53] [54].

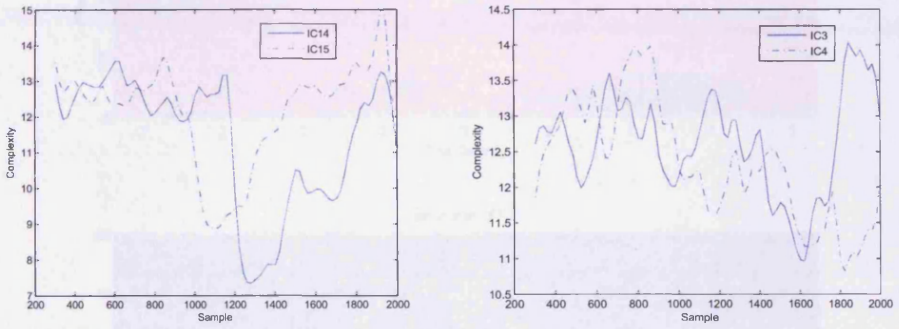

Figure 3.10. Measurement of complexity. The left figure shows the complexity for two artifact components IC14 and IC15. In the right figure the complexity for two seizure components IC3 and IC4 is presented.

Thirdly, the time-frequency analysis was applied to the above selected components as a further test. Fig. 3.11 shows the spectrogram of IC3 and IC4. The spectrogram shows the magnitude of the short-time Fourier transform of the components. It can be found that the magnitude of the frequency is higher in the seizure band (3 Hz -15 Hz).

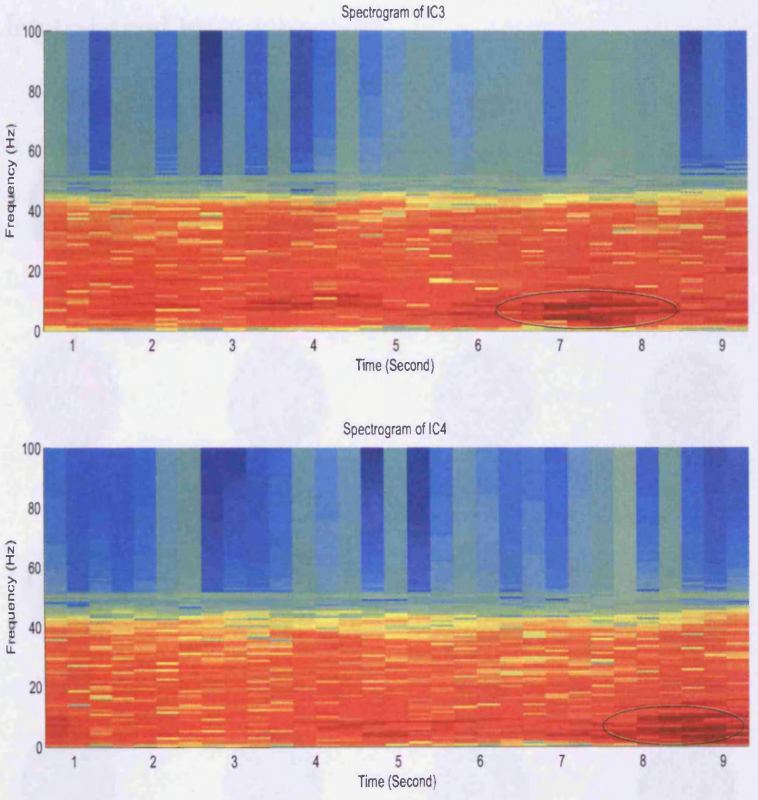

Figure 3.11. Spectrogram of seizure components IC3 and IC4.

Fourthly, the topographic maps of the estimated sources were studied (as given in Fig. 3.12). A topographic map reveals how each source signal contributes to the recordings, which can be obtained by back-projecting the estimated source onto the original signal space. For example, the back projection of IC_i is $X_p(i)$, which can be obtained

by multiplying the i-th column vector of the inverse of the unmixing matrix by the corresponding estimated source, $X_p(i) = [\mathbf{W}^{-1}]_i \mathbf{s}_i$. Fig. 3.12 gives the topographic maps of the averaged energy of each IC. It can be noticed that the distribution of ocular artifacts related component IC14 focuses on the area near the location of electrodes Fp1 and Fp2. The maps of the two seizure components IC3 and IC4 are located at the fronto-lateral brain lobes.

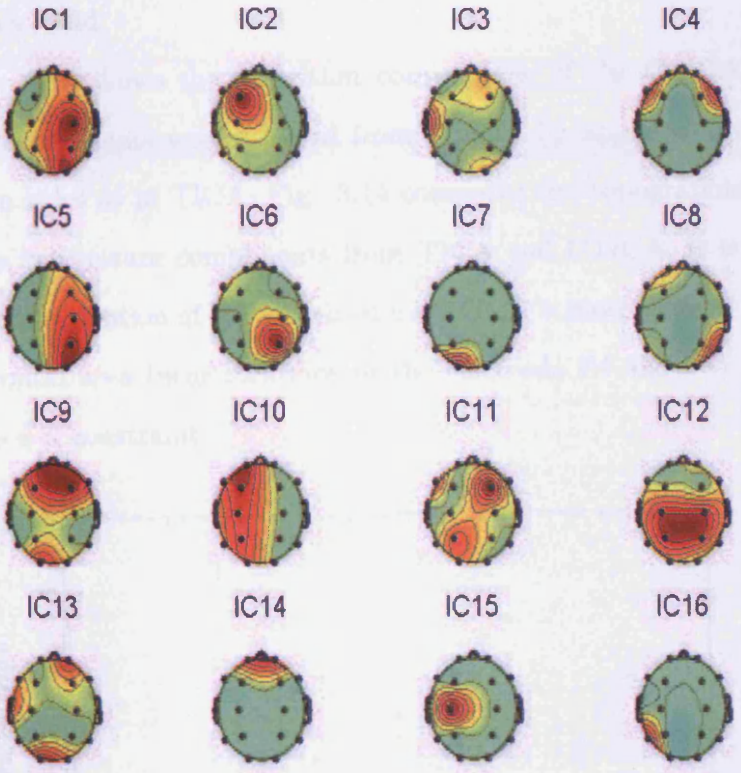

Figure 3.12. Topographic maps of the estimated EEG sources from TICA.

Results from CTICA

CTICA was applied to the same EEG data. The reference signal was formed by first averaging the channels close to the seizure area which was confirmed by our clinical consultant. In the second experiment, two electrodes F4 and F8 from the right frontal lobe were selected. Then, 3 Hz -15 Hz bandpass filtering was undertaken to ensure that the frequency components of the reference signal fall in the seizure frequency band.

Fig. 3.13 shows the algorithm convergence of the CTICA. Two seizure components were selected from CTICA by applying the same selection rules as in TICA. Fig. 3.14 compares the topographic maps of these two seizure components from TICA and CTICA. It is found that the distribution of IC3 obtained by CTICA is more focused on the right frontal area (near locations of the electrode F4 and F8) due to the effect of constraint.

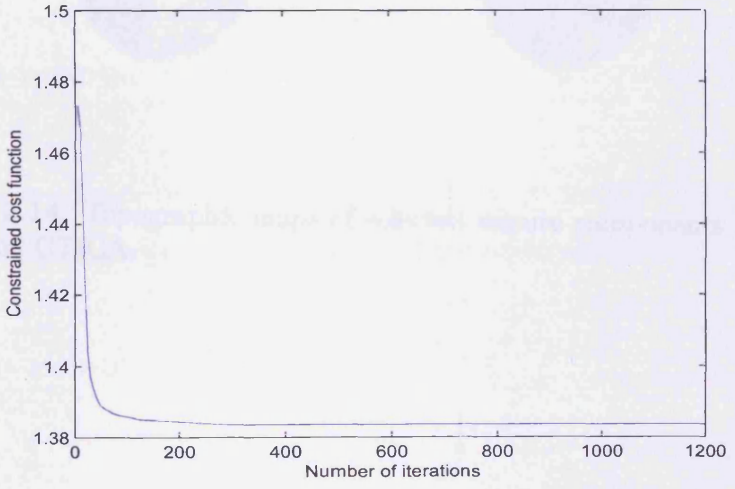

Figure 3.13. Algorithm convergence of CTICA.

The TICA and CTICA are also compared in terms of signal-to-

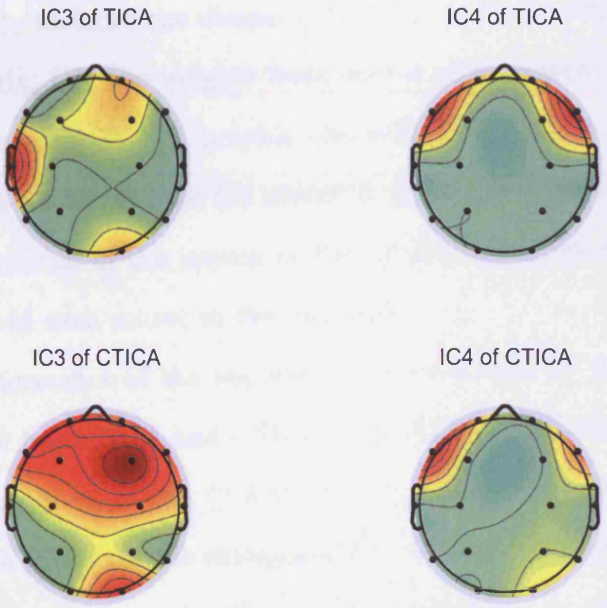

Figure 3.14. Topographic maps of selected seizure components from TICA and CTICA.

interference-ratio (SIR). SIR was defined to be the averaged signal energy for the estimated source $\mathbf{y}$ from the direct source divided by the energy stemming from the other sources. A higher value of SIR indicates better performance.

$$SIR = 10log_{10}\frac{\frac{1}{n}\sum_i^n [\mathbf{W}^{-1}]_{ii}^2 E\{y_i^2\}}{\frac{1}{n(n-1)}\sum_{i\neq j}^n \sum_j^n [\mathbf{W}^{-1}]_{ij}^2 E\{y_j^2\}} \tag{3.3.3}$$

where $[\mathbf{W}^{-1}]_{ii}$ includes the diagonal elements in the inverse of the unmixing matrix, i.e., the weights from source y_i to sensor x_i. The off-diagonal elements $[\mathbf{W}^{-1}]_{ij}$ provide the weights from the source y_j to the sensor x_i. It shows how the source y_j interferes with the source y_i, since each column of the inverse of the unmixing matrix indicates the distribution of each source in the mixtures.

The performance of the algorithm was evaluated by the average of five trials for both TICA and CTICA. The SIR was calculated based on the definition given in Eq. (3.3.3). Fig. 3.15 illustrates the separation performance (SIR) via the changes of the width of the neighbourhood. It can be noticed that, the SIR of TICA decreases as the neighbourhood width increases. This is because the wider the neighbourhood, the more sources are considered to be energy correlated. However, for the CTICA, due to the effect of the constraint, the SIR only slightly decreases at the beginning. It shows that generally, the CTICA has better performance than TICA.

3.3.3 Experiment III

In the second experiment, the results have demonstrated how TICA works for grouping nearby sources, and have shown that CTICA achieves

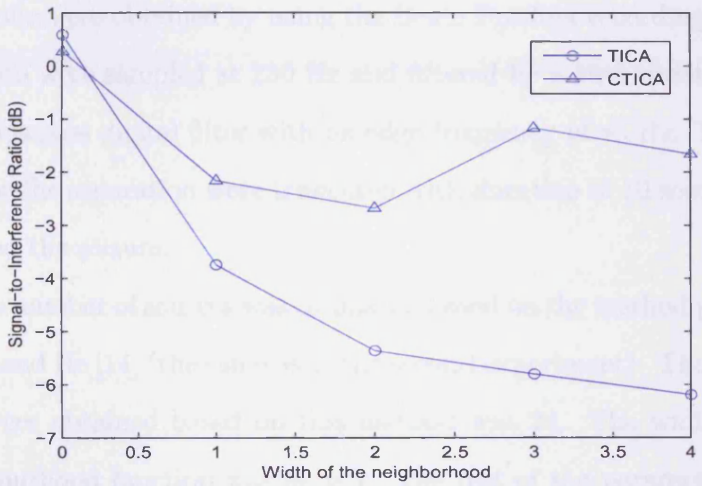

Figure 3.15. Performance comparison of TICA and CTICA.

better performance than TICA. In the third experiment, the CTICA was compared with three other ICA algorithms, TICA, JADE and FastICA. A component which had the highest absolute value of correlation with the reference signal was selected from outputs of these four algorithms. The component selected by this way is the source closest to the reference.

Data and Preprocessing

The 64-channel epileptic EEGs with the seizure area at the right temporal lobe were obtained by using the Brain Product recording system. The data were sampled at 250 Hz and filtered by a 10th order Butterworth lowpass digital filter with an edge frequency of 45 Hz. The data used for the separation were truncated with duration of 10 seconds and included the seizure.

The number of sources was estimated based on the method proposed by Bai and He [14] (the same as in the second experiment). The number of sources obtained based on this method was 24. The width of the neighbourhood function was $m = 1$. The rest of the parameters were set as in the previous experiments. The reference signal was formed by averaging and bandpass filtering the signals from two electrodes T8 and P8, which was based on the suggestion by the clinical consultant as the seizure area was known at the right temporal lobe.

Results

The source that had the highest correlation with the reference was selected from the outputs of each algorithm. Table 3.5 gives the correlation coefficients between the reference signal and the selected sources.

It can be seen that the selected IC from the CTICA has the highest correlation with the reference, although it is not significant different, which is in common with the findings in [66].

Table 3.5. Correlation coefficients between reference and the closest source.

TICA	CTICA	FastICA	JADE
0.4747	0.5512	0.5461	0.4678

3.4 Discussion and Conclusion

A novel constrained topographic ICA algorithm has been proposed for separation of the epileptic seizure signals. It not only relaxes the independence assumption of the nearby sources, but also further constrains the TICA model based on the spatial and frequency domain properties of the seizure signal by using some knowledge about the epileptic seizures in the form of an averaged and band-limited reference signal. The experimental results have shown that the CTICA algorithm achieves a better separation performance than the TICA and some other ICA algorithms.

The ambiguity problem of conventional ICA has been carefully considered. By preprocessing the data, such as centring and pre-whitening, the data were properly scaled to have unit variance. The unmixing matrix was orthogonalized. The indeterminacy in the sign of the sources has no effect on the nonlinear analysis of the sources, because the nonlinear measurement as Lyapunov exponent is invariant with respect to the change of sign.

The proposed method can be further improved by developing a more appropriate neighbourhood function based on the statistical properties

of the experimental data. More investigation in setting the proper learning parameters and applying different closeness measurements may accelerate the convergence of the algorithm.

Chapter 4

PREDICTABILITY OF EPILEPTIC SEIZURE FROM SCALP EEG

4.1 Introduction

Traditional Prediction Method

Prediction of epileptic seizure has been investigated for decades and many methods have been developed based upon the nonlinear dynamic analysis [28]- [42]. These prediction methods rely on evaluation of the chaotic behaviour of the epileptic brain. It has been shown that when the state of the epileptic brain transforms from preictal (prior to seizure onset) to ictal (during seizure onset) then to postictal (after seizure), the corresponding brain signals change from chaotic to ordered then return to chaotic [4]. Therefore, the prediction of seizure can be achieved by quantifying this nonlinear dynamic change.

The first clinical investigation of the nonlinear dynamics of epileptic seizures was reported by the group led by Iasemidis and Sackellares [28], which quantified the transition of brain stages by estimating of the short-term Lyapunov exponents (STLmax) from intracranial

EEG recordings. Other methods such as measuring the correlation dimension [32]- [34], evaluation of the similarity [35] [41], and time-frequency analysis [43] [73], have also been investigated for epileptic seizure prediction. Most of these prediction methods were developed based on analysis of intracranial EEG. This requires surgical operation to implant the electrodes inside the brain, and in order to capture the seizures, the electrodes must be placed as close to the epileptogenic zone as possible. Therefore, the method based on intracranial EEGs is not convenient, and a "warning" method based on noninvasive recordings such as scalp EEG is highly desirable.

Method of BSS for Scalp EEG

Nonlinear dynamic analysis of scalp EEG has also been investigated [36]- [40] [44]. According to these studies, a dynamic transition prior to seizure onset has been found in scalp EEG, similar to that in the intracranial recordings, which suggests the possibility of prediction by analysis of scalp EEG recordings.

The main drawback of using scalp EEG is that the signals from the scalp are contaminated by noise and artifacts. The attenuation due to the soft tissue and skull also affects the accuracy of traditional nonlinear methods for prediction. Corsini et al. [42] firstly proposed a novel approach to investigate the predictability of epileptic seizure from scalp EEG by applying blind source separation (BSS) techniques, which showed very promising results. In their method, seizures were considered as independent components of the scalp EEG, which could be separated by using a BSS algorithm. Then the traditional nonlinear analysis method for quantification of the dynamic changes by estima-

tion of STLmax was performed on these estimated sources to evaluate the predicability of seizures. The results showed that some sources presented a similar dynamic transition prior to seizure, suggesting the possibility of seizure prediction from scalp EEGs when a reliable and effective seizure source separation method is applied.

There are two problems with Corsini's method. One problem is how to identify the seizure sources. In their approach, the calculation of STLmax is performed for all separated sources due to lack of information about the seizure sources, which is computationally expensive. The second problem also relates to the overall high computational cost. In their method, in order to solve the permutation problem in BSS, a block-based BSS is executed for the overlapped data segments. After performing BSS for each segment, the correlation between the consecutive estimated source segments is measured, then the source signals for the consecutive segments are realigned. Although the overlap window method solves the permutation problem, it takes a much longer time for data processing. This is another reason why this method is practically very expensive.

In this chapter, the predictability of seizure from scalp EEG has been further investigated by applying different ICA algorithms to the epileptic EEG signals. The rest of this chapter is organized as follows. Firstly, the traditional nonlinear method for dynamic quantification based on STLmax from the EEG time series is described in detail. Secondly, the BSS approach is explained, and the JADE algorithm based on fourth order statistics is introduced. In the first experiment, the results obtained from SOBI and JADE are compared. In the second experiment, the proposed constrained topographic ICA (CTICA) is

applied to the same EEG data and the results are compared with those of the first experiment. In both experiments, the STLmax from the estimated sources and the simultaneously recorded intracranial signals are compared. In the final section, the overall work is concluded.

4.2 Estimation of Lyapunov Exponents from EEG Time Series

Iasemidis et al. [28] proposed a method for estimation of the short-term largest Lyapunov exponent (STLmax) for EEG time series. Here, "short-term" refers to estimation of the Lyapunov exponent from short length EEG data. Nonstationarity of the long EEG sequences has to be considered in relation to dynamical measurement. Iasemidis [28] states that there is a physiological time scale for brain dynamics and dynamical measurements should therefore be computed within this time scale rather than over long time intervals. In practice, a nonstationary signal can be assumed to be stationary by dividing the signal into blocks of short, pseudo-stationary segments. L. Silva et al. [45] have shown that an EEG epoch of tens of seconds duration can be considered as quasi-stationary depending on the patient's behavioural state. In the study of seizure prediction based on method of correlation dimension [32] [33], the duration of epileptic EEG was chosen as 30 seconds. In Iasemidis' experiment [28], the time duration for calculating STLmax was decided on the basis of two requirements: first, it should be as small as possible to provide the local dynamic information; second, it should satisfy the requirement of the minimum data length for calculating STLmax. Based on their tests, they found that a data duration between 10 to 12 seconds is adequate to distinguish the dynamical changes between preictal and ictal stages. And according to Wolf's paper [30], the length of

the data required to calculate the largest Lyapunov exponent (λ_1), for data with a d-dimensional attractor, should be between $10^d \sim 30^d$. For epileptic EEG time series, the attractor dimension is 2 or 3 [31], so a data length of between 1000 to 27000 samples is required for estimation of Lyapunov exponents. Therefore, the length of data was decided as 10 to 12 seconds in [28]. According to the studies in these literature, in this study, the length of data segment for measuring STLmax was selected as 10 seconds.

In order to quantify the chaotic behaviour, the dynamic system must first be reconstructed according to Takens' *delay-embedding theorem* [23]. Given an EEG data segment $\mathbf{x}(t)$ with N time points , then at time t_i, the vector $\mathbf{x}_i$ in the phase space can be constructed by:

$$\mathbf{x}_i = [x(t_i), x(t_i + \tau), ..., x(t_i + (p-1)\tau)]^T \tag{4.2.1}$$

where the value τ is the selected time lag between the elements of each vector in the phase space, p is the dimension of the embedding phase space, and $t_i \in [1, N - (p-1)\tau]$. Then, the estimation of STLmax, L, can be represented as [28]:

$$L = \frac{1}{\mathbf{N}_a \Delta t} \sum_{i=1}^{\mathbf{N}_a} log_2 \frac{|\delta \mathbf{x}_{i,j}(\Delta t)|}{|\delta \mathbf{x}_{i,j}(0)|} \tag{4.2.2}$$

where

$$\delta \mathbf{x}_{i,j}(0) = \mathbf{x}(t_i) - \mathbf{x}(t_j) \tag{4.2.3}$$

and

$$\delta \mathbf{x}_{i,j}(\Delta t) = \mathbf{x}(t_i + \Delta t) - \mathbf{x}(t_j + \Delta t) \tag{4.2.4}$$

where $\delta \mathbf{x}_{i,j}(0)$ is the displacement vector at initial time, and $\delta \mathbf{x}_{i,j}(\Delta t)$

is the evolution of this perturbation after evolution time Δt. $\mathbf{N}_a$ is the number estimated within a duration of the data segment, as $N = N_a\Delta t + (p-1)\tau$. The selection of parameters is decided as follows [28]:

• p: In the case of epilepsy, the epileptic attractor dimension d is 2 or 3 [31]. According to Takens' Theorem, the embedding dimension p has to be at least equal to $(2d+1)$, so that $p \geq (2*3+1) = 7$;

• τ: Should be small enough to capture the shortest changes, and also should be large enough to ensure possible maximum independence between the vectors in the phase space. The duration of a vector spanned in the phase space is $(p-1)\tau$, which should be at most equal to the period of the maximum frequency component in the data. In the case of an epileptic attractor, the dominant frequency component is often less than 12 Hz. Therefore, with $p = 7$, $(7-1)\tau = 1/12 \cong 83$msec, and thus τ should be approximately 14 msec.

• Δt: The evolution time should not be too small in order to follow the maximum rate of information change. If the dominant frequency component in the data is f_0, Δt is usually chosen as $1/2f_0$. For the epileptic EEG data, this gives $\Delta t = 42$ msec.

• The vector $\mathbf{x}(t_j)$: should be chosen such that the previous evolved displacement vector $\delta\mathbf{x}_{i,j}(\Delta t)$ is almost parallel to the candidate displacement $\delta\mathbf{x}_{i,j}(0)$.

4.3 Predictability of Seizure by Incorporating BSS

The main idea of applying BSS to the EEG signals for seizure prediction is to consider the seizure signals as independent components of the scalp EEG, which can be extracted using BSS algorithms. Then the traditional nonlinear analysis method, i.e. quantification of the dynamical changes by calculating the STLmax, is performed for the estimated sources to evaluate the predicability of the seizures. SOBI was applied for seizure source separation in Corsini's method [42]. SOBI separates the signals based on the assumption of mutual uncorrelatedness within multiple lags, rather than independence, which is reasonable for brain signal separation because the distribution of brain sources is unknown. In the work, two more algorithms, JADE and CTICA are applied for seizure source separation.

4.3.1 JADE Algorithm

The JADE algorithm [17] is based on higher-order statistics. As diagonalization of the correlation matrix gives the uncorrelated random variables, making the "off-diagonal" elements of the fourth order cumulant matrix of the output equal to zero would give an estimation of the independent components. Recall that the fourth-order cumulant for a real signal is defined as:

$$\begin{aligned} cum(x_i, x_j, x_k, x_l) = {} & E\{x_i x_j x_k x_l\} - E\{x_i x_j\}E\{x_k x_l\} - E\{x_i x_k\}E\{x_j x_l\} \\ & - E\{x_i x_l\}E\{x_j x_k\} \end{aligned} \tag{4.3.1}$$

where $cum(\cdot)$ denotes the cumulant. The cumulant tensor can be considered as the linear transformation of a matrix $\mathbf{M}$, which is given by:

$$[\mathbf{Q}_x(\mathbf{M})]_{ij} = \sum_{k,l=1}^{n} cum(x_i, x_j, x_k, x_l) m_{lk} \tag{4.3.2}$$

where m_{lk} is the *(l,k)*th component of matrix $\mathbf{M}$. Therefore, an eigenvalue decomposition (EVD) of the tensor satisfies,

$$\mathbf{Q}(\mathbf{M}) = \lambda \mathbf{M} \tag{4.3.3}$$

where λ is the eigenvalue and $\mathbf{M}$ is the eigenmatrix. In this model, the data are whitened by a "whitening matrix" $\mathbf{V}$,

$$\mathbf{z} = \mathbf{VAs} = \mathbf{W}^T\mathbf{s} \tag{4.3.4}$$

where matrix $\mathbf{W}$ is orthogonal. The eigenmatrix is given [65] as,

$$\mathbf{M} = \mathbf{w}_i \mathbf{w}_i^T \tag{4.3.5}$$

The JADE algorithm estimates the matrix $\mathbf{W}$ by diagonalization of matrix $\mathbf{WQ(M)W}^T$. It is noticed that minimization of the sum of squares of off-diagonal elements is equivalent to maximization of the sum of squares of diagonal elements. Thus, the solution of $\mathbf{W}$ that jointly diagonalizes the matrices can be obtained by the cost function [65]:

$$J_{JADE} = \sum_i \|diag(\mathbf{WQ}(\mathbf{M}_i)\mathbf{W}^T)\|_F^2 \tag{4.3.6}$$

where $\|diag(\cdot)\|^2$ means the sum of squares of the diagonal elements, $\|\cdot\|_F$ denotes Frobenius norm. Maximization of J_{JADE} is achieved by joint approximate diagonalization of $\mathbf{Q}(\mathbf{M})$.

4.3.2 Solution to Permutation Problem

For the investigation of seizure predictability, the dynamical measurement needs to be carried out for long-term and continuous EEG recordings. By considering the stationarity and the data length for calculating STLmax, the long recording EEG data need to be segmented into frames of a certain duration (10 seconds in this study). The algorithm is then performed over the consecutive data segments. There are two ambiguities in BSS, first, the scale of the independent components is uncertain; second, the order in which the components are arranged is unknown. The scaling problem can be solved by pre-whitening the data such that the data and the estimated sources can have unit variance. The sign of the estimated source does not affect the results of estimation of STLmax since the dynamical property is independent of the sign change. The permutation problem needs to be solved to maintain continuity of the sources because the estimated sources may appear in different orders along the consecutive segments. In order to solve this problem in the present work, the algorithm is performed over overlapped frames and the sources within the overlapped segments are compared by measuring the correlation between the estimated sources, and based on this the separated sources are realigned.

For n-channel zero-mean scalp EEG, $\mathbf{x}(t) = [x_1(t), x_2(t), ..., x_n(t)]^T$ of length L, consider two consecutive windows of data $\mathbf{x}_1(t) = \mathbf{x}(t_0 + t)$ and $\mathbf{x}_2(t) = \mathbf{x}(t_0 + N + t)$, where $N \ll L$, and $L - N$ is the length of the

overlapping window. If the outputs of BSS for segments $\mathbf{x}_1(t)$ and $\mathbf{x}_2(t)$ are $\mathbf{s}_1(t)$ and $\mathbf{s}_2(t)$ respectively, with $\mathbf{s}_1(t) = [s_1(t), s_2(t), ..., s_m(t)]^T$ and $\mathbf{s}_2(t) = [s'_1(t), s'_2(t), ..., s'_m(t)]^T$, then the correlation as the normalized covariance between $\mathbf{s}_1(t)$ and $\mathbf{s}_2(t)$ within the overlapping sections is measured as:

$$cor(\mathbf{s}_1, \mathbf{s}_2) = \frac{cov(\mathbf{s}_1, \mathbf{s}_2)}{\sigma_{\mathbf{s}_1}\sigma_{\mathbf{s}_2}} \tag{4.3.7}$$

where $\sigma_{\mathbf{s}}$ denotes the standard deviation and $cov(\mathbf{s}_1, \mathbf{s}_2)$ is the lag zero covariance of the two sources. The covariance provides a measure of the extent of correlation between these sources. Thus, the correlation is used to compare the consecutive blocks within the overlapped interval, whereby the estimated sources can be aligned accordingly.

In the case of applying CTICA, one reference signal can be obtained based on prior information about the seizure (as described in Chapter 3), because the location of the epileptogenic zone and the dominant frequency of the seizure may be known in advance. For each segment, the source which is closest to the reference signal can be selected from CTICA. Then, the STLmax can be calculated for the selected source. Therefore, the overlapped window is not necessary any longer, and the computational cost can be greatly decreased.

4.4 Experiments

There are two experiments in this section. In the first experiment, JADE and SOBI were applied to scalp EEG data of three epileptic patients, in which the scalp EEGs were recorded simultaneously with the intracranial signals. Correlation and overlap window was used to

solve the permutation problem. The results of STLmax obtained from the simultaneous intracranial and estimated sources were compared. In the second experiment, CTICA was tested for the same data. The reference signal was constructed based on the spatial and frequency information about the seizure (as described in Chapter 3). The source with the highest correlation coefficient with the reference was selected for further nonlinear analysis. The source obtained in this way is the source closest to the reference, which contains the most information from the seizure area.

4.4.1 Data Acquisition and Preprocessing

A set of 12-channel intracranial EEG recordings were acquired from multi-contact Formen Ovale (FO) electrodes. Electrode bundles were introduced bilaterally through the FO under fluoroscopic guidance. The deepest electrodes within each bundle lie next to medial temporal structures, whereas the most superficial electrodes lie at or just below the FO [42]. Simultaneously, the multichannel EEGs were recorded using standard silver cup electrodes applied according to the "Maudsley" electrode placement system, which is a modification of the extended 10-20 system. This system provides a more extensive coverage of the lower part of the cerebral convexity, increasing the sensitivity for the recording from basal subtemporal structures [77]. The 16 channels scalp EEG were sampled at 200 Hz and bandpass filtered in the frequency range of 0.3 Hz - 70 Hz. The system input range was 2 mV and the data were digitized with a 12-bit analog-to-digital converter [42].

The signals were preprocessed by first removing the baseline to alleviate the effect of low frequency artifacts. Then, the EEGs were

filtered by a $10th$ order Butterworth lowpass digital filter with an edge frequency of 45 Hz in order to eliminate the 50 Hz frequency component. The EEGs used in the following experiments were truncated from the original long recordings. The length of the data segment was 5-6 minutes with the seizure onset at the end of the data segment. (The data used in the experiments were known to have the seizure at the end of the data segment though the exact time of seizure was unknown, but one can expect the STLmax to show a downward trend at the end of the segment.) In all experiments, the mean of data was removed. The preliminary whitening was performed to make the data have unit variance before further separation processing. The number of sources was chosen as 16.

4.4.2 Experiment I

Intracranial and Scalp EEGs

Fig. 4.1 shows four channel intracranial EEG recordings with duration of 10 seconds. The first two channels are close to the epileptic area, from which it can be seen that the seizure starts from the middle of the data segment. The other two channels do not show the obvious dynamic transition compared with the first two channels, mainly because the electrodes were not implanted in proximity of any seizure sources. Fig. 4.2 displays the scalp EEG recordings of the same segment. Compared with Fig. 4.1, it is not easy to distinguish the seizure signal due to the noise and artifacts.

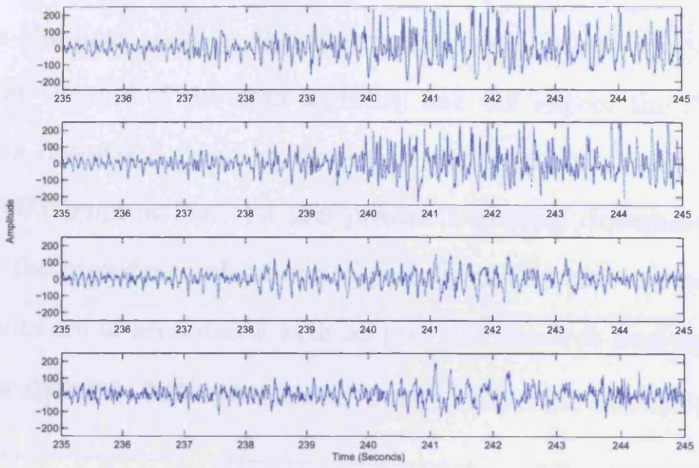

Figure 4.1. Intracranial EEG recordings from patient 1.

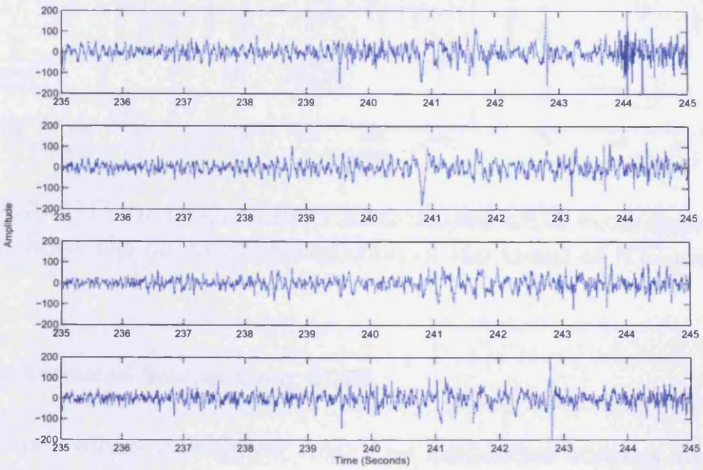

Figure 4.2. Scalp EEG recordings from patient 1.

STLmax of Intracranial EEG

The data from three patients were tested and the corresponding STLmax calculation results are shown in Fig. 4.3. It can be seen that STLmax values are positive, which indicates that the system is chaotic. Because the data used in the experiments were known to have the seizure at the end of the data segment, one can expect the STLmax to show a downward trend at the end of the segment. It can be seen that the STLmax in Fig. 4.3 also present a gradual downward trend prior to the occurrence of seizure, especially in the last two patients. The results are in accordance with all previous research findings using nonlinear dynamic methods.

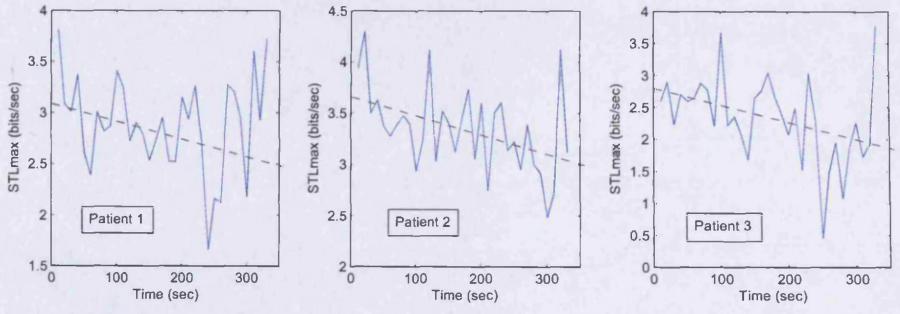

Figure 4.3. STLmax values from intracranial EEG recordings. The dash line shows the linear approximation of the trend of STLmax.

STLmax of Estimated Sources Using SOBI

The STLmax values calculated from the estimated sources by using SOBI are given in Fig. 4.4. For patient 1, there is one source with a minimum value of STLmax of around 250 sec, and another around 150 sec. For patient 2, STLmax of source 2 and source 4 gradually drop before the seizure onset. For patient 3, only source 1 presents a very clear downward trend prior to the seizure.

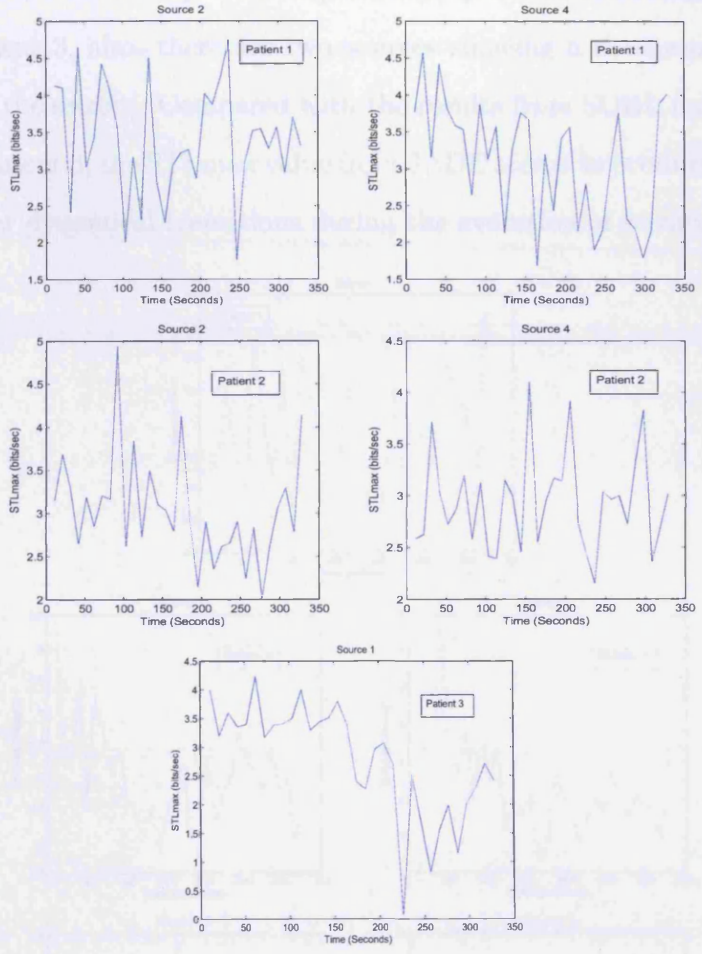

Figure 4.4. STLmax values of estimated sources by using SOBI.

STLmax of the Estimated Sources Using JADE

The STLmax values calculated from the estimated sources by using JADE are given in Fig. 4.5. For patient 1, source 1 shows the minimum STLmax near the end of the segment. For patient 2, it is seen that source 1 and source 2 present a gradual drop before the seizure onset. For patient 3, also, there are two sources showing a downward trend prior to the seizure. Compared with the results from SOBI, for patient 2 and patient 3, the STLmax value from JADE seems to produce clearer nonlinear dynamical transitions during the evolution of seizure.

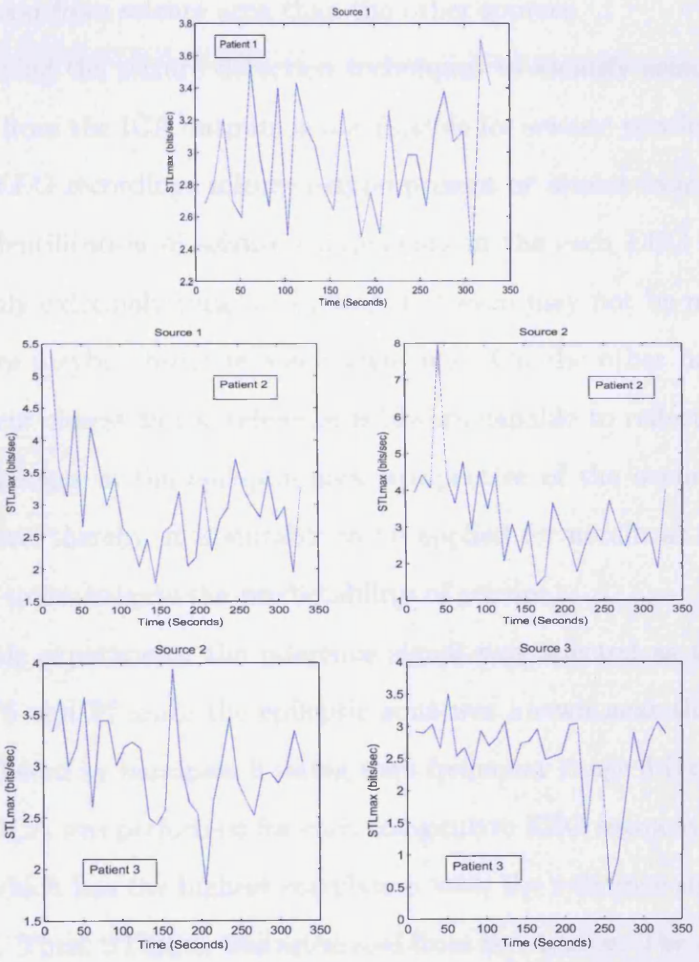

Figure 4.5. STLmax values of the estimated sources by using JADE.

4.4.3 Experiment II

In the second experiment, CTICA was applied to the same scalp EEG data. A component which had the highest correlation with the reference signal was selected for the further nonlinear analysis. The component selected by this way is the source closest to the reference signal. As explained in Chapter 3, the reference signal in CTICA was formed by averaging and filtering the signals from the epileptic area, since the epileptic area and the frequency band with seizure were usually known a priori. Therefore, the source closest to the reference will contain more information from seizure area than the other sources.

Applying the seizure detection techniques to identify seizure components from the ICA outputs is not feasible for seizure prediction , as in long EEG recordings seizure maybe present or absent from time to time. Identification of seizure components in the each EEG segment is not only extremely time consuming, but even may not be necessary as seizure maybe absent in some segments. On the other hand, the component closest to the reference is always capable to reflect the dynamic changes in the epileptic area irrespective of the occurrence of the seizure, thereby, it is suitable to be applied for nonlinear dynamic analysis to investigate the predictability of seizure.

In this experiment, the reference signal was selected as the average of F8 and F7 since the epileptic zone was known near the frontal area, followed by bandpass fi tering with frequency range 3 Hz - 15 Hz. The CTICA was performed for each consecutive EEG segment and one source which has the highest correlation with the reference signal was selected. Then, STLmax was estimated from this source. The main advantage of applying CTICA is that STLmax can be calculated for one

source only and no overlapping window is needed, therefore the computational cost is much less and this approach is more efficient than that in the first experiment.

Fig. 4.6 gives the results of STLmax obtained from same patients as the above experiment. It is noticed that, in all cases, a gradual drop is observed prior to seizure, in accordance with the results from the intracranial EEGs (as in Fig. 4.3).

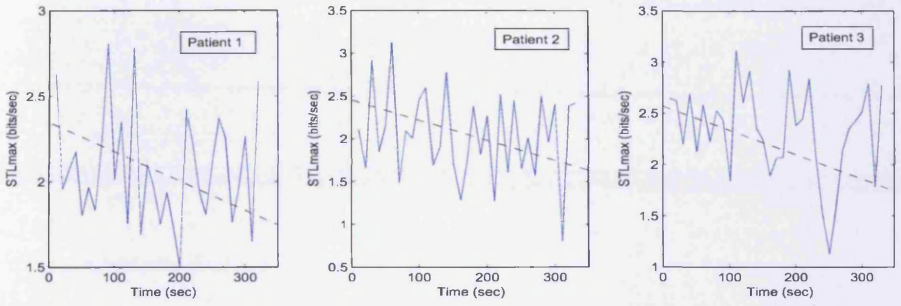

Figure 4.6. STLmax values of the seizure source obtained from CTICA. The dash line shows the linear approximation of the trend of STLmax.

4.5 Conclusion

Predictability of epileptic seizure has been investigated in this chapter. By using BSS techniques, the seizure components can be extracted from the scalp EEG background. The results of nonlinear quantification present a similar downward trend as for the intracranial recordings, which suggests predictability of seizure from scalp EEG. By incorporating the prior spatial and spectral information about the seizure as the constraint, the CTICA algorithm proves to be an effective and superior method for seizure source separation, which not only can extract the seizure source, but also is less computationally expensive than the

other popular separation methods.

Chapter 5

FUSION OF EEG AND FMRI: SCANNER ARTIFACT REMOVAL

5.1 Introduction

Simultaneous EEG and fMRI recording combines two advanced modalities to monitor the micro neural functions by exploiting both temporal and spatial information. Clinically, EEG remains as the principal tool for the diagnosis and classification of brain function disorder syndromes such as schizophrenia and epileptic seizures. This is because EEG presents the micro neural activities with high temporal resolution. On the other hand, fMRI, with high spatial resolution, compensates for the low spatial resolution drawback of EEG. Therefore, fusion of these two modalities can exploit more efficiently the spatio-temporal information related to the brain activity.

Combined EEG and fMRI recording plays a very important role for diagnosis of epilepsy and identification of the epileptogenic zone. Focal epilepsy is characterized by its onset within a distinct area. Therefore, it can be treated by surgical operation to remove the epileptic

cells from the brain, if the epileptogenic zone can be identified accurately [96]. The signature of blood oxygen level-dependence (BOLD), potentially available from fMRI, provides very valuable spatial information for identification of the epileptogenic zone and the final surgical decision.

The technical problems in collection of simultaneous EEG-fMRI recordings include the mutual effects in both EEG and fMRI data. The study in this chapter was only focused on the interferences caused by the fMRI scanner in the EEG recordings. There are different types of artifacts which contaminate the EEGs. One common type is caused by the body movement in a magnetic field. This type of artifact can be reduced by mechanical means such as fixing the subject and wires, and avoiding loops in the wires. Another type of artifact is cardiac pulse interference, which can cause a small movement of electrodes and scalp due to the expansion and contraction of scalp arteries. The pulse artifacts can be reduced by using some post-processing methods, such as the ECG-triggered subtraction of an averaged artifact at each EEG channel [78]. The most significant interference is the MRI scanner artifacts which originate from switching magnetic field gradients during the process of MRI scanning. Fig. 5.1 shows the EEG signals which contain such scanner artifacts. It can be seen that the scanner artifacts intensively obscure the EEG signals, which makes it impossible to extract the diagnostic information from EEG.

Various methods for scanner artifact removal have been investigated previously, such as processing in the frequency domain [79] [80], introducing certain recording methods [81], and post-processing approaches [82]. In [79] and [80], the focus is on elimination of the artifact-

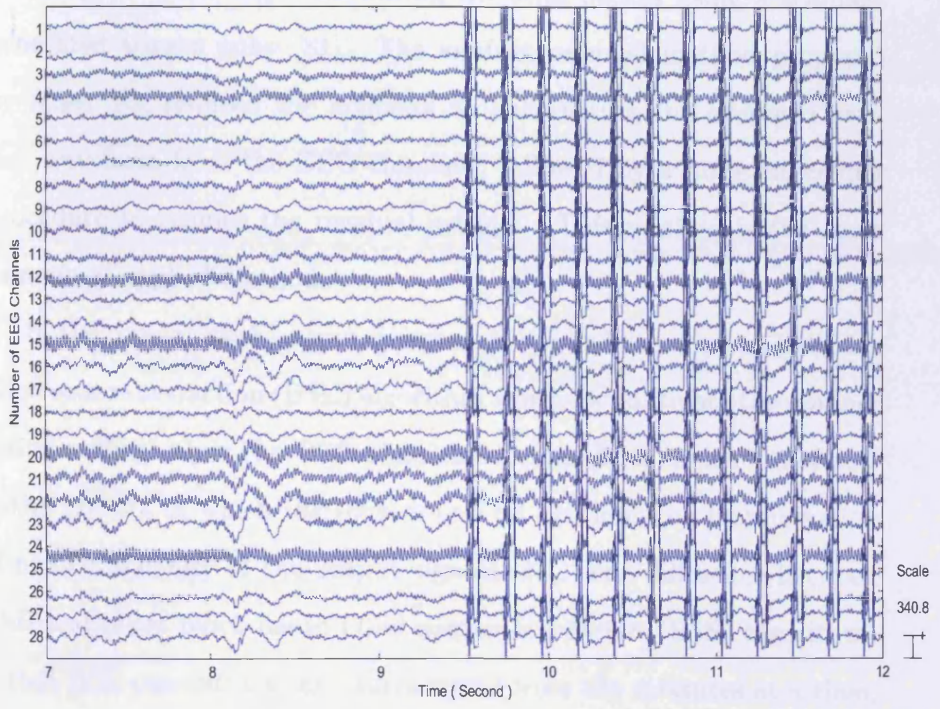

Figure 5.1. EEGs containing scanner artifacts in which the real EEGs are obscured by the scanner artifacts.

specific power spectrum by utilizing the fast Fourier transform (FFT) and reconstructing the artifact-free signal by inverse FFT. The spectrum of the scanner artifact was detected by comparing the EEG spectrum before and during the MR imaging sequence. Some approaches have been attempted to improve the recording methods to minimize the scanner effect, such as carefully choosing the image sequence and blanking the EEG segments during the scan period using a scanner-generated trigger pulse [81]. The artifact removal method proposed by Allen [82] reduced the artifacts by subtracting the averaged artifact waveform from the EEG channels, followed by a noise cancelling procedure to remove the residual artifact. This method is the most commonly applied method.

In the present work, a new approach is applied based on an iterative blind source extraction (BSE) algorithm which can mitigate the scanner artifact effectively. The BSE algorithm is based on higher order statistics (HOS), in which the sources can be extracted by maximization of non-Gaussianity of the output signals [83]. The difference between BSE and other block-based blind source separation (BSS) algorithms is that BSE can extract one source signal from the mixtures at a time, rather than separating all the sources at the same time. If more than one source is expected, then BSE can extract the sources one-by-one. The process of deflation following the extraction in each iteration can exclude the extracted source from the rest of the mixture. In this work, the scanner artifacts are the sources to be extracted from the EEGs. After performing a number of extractions and deflations, the scanner artifacts can be reduced effectively.

In the following sections, the physical background of MRI signals

is briefly introduced. The BSE algorithm is then explained in detail. The experiments are carried out on both simulated data and real EEG data with fMRI scanner artifacts. The results are presented at the end of this chapter.

5.2 MRI Signal and Scanner Artifact

Nuclear Magnetic Resonance

Magnetic resonance imaging (MRI) is an imaging technique which can provide high quality images from inside the human body. The principle of MRI is based on nuclear magnetic resonance (NMR), a property of atoms first observed by Bloch and Purcell [84]. Most MRI looks at the NMR signal from the hydrogen nucleus. The hydrogen nucleus contains one single proton, which possesses an intrinsic property called spin. In physics and chemistry, spin is the angular momentum intrinsic to a body, and elementary particles such as protons, electrons and neutrons possess spin. The spin of the particle can be considered as a magnetic moment vector which makes the particle behave like a magnet. When the proton is placed in an external magnetic field, the spin vector of the particle aligns itself with the external field. Then the proton may experience the energy transition between two states: a proton in the lower energy state absorbs a photon and ends up in the upper energy state; a proton which emits a photon can transfer from a higher to a lower energy state. It is this energy transition that generates the NMR signal, and this transition between the lower and higher energy states is called resonance [84].

If a particle with spin is placed in a magnetic field of strength $\mathbf{B}$, it absorbs a photon of frequency ν, which is referred to as the reso-

nance frequency, and the relation between the magnetic field and the resonance frequency is given as,

$$\nu = \gamma \mathbf{B} \tag{5.2.1}$$

where γ is the gyromagnetic ratio of the particle. The transition of energy, $\mathbf{E}$, happens when the particle absorbs a photon and changes from the lower energy state to the higher energy state. This energy is related to the frequency, ν, by Planck's constant h, i.e. [84].

$$\mathbf{E} = h\nu \tag{5.2.2}$$

Therefore, the energy needed for a transition between the two states is

$$\mathbf{E} = h\gamma \mathbf{B} \tag{5.2.3}$$

Hence, the NMR signal originates from this energy transition procedure and the energy is proportional to the strength of the magnetic field.

Scanner Artifact

A magnetic resonance image is the picture that presents the NMR signals in the object. In order to form an image, the NMR signals must be linked to the spatial region. The procedure to find the relationship between the resonance frequency and position is referred to as frequency encoding.

From the resonance equation $\nu = \gamma \mathbf{B}$, one can see that the resonance frequency of the spin is proportional to the magnetic field strength $\mathbf{B}$. In MRI, in order to link the frequency to the spatial region, a magnetic field gradient is applied. A magnetic field gradient is a variation in the

magnetic field with respect to position. For example, a one-dimensional magnetic field gradient varies along the x axis direction. Suppose that, at the centre of the magnetic field, the magnetic strength is $\mathbf{B}_0$, the resonance frequency is ν_0, and the gradient along the x axis is $\mathbf{G}_x$, then the relationship between the resonance frequency ν and position x can be written as,

$$\nu = \gamma(\mathbf{B}_0 + x\mathbf{G}_x) = \nu_0 + \gamma x \mathbf{G}_x \tag{5.2.4}$$

then

$$x = (\nu - \nu_0)/(\gamma \mathbf{G}_x) \tag{5.2.5}$$

This equation forms the basic principle of magnetic resonance imaging.

During the process of MRI scanning, the object is placed in a magnetic field, a one-dimensional magnetic field is applied at one certain angle in one desired plane and the NMR signals are recorded. Then this magnetic field is applied to the next angle and the same process is repeated until the whole object is scanned. The scanner artifacts originate from switching magnetic field gradients during the process of MRI scanning. (The more information about fMRI methods can be found in [85]).

5.3 Scanner Artifact Removal by Blind Source Extraction

One of the solutions for removal of scanner artifacts, proposed by Allen et al. [82], is based on subtraction of the averaged artifact from each EEG channel. In this method, the scanner artifact waveform was obtained by averaging 25 epochs of EEGs. The scanner-generated "slice trigger pulse" was used to ensure that the artifacts from one epoch to another are synchronised. Then, the averaged artifact was subtracted

from EEGs for each epoch. Theoretically, since the scanning process is periodic, the averaging-and-subtraction can remove this kind of artifact. In general, this method provides a significant improvement in the EEG quality. However, some useful information in EEGs maybe lost by the averaging method, and the "slice trigger pulse" requires a very delicate connection between the scanner and the EEG recording system. In the present work, a blind source extraction technique is proposed which does not need any synchronization process as the "slice trigger pulse", but can reduce the scanner artifact effectively.

Blind Source Extraction Algorithm

The BSE algorithm is based on the maximization of non-Gaussianity of the output signals. Spike-type scanner artifacts always have higher kurtosis than normal EEGs, and therefore BSE is a suitable choice to extract these high kurtosis artifacts.

Given n-channel observed data $\mathbf{x}(t) = [x_1(t), x_2(t), ..., x_n(t)]^T$, $t = 1, ..., N$, as a linear and instantaneous mixture of m underlying sources $\mathbf{s}(t) = [s_1(t), s_2(t), ..., s_m(t)]^T$, which are mixed by the mixing system $\mathbf{A}$ as,

$$\mathbf{x}(t) = \mathbf{A}\mathbf{s}(t) \tag{5.3.1}$$

then the estimated source $\mathbf{y}$ is obtained by using

$$\mathbf{y} = \mathbf{w}^T\mathbf{X} \tag{5.3.2}$$

where $\mathbf{X} = [\mathbf{x}(1), ..., \mathbf{x}(N)]$, and $\mathbf{w}$ is the unmixing vector which is estimated based on the maximization of non-Gaussianity of the output signal $\mathbf{y}$. The cost function of BSE is then expressed [83] as:

$$J(\mathbf{w}) = -\frac{1}{4}|k_4(y)| = -\frac{\beta}{4}k_4(y) \tag{5.3.3}$$

where $k_4(y)$ is the normalized kurtosis, which measures the flatness (for the sub-Gaussian signal) or peakedness (for the super-Gaussian signal) of a distribution of a signal. The parameter β determines the sign of the kurtosis of the extracted signal, and is selected to be -1 or $+1$ when the extracted source has negative or positive kurtosis respectively. The normalized kurtosis for zero-mean signals is defined by,

$$k_4(y) = \frac{E\{|y|^4\}}{E^2\{|y|^2\}} - 3 \tag{5.3.4}$$

where $E\{\}$ is the statistical expectation operator. Applying the standard gradient descent approach [83] to minimize the cost function (5.3.3) one can obtain:

$$\triangle\mathbf{w} = -\mu(t)\frac{\partial J(\mathbf{w})}{\partial \mathbf{w}} = \mu(t)\varphi(y(t))\mathbf{x}(t) \tag{5.3.5}$$

where $\mu(t) > 0$ is a learning rate, and

$$\varphi(y) = \beta\frac{\hat{m}_4(y)}{\hat{m}_2^3}[\frac{\hat{m}_2(y)}{\hat{m}_4(y)}y^3 - y] \tag{5.3.6}$$

where the moments are given by $m_q(y) = E\{y^q(t)\}$. $\mathbf{w}$ can be obtained by applying the simple local type least mean square (LMS) learning rule:

$$\mathbf{w}(k+1) = \mathbf{w}(k) + \mu(k)\varphi(y(k))\mathbf{x}(k) \tag{5.3.7}$$

where k is the iteration number. Since BSE extracts the sources one-

by-one, in order to avoid the previous source to be separated again, a deflation process follows the extraction process. Assuming that $\mathbf{x}_j$ and y_j are the jth mixture and jth extracted components respectively, the deflation process finds a new mixture $\mathbf{x}_{j+1}$ iteratively based on the following update equation,

$$\mathbf{x}_{j+1}(k) = \mathbf{x}_j(k) - \tilde{\mathbf{w}}_j y_j(k) \tag{5.3.8}$$

where $y_j(k) = \mathbf{w}_j^T \mathbf{x}_j(k)$, and $\tilde{\mathbf{w}}_j$ is estimated by minimization of the following cost (energy) function [83]:

$$J(\tilde{\mathbf{w}}_j) = \frac{1}{2} E\{\sum_{p=1}^{n} \mathbf{x}_{j+1,p}^2\} \tag{5.3.9}$$

The above cost function can be considered as an energy function, the minimum of which is achieved when the extracted source is eliminated from the mixtures of sources. By minimization of the mean square cost function

$$J(\tilde{\mathbf{w}}_j) = E\{\mathbf{x}_{j+1}^T \mathbf{x}_{j+1}\} = E\{\mathbf{x}_j^T \mathbf{x}_j\} - 2\tilde{\mathbf{w}}_j E\{\mathbf{x}_j y_j\} + \tilde{\mathbf{w}}_j^T \tilde{\mathbf{w}}_j E\{y_j^2\} \tag{5.3.10}$$

with respect to $\tilde{\mathbf{w}}_j$, one can get an alternative simple updating equation [83]:

$$\tilde{\mathbf{w}}_j = \frac{E\{\mathbf{x}_j y_j\}}{E\{y_j^2\}} = \frac{E\{\mathbf{x}_j^T \mathbf{x}_j\}\mathbf{w}_j}{E\{y_j^2\}} \tag{5.3.11}$$

Implementation

As BSE is based on maximization of the output kurtosis, each time running BSE will produce one source that has higher kurtosis. In this case, the estimated source is the scanner artifact. The extraction process

first extracts the artifact as one source, a deflation process removes this source from the EEG mixtures, and then the BSE algorithm is performed on the remaining EEGs.

In order to remove the whole scanner artifacts, it is necessary to run the BSE a number of times. The number of times is decided by measuring the kurtosis of the mixtures iteratively during the BSE process. Theoretically, once the scanner artifacts are removed from the EEG, the kurtosis of the scanner artifact-removed EEG would be decreased. Thereby, kurtosis measurement is selected as the criterion to decide the number of iterations for running the overall BSE, and is carried out by comparing the measured normalized kurtosis with an empirically predefined threshold value. Care has to be taken in order to avoid removal of any informative sources. For this case, this threshold value is set to 1. Thus the BSE algorithm stops once the normalized kurtosis decreases to less than 1.

5.4 Experiments

5.4.1 Experiment I: Simulation

Three source signals were generated with kurtosis of 1.5, 3.0 and 4.15 respectively. The simulated source signals are shown in Fig. 5.2. The mixed sources are shown in Fig. 5.3, which were mixed by a matrix with elements drawn from a zero mean and unit variance Gaussian distribution. The result after BSE is given in Fig. 5.4. It is seen that the mixed source signals have been extracted, note the expected change of amplitudes and order of sources.

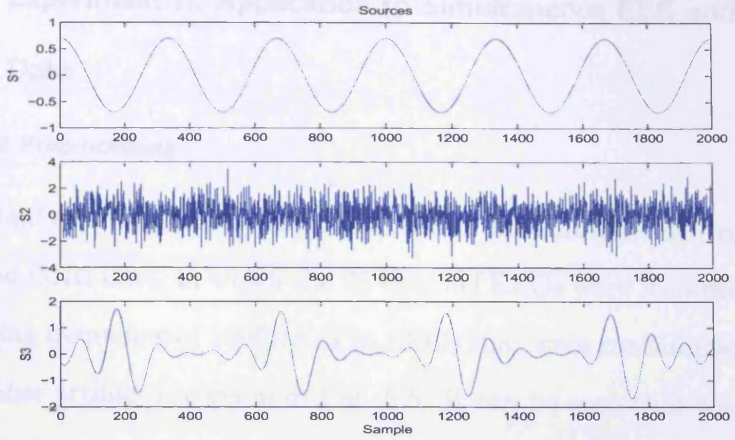

Figure 5.2. Synthetic source signals.

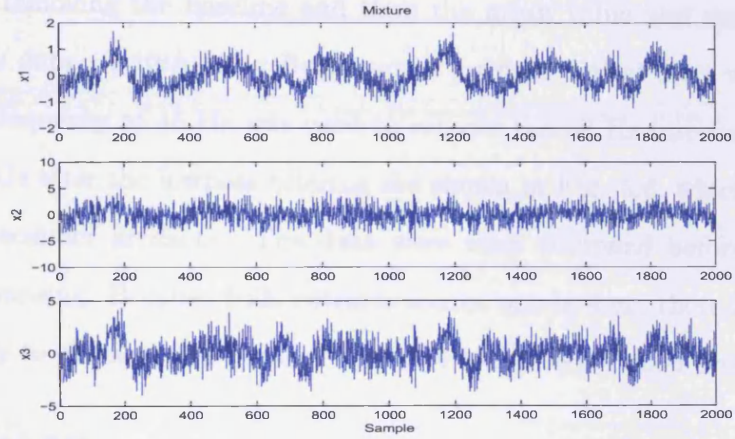

Figure 5.3. The mixtures of the sources which are mixed by a randomly chosen mixing matrix.

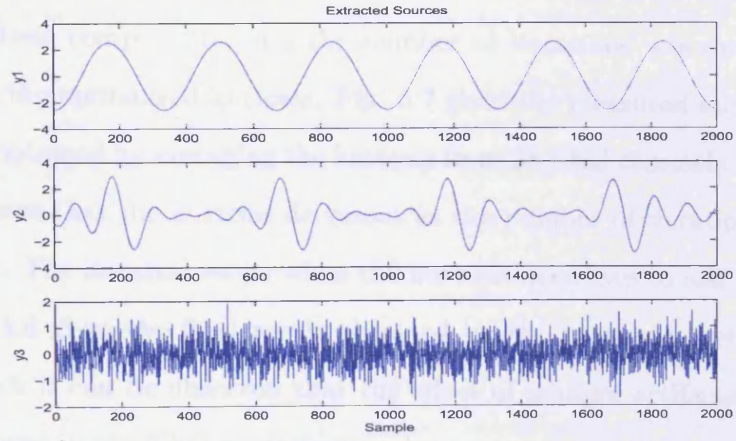

Figure 5.4. The extracted sources obtained by the BSE algorithm.

5.4.2 Experiment II: Application to Simultaneous EEG and fMRI Data

Data and Preprocessing

The second experiment was carried out based on simultaneously recorded EEG and fMRI data, in which the 28-channel EEGs were recorded with a sampling frequency of 1000Hz. The EEGs that were contaminated by the scanner artifact are given in Fig. 5.5. It can be seen that the scanner artifacts obscure the real EEG signals. The data were preprocessed by first removing the baseline and then the mean value was removed from the data. A $10th$ order Butterworth lowpass digital filter with a cut-off frequency of 45 Hz was used to remove the 50 Hz interference. The EEGs after the lowpass filtering are shown in Fig. 5.6, which still contain scanner artifacts. The data were then whitened before further processing. Because BSE extracts source one-by-one, there is not necessary to estimate the number of source before separation process.

Results from BSE

The BSE algorithm was applied to the filtered EEGs to remove the high kurtosis components, and the number of iterations was decided based on the normalized kurtosis. Fig. 5.7 gives the measured kurtosis which is obtained by averaging the kurtosis from 28 EEG channels. The graph shows that the kurtosis decreases as the number of iterations is increased. The iteration stops when the kurtosis decreases to less than 1. Fig. 5.8 gives the final result obtained by the proposed method, from which it can be observed that the effect of scanner artifacts has been reduced in the EEG recordings.

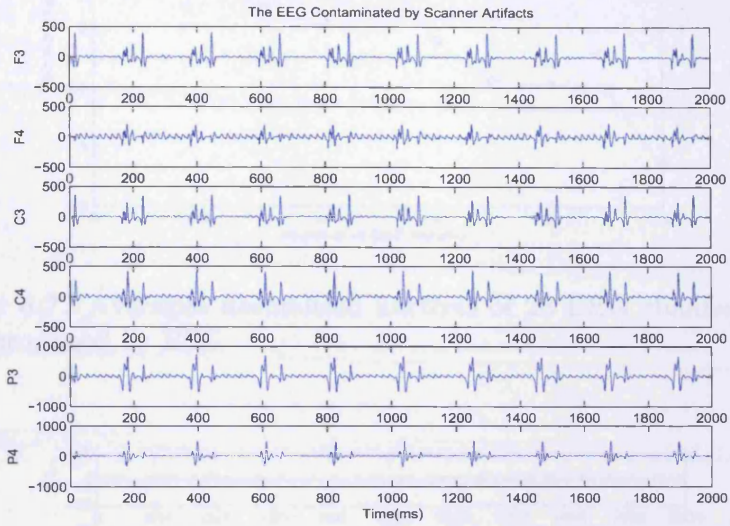

Figure 5.5. The EEGs containing the scanner artifacts in which the real EEGs are obscured by scanner artifacts.

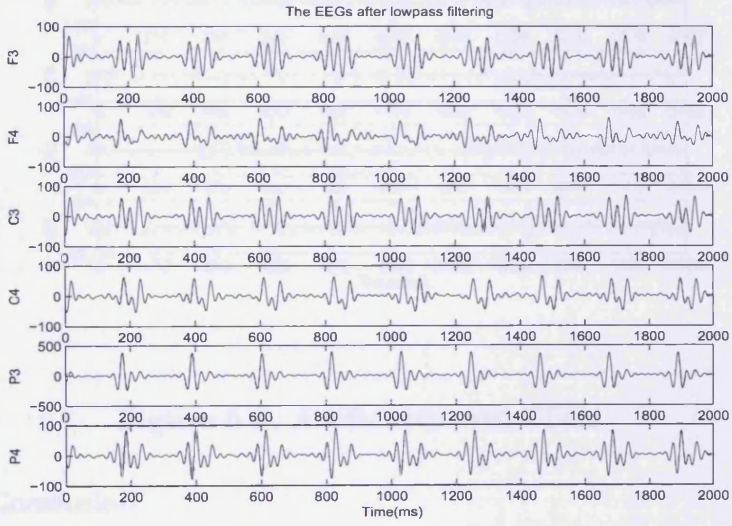

Figure 5.6. The EEGs with scanner artifacts after lowpass filtering.

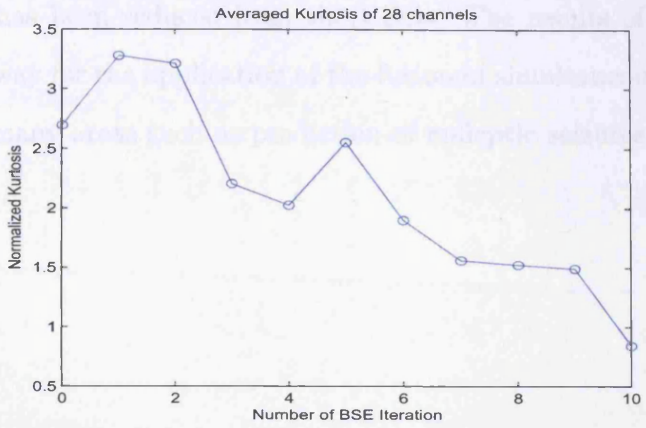

Figure 5.7. Averaged normalized kurtosis of 28 EEG channels after being processed by BSE.

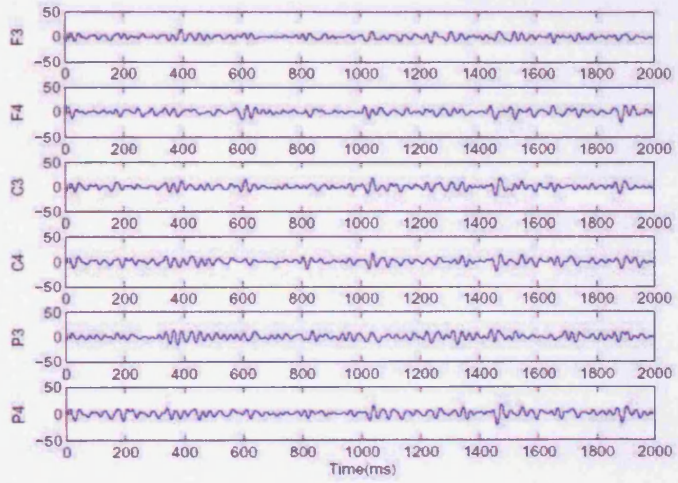

Figure 5.8. Artifact-removed EEGs.

5.5 Conclusion

In this chapter, an effective method for removing the scanner artifacts has been presented, in which BSE was applied to extract the high kurtosis scanner artifacts. The results show that the effect of scanner

artifacts has been reduced from the EEGs. The results of this study pave the way for the application of the fusion of simultaneous EEG and fMRI in many areas such as prediction of epileptic seizures from scalp EEGs.

Chapter 6

ANALYSIS OF EPILEPTIC EEG-FMRI SIGNALS

6.1 Introduction

Relationship between fMRI and EEG

As one of the advanced brain function monitoring modalities, fMRI provides high resolution spatial information which helps visualization of the brain activities. Blood-oxygenated level-dependence (BOLD) regions in fMRI result from event-related, movement-related, and abnormal brain activities such as seizures, which provides valuable information for localization of the brain activation regions. EEG, on the other hand, reveals the neural electrical activation and provides the high temporal resolution. Many unanswered questions about the relationship between the cerebral haemodynamic changes (measured by fMRI) and the underlying neural electrical activity (revealed by EEG) are of interest to many researchers.

Although the spatiotemporal relationship between fMRI and EEG is still far from straightforward, there are promising perspectives presented in the literature. Logothetis et al. [101] compared local field potentials (LFPs) with the fMRI responses from the visual cortex of

monkeys. The largest magnitude changes observed in LFPs at recording sites characterized by transient responses were the signals that highly correlated with the haemodynamic response. In [102], the relationship between fMRI and event-related potential (ERP) was examined during an auditory oddball paradigm. Horovitz et al. [102] have shown for the first time that for auditory stimuli, the amplitude of the hemodynamic response in the region of interest (ROI) follows the amplitude of the ERP changes. BOLD signals from the source location of P300 have high correlation with the amplitude of the P300. In a more recent simultaneous EEG-fMRI study of painful electric stimulation [90], Christman et al. have shown that the BOLD changes in ROI were correlated with the dipole strength of the EEG source and revealed a close relationship of BOLD signal and possible underlying neural electrical activity in ROI. Although these studies were based upon clinical and physiological experiments, the results provided evidence that there were underlying connections between fMRI and EEG. How to combine the signals from these two modalities technically has started to attract more attention in recent years.

Fusion of fMRI and EEG

Multimodal data fusion has raised much attention in the last few years and numerous efforts have been directed towards combining high spatial information provided by hemadynamic based imaging methods, such as fMRI, with the high quality temporal data generated by EEG or MEG. These approaches mainly focus on three aspects [91]. The first aspect is referred to as direct data fusion, such as the most common method used in EEG source localization. The geometrical information on the source

activation region obtained from fMRI can be used as the constraint for localizing the EEG dipole sources [87] - [90], because there is no unique solution for the ill-posed inverse problem for EEG source localization in the absence of constraints. For example, in [89] the geometrical information from fMRI provided the realistic head model as a volume conductor medium to help reduce the EEG localisation solution space. In [87], fMRI was not used as a rigid constraint but helped in selecting more likely inverse solution among the possible solutions. The second aspect is based on the use of computational neural models, in which the relation of EEG and fMRI is modelled on the basis of some hypotheses of certain neural activities [92] [93]. In these approaches, the EEG and fMRI data are not linked directly, but are compared inside a simulated neural model. The main challenge for this approach is to construct a recurrent neural model for simulation of the complex neural physiological activities, which is still questionable from the physiological aspect because the simulated neural model simplifies the complexity of neural activities [91]. The third type of these fusion approaches is more commonly used in the clinical or neurological field in which temporal information from the EEG helps to time-lock the events in the fMRI. As the studies discussed in [94]- [98], the epileptic EEG and fMRI data were simultaneously recorded during seizure onset, and the spikes within the seizure EEG were modelled as the stimuli which can be used in the statistical parameter mapping in fMRI. The provided brain map of seizure can be used for help in surgical planning. In this study, the work is related to the third aspect, which aims at combining EEG and fMRI for identification of the "epileptogenic zone".

Model-based Method for fMRI Analysis

Several techniques have been proposed for detecting the brain activation regions in fMRI. The most commonly used model-based approach is the general linear model (GLM) [105]- [107] developed by Friston et al. (1995) [105]. According to GLM, fMRI data from each voxel is considered as a linear combination of the hemodynamic responses of stimuli and their corresponding weighted parameters. The stimuli are modelled as delta functions and the response is the convolution of the stimulus and the predefined hemodynamic response functions (HRF) [105]. The response is referred to as Design Matrix in GLM, and the HRF can be chosen from some well defined functions such as the Gamma function and Fourier set (windowed sines and cosines). Therefore, based on GLM, in order to specify the model, prior knowledge or specific assumptions about the time courses contributing to the signal changes are required. After the model specification, the weight parameters can be estimated by using estimation techniques such as maximum likelihood estimation (MLE) or Bayesian estimation. The active areas are then detected by evaluating the statistical significance of the whole brain voxels [105]. Several software toolboxes for fMRI analysis have been developed based on GLM, which can be used for fMRI data preprocessing, model specification, statistical parameter estimation and parameter mapping, such as statistical parametric mapping (SPM) [109] and FMRIB Software Library (FSL) [110]. Details of application of SPM are given in the following section.

Data-based Method for fMRI Analysis

In contrast to the model-based GLM, the data-based model relies on the data instead of prior information on stimuli or predefined brain function. One of these approaches has raised more attention recently [114]- [127]. This was proposed by McKeown et al. [114] as the first application of ICA to fMRI data analysis. In the ICA model, the fMRI data are considered as a linear combination of a number of temporally or spatially independent components. Comparing with GLM, the data-driven model is more suitable for analysis of brain signals because no assumptions regarding the stimulus response are required. The brain function and its hemadynamic response are so complicated that it is still questionable to simply choose certain predefined HRF and to assume that the shape of the HRF remains constant during the events for each brain voxel. In the following section, the details of the ICA model are discussed and the experimental results show that the ICA approach can be used to analyze the fMRI data in those cases that the GLM cannot work.

Apart from ICA, some other model-free approaches have been applied to fMRI analysis, such as support vector machine (SVM) [129] - [132], and mutual information (MI) [128]. The core concept of using SVM or any other pattern classification method is based on the fact that the voxels within the active areas certainly contain some special patterns which can distinguish the active part from the rest of the brain. These features can be image features such as image intensity, probability density, statistical information from each voxel, or the shape of the temporal sequence of the designed event. By means of feature extraction, the region of activation can be detected.

Information theory has also been applied to various research topics in neuroscience in the last decade. The main idea is to estimate the information across the whole brain voxels under the designed experiments and then to decide the active areas based on the mutual information criterion. As in [128], Galit et al. proposed a model-free method based on measuring the entropy and MI, which detected the location of the event-related activity by evaluation of the temporal information across different brain regions. The stimulus was used as a reference, the MI between the fMRI signals in each voxel and the stimulus was measured. The active areas were then detected by selecting those voxels which had higher MI according to the task conditions.

fMRI Analysis for Epileptic Seizure

In comparison with the common fMRI analysis, for which the functional data are acquired from the designed experiments, the fMRI data from epileptic seizures are very different. As the spontaneous brain activity caused by certain functional disorders, the response of epileptic seizure is very difficult to be modelled. There has been limited literature [94] - [96] [98] that investigated the statistical parameter mapping of epileptic seizure spikes. Those results were limited by carefully choosing functional data that have distinguishable periodic seizure spikes, in which the spikes were used as the stimulus to construct the design matrix. Therefore, these approaches cannot work for unpredictable events, such as seizure onset. However, the seizure active area can be detected without concerning the seizure time course by using a model-free method such as ICA. If the information available in EEG and fMRI can be incorporated in the separation process of ICA, then the performance of

ICA can be improved. This is the main objective of the present work.

This chapter is arranged as follows. First, the GLM is briefly explained. Second, the spatial ICA model is described in detail and also a comparison between the spatial and temporal ICA models is discussed, with the development of the constrained spatial ICA algorithm given afterwards. In the final section, the experimental results are given and discussed.

6.2 Model Based Methods

6.2.1 General Linear Model

The General Linear Model (GLM) is a linear model which can be presented as:

$$\mathbf{Y} = \mathbf{XB} + \mathbf{E} \tag{6.2.1}$$

where $\mathbf{Y}$ is an $N \times V$ matrix representing the fMRI time series in each voxel, N is the number of scans, and V is the number of voxels involved in the analysis. $\mathbf{X}$ is an $N \times F$ matrix referred to as the design matrix, which is the predicted event response by convolving the stimulus with the predefined hemadynamic response function, and F is the number of stimuli (events). $\mathbf{B}$ is an $F \times V$ matrix of unknown parameters which are to be estimated, and $\mathbf{E}$ represents the errors which are assumed to be independently and identically distributed normal random variables [105].

For the fMRI data from the jth voxel, the elements of the above matrix equation can be represented as:

$$\begin{pmatrix} y_{1j} \\ \vdots \\ y_{ij} \\ \vdots \\ y_{Nj} \end{pmatrix} = \begin{pmatrix} x_{11} & \cdots & x_{1j} & \cdots & x_{1F} \\ \vdots & \ddots & \vdots & \ddots & \vdots \\ x_{i1} & \cdots & x_{ij} & \cdots & x_{iF} \\ \vdots & \ddots & \vdots & \ddots & \vdots \\ x_{N1} & \cdots & x_{Nj} & \cdots & x_{NF} \end{pmatrix} \begin{pmatrix} b_{1j} \\ \vdots \\ b_{ij} \\ \vdots \\ b_{Fj} \end{pmatrix} + \begin{pmatrix} \epsilon_{1j} \\ \vdots \\ \epsilon_{ij} \\ \vdots \\ \epsilon_{Nj} \end{pmatrix} \quad (6.2.2)$$

From the above equation, one can see that the column vector $\mathbf{b}_j = [b_{1j}, ..., b_{Fj}]^T$ is actually the weight factor of each event response at the jth voxel. An estimation of the parameter $\mathbf{B}$ which represents the weight for all voxels, denoted as $\hat{\mathbf{B}}$, can be obtained as,

$$\hat{\mathbf{B}} = (\mathbf{X}^T\mathbf{X})^{-1}\mathbf{X}^T\mathbf{Y} \quad (6.2.3)$$

The conventional approach for fMRI analysis is based on evaluation of the statistical significance in each voxel, for example by means of the t-statistic [105]. The activated areas are detected by selecting the voxels in which the statistical significance is higher than a certain threshold value.

6.3 Data Based Methods

Although the GLM is widely used in fMRI data analysis, the assumptions made in this model are still questionable from different aspects. As Alpert et al. [99] pointed out, a constant HRF for each voxel is fundamentally problematic because the HRF shapes have actually been shown to vary across regions, subjects, and even cortical layers. They also questioned the linear relation between the stimulus and the cor-

responding BOLD response, because it has been shown that for a sustained stimulus, the response is actually a sub-linear function of the stimulus duration. McKeown et al. [114] also questioned the approaches used in SPM, which test the signal at each voxel using univariate measures (e.g., t-test) under the hypothesis that the values are distributed under a known probability distribution (e.g. Gaussian). They also raised questions concerning the fact that the variance and covariance between repeated measurements are assumed to be equal, and that the time course (of the design matrix) is estimated in advance by selecting certain HRFs. The GLM is based on the predefined paradigm, therefore, it is more suitable for event-related tasks in which all stimuli of the task can be accurately specified. But for more complicated events, such as some spontaneous stimuli in the brain that are impossible to be pre-defined, a data-driven model is more appropriate and more feasible.

6.3.1 Spatial ICA

The first application of the spatial ICA model for fMRI analysis was proposed by McKeown et al. [114]. According to the authors, the physiological foundation for the ICA model is based on the two complementary principles of brain function, namely localization and connection. Localization implies that each psychomotor function is performed in a small region of the brain area; the principle of connection reveals that the active brain area involved in certain functions may be widely distributed in the multiple distinct brain systems [114]. Based on these two principles, McKeown et al. introduced the spatial ICA model. In this model, the brain areas executing different tasks are assumed to be spatially independent. Each of these areas can be considered as an

independent component associated with a time course. According to the statistical definition of independency, the spatial independence can be defined as:

$$p(\mathbf{c}_1, \mathbf{c}_2, ..., \mathbf{c}_n) = \prod_{i=1}^{n} p_i(\mathbf{c}_i) \tag{6.3.1}$$

where $\mathbf{c}_i$ is the ith independent spatial component, and the joint pdf $p(\cdot)$ is the multiplication of the marginal pdfs of the components. As for the conventional ICA model, the spatial ICA model is formed as:

$$\mathbf{X} = \mathbf{MC} \tag{6.3.2}$$

where $\mathbf{X}$ is a $T \times V$ matrix of the mixtures, T is the length of the fMRI scan, V is the number of brain voxels involved in the analysis, $\mathbf{C}$ is an $N \times V$ matrix of unknown sources, $\mathbf{M}$ is a $T \times N$ mixing matrix, and N is the number of unknown spatially independent sources. Each column of $\mathbf{M}$ represents the time course of the corresponding independent component. Based on this model, fMRI signals can be decomposed into a number of spatially independent components $\mathbf{C}$ and their associated time course of activation $\mathbf{M}$. The spatial components can be estimated from:

$$\mathbf{C} = \mathbf{WX} \tag{6.3.3}$$

where $\mathbf{W}$ is an $N \times T$ unmixing matrix to be estimated, and $\mathbf{W}$ is the pseudoinverse of $\mathbf{M}$, i.e. $\mathbf{W} = \mathbf{M}^{\dagger}$.

In contrast to conventional ICA, which is based on temporal independence, the spatial ICA is based on the assumption of spatial independence. Although some research has exploited both the spatial and

temporal independence [127], most approaches are still based on the assumption of spatial independence due to lack of good understanding of the unknown brain activities for the temporal dynamics of fMRI. Another reason that spatial ICA is more favourable for decomposing fMRI data is that it is computationally less expensive. Temporal and spatial ICA analysis of fMRI data has been compared by Calhoun et al. [121]. Fig. 6.1 illustrates the difference between the two models. It is noticed that, for the mixture, $\mathbf{X}$ (fMRI data matrix) in the spatial model is the transpose of $\mathbf{X}$ in the temporal model, and the spatial dimension is much higher than the temporal one because the number of brain voxels is larger than the number of time points of the scans. For estimation of the unmixing matrix in temporal ICA, a covariance matrix on the order of V^2 must be calculated, which is more computationally expensive than that for spatial ICA. For these reasons, spatial ICA is selected in this work and is denoted as SICA in the following section.

6.3.2 Constrained ICA for fMRI Analysis

The constrained ICA has been applied to fMRI signal analysis in order to incorporate prior information since the SICA model does not take the fMRI time course into account. Although very limited, recent work has shown that the performance of the application of ICA to fMRI analysis is improved if some prior information is incorporated into the estimation process [120]. Lu and Rajapakse [125] applied a predefined stimulus as the reference signal in the temporal ICA model. By minimizing the distance between the output and reference signal, the source component closest to the reference can be obtained. Calhoun et al. developed a

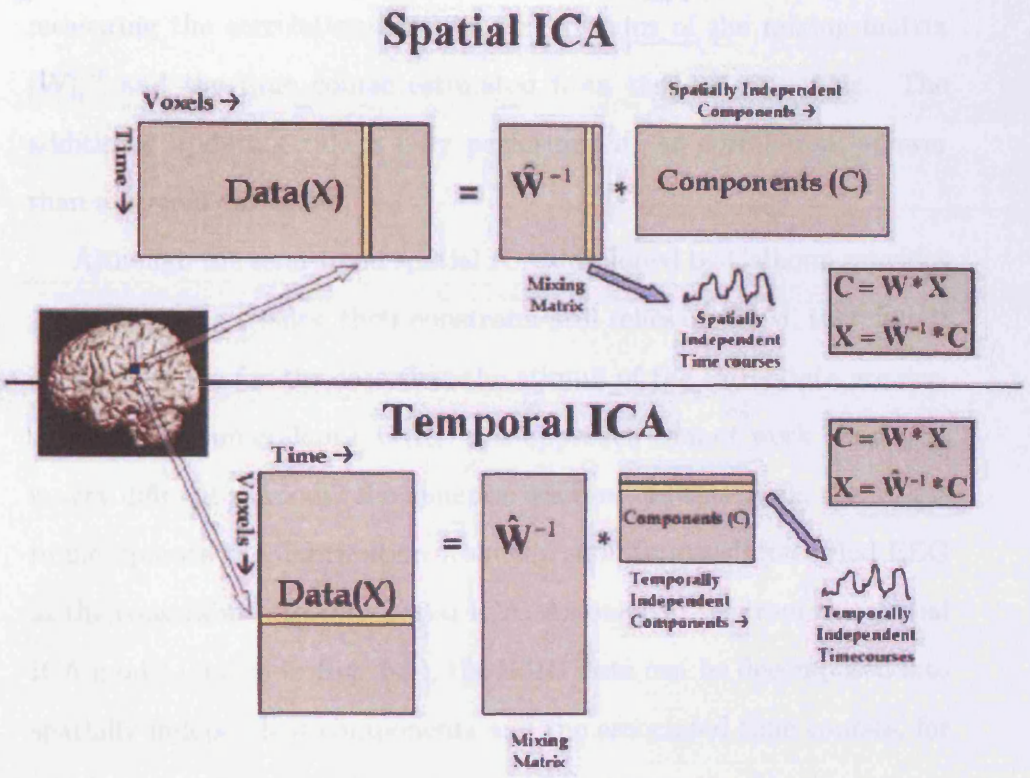

Figure 6.1. Comparison of the key stages of processing within spatial ICA and temporal ICA [121].

semi-blind spatial ICA [126], in which a constraint is introduced by incorporating the GLM design matrix which contains information on the fMRI time course. The column vectors of the mixing matrix are constrained according to their closeness to the time course estimated from the design matrix. At each iteration, apart from updating $\mathbf{w}_i$ based on the Infomax algorithm, an additional updating rule is set by measuring the correlation between the columns of the mixing matrix $[\mathbf{W}]_i^{-1}$ and the time course estimated from the design matrix. The additional updating rule is only performed if the correlation is lower than a certain threshold.

Although the semi-blind spatial ICA developed by Calhoun provides some promising results, their constraint still relies on GLM, therefore it is only suitable for the case that the stimuli of the fMRI data are pre-specified. For an epileptic fMRI, this approach cannot work because it is very difficult to model the epileptic seizures. In this work, the idea is to incorporate the information from the simultaneously recorded EEG as the constraint into the spatial ICA. As one can see from the spatial ICA model (shown in Fig. 6.1), the fMRI data can be decomposed into spatially independent components and the associated time courses, for which each column of the mixing matrix represents the time course of one component activation. Therefore, the temporal constraint can be introduced by linking the EEG with the columns of $\mathbf{W}^{-1}$ in the separation process. In the following section, constrained spatial ICA is denoted CSICA.

6.3.3 Algorithm

The performance of different ICA algorithms for fMRI data separation have been studied by several groups [111] [136] [137]. Basically, selection of the separation algorithm depends on the assumption about the distribution of the sources. For example, fMRI data are commonly assumed to have super-Gaussian distribution [120], from which one can expect that the algorithm which is more suitable for super-Gaussian signals will achieve a better performance. As it will be explained in the following section, Infomax is suitable for super-Gaussian signals. Also as shown in [137], Infomax consistently yields reliable results for separation of fMRI followed by JADE and FastICA. Therefore, Infomax was selected in this work. In the following sections, the principle of Infomax is explained. Then the constraint is introduced to the Infomax learning rule and the development of the constrained algorithm is given.

Infomax

Infomax is based on information theory by maximizing the output entropy or information flow of a neural network with nonlinear outputs, hence the name Infomax. Assume that the neural network with output y and input $\mathbf{x}$ is of the form:

$$y_i = \phi_i(\mathbf{w}_i^T \mathbf{x}) + e \tag{6.3.4}$$

where $\phi_i(\cdot)$ are some nonlinear scalar functions, the $\mathbf{w}_i$ are the weight vectors of the neurons, and e is the additive Gaussian white noise. The

entropy of the output is:

$$H(\mathbf{y}) = H(\phi_1(\mathbf{w}_1^T\mathbf{x}), ..., \phi_n(\mathbf{w}_n^T\mathbf{x})) \tag{6.3.5}$$

For an invertible transformation of the random vector $\mathbf{x}$, $\mathbf{y} = f(\mathbf{x})$, the relation between the entropies of $\mathbf{y}$ and $\mathbf{x}$ can be expressed as [65]

$$H(\mathbf{y}) = H(\mathbf{x}) + E\{log \mid detJf(\mathbf{x}) \mid\} \tag{6.3.6}$$

where $Jf(\cdot)$ is the Jacobian matrix of function $f(\cdot)$. According to Eq. (6.3.6), the transformation of the entropy in Eq. (6.3.5) can be obtained as

$$H(\mathbf{y}) = H(\mathbf{x}) + E\{log \mid det\frac{\partial F}{\partial W}(\mathbf{x}) \mid\} \tag{6.3.7}$$

where $F(\mathbf{x}) = (\phi_1(\mathbf{w}_1^T\mathbf{x}), ..., \phi_n(\mathbf{w}_n^T\mathbf{x}))$ denotes the nonlinear function defined by the neural network. As $H(\mathbf{x})$ is independent of $\mathbf{W}$, the entropy of output can be expressed as

$$H(\mathbf{y}) = \sum_i E\{log\phi_i'(\mathbf{w}_i^T\mathbf{x})\} + log \mid det\mathbf{W} \mid \tag{6.3.8}$$

It is noticed that maximization of the output entropy is very closely related to the maximum likelihood (ML) estimation. The ML estimation yields [133]

$$\triangle\mathbf{W} \propto [(\mathbf{W}^T)^{-1} - \varphi(\mathbf{y})\mathbf{x}^T] \tag{6.3.9}$$

where the nonlinear function $\varphi(\mathbf{y})$ is the column vector whose i-th component is

$$\varphi_i(y_i) = -\frac{\frac{\partial p(y_i)}{\partial y_i}}{p(y_i)} \tag{6.3.10}$$

where $p(y_i)$ is an approximate model of the pdf of the i-th source signal. In practice, $\varphi(y_i) = 2tanh(y_i)$ is selected as it is suitable for super-Gaussian signals [65]. By defining $\varphi(\cdot)$ in a different way, the Infomax can also work for sub-Gaussian signals, which is referred to as extended-Infomax [134].

An efficient way to maximize the log-likelihood is to follow the natural gradient learning method [83],

$$\triangle \mathbf{W} \propto \frac{\partial H(\mathbf{y}, \mathbf{W})}{\partial \mathbf{W}} \mathbf{W}^T \mathbf{W} = [\mathbf{I} - \varphi(\mathbf{y})\mathbf{y}^T]\mathbf{W} \tag{6.3.11}$$

Then, the updating rule can be written as

$$\mathbf{W}(k+1) = \mathbf{W}(k) - \eta(k)[\mathbf{I} - \varphi(\mathbf{y}(k))\mathbf{y}(k)^T]\mathbf{W}(k) \tag{6.3.12}$$

where k is the iteration number, $\mathbf{I}$ is the identity matrix and $\eta(k)$ is the learning rate.

The optimal solution for $\mathbf{W}$ is obtained when the estimated sources y_i and y_j are independent. As shown in [83], the stability condition of the learning rule in Eq. (6.3.11) converges to an equilibrium point corresponding to the optimal solution which can be expressed as $E\{\varphi_i(y_i)y_i\} = 1$. This is not only the condition for local stability of the algorithm, but also determines the scaling of the estimated sources. (This condition is invariant with respect to the sign of y_i as $\varphi_i(y_i)$ is selected as an invertible (monotonic) function $tanh(y_i)$). As Infomax is very similar as ML estimation (see Eq. 6.3.8), the unmixing matrix must be constrained to be orthogonal such that the determinant of $\mathbf{W}$ is one and the second term in Eq. (6.3.8) can be ignored. In practice, $\mathbf{W}$ is usually initiated as the identity matrix, and therefore no more

orthogonalization process will be needed. This is because based on natural gradient learning rule, $\mathbf{W}$ is rescaled in each training iteration by $\mathbf{W}^T\mathbf{W}$.

Constrained Algorithm

In this work, the objective is to incorporate the EEG signal as the constraint into the fMRI data separation process since EEG contains valuable temporal information about the brain activity. As the columns of the mixing matrix represent the time courses of the estimated components, intuitively the temporal constraint can be added to the columns of the mixing matrix such that the EEG information can be taken into account. However, incorporating this information into the separation process is a problem to be resolved.

The relationship between fMRI and EEG is far from straightforward due to the complexity of the brain mechanism and very limited understanding of it at present. Although neural networks have been exploited to model the relationship between fMRI and EEG [92] [93], it is still hard to be established in the neurophysiological and clinical fields, because theoretically the complexity between the hemadynamic changes and neural activities can not be fully represented by a simple mathematical model [91]. Practically, correlation measurement has been widely used in the existing studies for investigating the relationship between fMRI and EEG [90] [101]- [104]. Therefore, in this work, correlation is used to connect the time course of fMRI components and the corresponding EEG signals.

The constraint term reflects the closeness between the ith column vector of the inverse of unmixing matrix $[\mathbf{W}]_i^{-1}$ and the processed EEG

time series $\mathbf{u}$. The seizure signal $\mathbf{u}$ has to be selected carefully either by applying temporal ICA to EEG data to obtain the seizure component, or based on prior clinical information about the seizure. In this work, $\mathbf{u}$ is formed on the basis of prior clinical information, since the epileptogenic zone is known as a *priori.*

The constraint is imposed in the Infomax update rule in Eq. (6.3.9). (A similar method to add a constraint in the natural gradient rule can be found in the nonholonomic learning rules [83] [135]). The basic natural gradient learning equation is then extended as:

$$\mathbf{W}(k+1) = \mathbf{W}(k) - \eta(k)[I - \varphi(\mathbf{y}(k))\mathbf{y}(k)^T - \alpha\Lambda(k)]\mathbf{W}(k) \quad (6.3.13)$$

where α is the factor adjusted based on the stability of the algorithm. $\Lambda = diag\{\Lambda_{ii}\}, i = 1, ..., N$ is a diagonal weight matrix containing the information from the EEG, which is updated as

$$\Lambda(k) = diag(cor([\mathbf{W}]_i^{-1}(k), \mathbf{u})) \quad (6.3.14)$$

where $cor(\cdot)$ denotes correlation. According to the adaptive learning rule in Eq. (6.3.13), $\mathbf{W}$ is updated based on the Infomax principle, also the column vectors of its inverse are forced to be close to the corresponding processed EEG signal $\mathbf{u}$.

As shown in Eq. (6.3.14), Λ is updated iteratively according to the closeness between $[\mathbf{W}]_i^{-1}$ and $\mathbf{u}$. Here, the entries of Λ are bounded since the absolute value of correlation coefficient is less than 1. Due to the additional constraint, the new algorithm can converge to the lower minimum of the cost function than the one before imposing a constraint, whereby the performance of algorithm can be improved.

6.4 Experiments

The experiments comprise two parts. In the first part, both GLM and SICA are applied to the auditory fMRI data. The procedure of using SPM is described and the result from SPM is compared with that from SICA. In the second experiment, SICA and CSICA are applied to the epileptic fMRI data (GLM cannot work in this case because it is impossible to pre-model the epileptic seizure signals). The simultaneously recorded EEG was introduced as the constraint in CSICA and the process of constructing the constraint is described in detail. The performances of SICA and CSICA are compared in terms of algorithm convergence and the closeness between the dominant IC and seizure EEG, which demonstrate the superiority of CSICA.

6.4.1 Preprocessing of fMRI Data

Image Data Format

The primary functional image data format used in this work is Analyze 7.5 [86]. An Analyze 7.5 data format consists of two files, an image file and a header file, with extensions ".img" and ".hdr" respectively. The .img file contains the image data information. The .hdr file contains the volume information of the .img file, such as voxel size, and the number of pixels in the x, y and z directions (dimensions). Also, a MATLAB file .mat is added to the .hdr and .img pair which includes some information on the orientation of the image, generated by the realignment and coregistration processes [86]. In this coordinate system for Analyze data format, the x-direction is from left to right, the y-direction is from back to front, and the z-direction is from bottom to

top. The image obtained from one scan is referred to as one volume. Each volume consists of a number of slices through the brain, and each slice has a certain thickness and is composed of a number of 3D unit elements called voxels (as shown in Fig. 6.2). The volume of a voxel is approximately 3 mm^3. In general, the analysis of fMRI is executed based on each voxel.

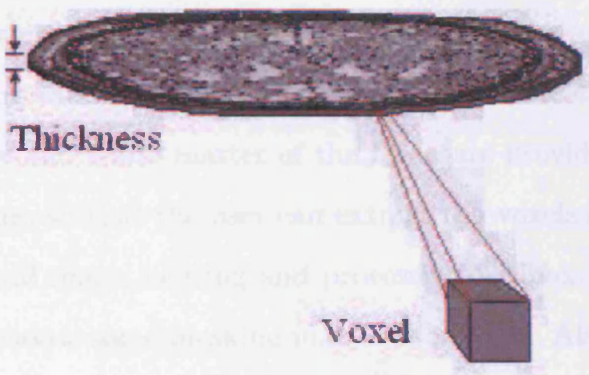

Figure 6.2. Illustration of the voxel in one slice of an MRI image [86].

Preprocessing

In order to apply ICA to the functional data, certain preprocessing must be performed before the data are ready for further analysis. The preprocessing includes not only the basic temporal and spatial preprocessing as needed in SPM, but also the data dimension reduction and data structure conversion which are required before applying ICA.

The first basic step is temporal and spatial preprocessing for the raw fMRI data by means of slice timing and realignment in order to

remove the motion artifacts. In both experiments, this preprocessing is carried out by using the established tool in the SPM.

The second step is data dimension reduction. The analysis of fMRI is always computationally expensive due to the large number of brain voxels. Therefore, a very important step of preprocessing before performing any fMRI analysis is to reduce the number of voxels involved in the analysis, and thereby to reduce the data dimension for further analysis. This can be executed by either removing the off-brain voxels (i.e. the pixels which fall outside the brain boundary), or extracting the voxels within the area of interest. Both processes can be carried out by applying various techniques. For example, in SPM, the standard images of grey and white matter of the brain are provided to be used as mask images, so that the user can extract the voxels of interest. In another medical image viewing and processing toolbox MRIcro [113], the user can choose some masking images as in SPM. Also, in MRIcro, extraction of the region of interest (ROI) can be performed directly by drawing the ROI on the original images manually, then the ROI is converted to the Analyze 7.5 format which is readable in SPM. In the Matlab based software FMRLAB [112], the off-brain voxels are excluded by manually setting a threshold value. The user can visually check the changes in brain images during the process of removing off-brain voxels in the graphic interface, and decide on the threshold value. In the following experiments, the toolbox in FMRLAB was used to extract the brain voxels.

In the case of applying GLM to fMRI analysis, the above two steps of preprocessing are required. But for applying ICA to fMRI, one also needs to construct the input (data mixture) in order to perform the

ICA. As seen from the ICA model (Eq. 6.3.2), the input data mixture has dimensions of $T \times V$, where T is the number of scans and V is the number of brain voxels involved in the analysis, which are the voxels after excluding the off-brain voxels. For each scan (one time point of fMRI data), which is referred to as one volume, the data are in 3D form (i.e., with X, Y and Z directions). In order to construct the 2D mixture with size $T \times V$, it is necessary to first compress all scans into a 4D dataset, which is $T \times X \times Y \times Z$, then reshape the 2D mixture into the dimension $T \times V$, in which V is smaller than $X \times Y \times Z$ since the unnecessary voxels are excluded in the second step.

In all experiments, the data were first centred to have zero mean. Then preliminary whitening was performed to make the data have unit variance before further separation processing. The estimation of number of spatial components in fMRI has been attempted recently [138], in which the information-theoretic criteria was applied on the simulated data based on the minimization of the Kullback-Leibler divergence between the true model and the fitted model. However, it is still a relatively new research topic and many questions remain. In this study, the number of source was selected as the same as the number of input channels, which is the time points of fMRI data.

6.4.2 Experiment I: Analysis of Auditory fMRI Data

Data Details

In this experiment, the single subject fMRI data from a block auditory activation experiment were used. The preprocessed data set was downloaded from the SPM web site [109]. In total 96 acquisitions were made in blocks of 6, with a repeat time (RT) of 7s between scans. The

condition for successive blocks alternated between rest and auditory stimulation, starting with rest. The functional data started acquisition at the 4th scan and the first few scans were discarded. These whole brain BOLD images were acquired on a modified 2T Siemens MAGNETOM Vision system. Each acquisition consisted of 64 contiguous slices, giving the image dimension of $64 \times 64 \times 64$ and voxel size of $3mm \times 3mm \times 3mm$.

Results from SPM

The model was first specified in SPM, in which one needs to select the fMRI scans, to specify the details of the stimulus such as time and period, and to choose the pre-defined HRF to be convoluted with the stimulus to format the design matrix. The parameter estimation was carried out after model specification. Then, the statistical significance of the parameters was evaluated by the t-statistic and the area of activation was shown in the brain volume. Fig. 6.3 gives the results of the statistical parameter mapping, from which one can see that the BOLD area is located at the auditory region.

Figure 6.3. The analysis results for the auditory activation experiment obtained from SPM.

Results from SICA

The raw fMRI data were first compressed into 4D data format using MRIcro, then the off-brain voxels were excluded in FMRLAB. The SICA algorithm was then applied to the functional data. The dominant independent component was selected based on the prior information of the region of interest. The BOLD of the selected dominant IC is shown in Fig. 6.4 as the highlighted area, comprising voxels with z-value (normalized standard deviation) higher than the predefined threshold (which is set to 1.5 in this experiment). It is seen that the highlighted area is also located in the auditory region, but more focused than the result from SPM.

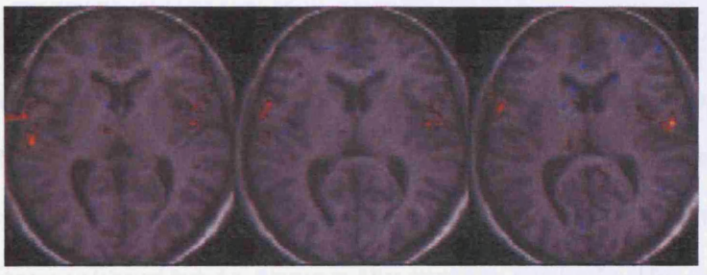

Figure 6.4. The analysis results for the auditory activation experiment obtained from SICA.

6.4.3 Experiment II: Analysis of Epileptic EEG-fMRI

Data Details

The simultaneously recorded EEG and fMRI data were obtained from the National Society for Epilepsy, University College London (UCL). The functional data were acquired on a modified 3T GE Horizon system and EEG data were recorded by the Brain Product system. The length of EEG-fMRI data is approximately 5 mins before and during

the seizure onset. The functional data were acquired from the 16^{th} scan. In this experiment, the functional data were truncated from acquisition 20 to acquisition 107, which is the scan just before seizure onset. The first four scans were discarded in order to remove the initial magnetic gradient effect in the fMRI recording. Each acquisition comprised 47 contiguous slices, with image dimension of $64 \times 64 \times 47$, and the volume size was $3.75mm \times 3.75mm \times 2.5mm$. The interval between each scan, the RT, was 3 sec. The simultaneous 64 channel EEGs were sampled at 250 Hz. Before applying the proposed algorithm over the simultaneous EEG-fMRI data, the scanner artifacts were removed by the data provider.

Experiment Setup

In this experiment, SICA and CSICA were applied to the epileptic EEG-fMRI data and the performances of these two algorithms were compared. The functional data were preprocessed as in the first experiment. After realignment to remove the motion artifacts, the raw data were first compressed into 4D format, then the off-brain voxels were removed and the 2D data were constructed for ICA.

As described in the above section, the constraint was formulated as the closeness between the EEG information and the column vectors of the mixing matrix, in which the closeness was measured by correlation. The special electrodes F8 and P8, which contain the most significant seizure information, were selected as the reference signal as suggested by the clinical consultant.

For measuring the correlation, the difference in resolution between the EEG and fMRI must be resolved first, because the temporal resolu-

tion of EEG is much higher than that of fMRI time series. In order to solve this problem, the following process was performed: (1) selecting electrode P8 or F8 as the EEG reference signal; (2) filtering the reference signal by lowpass filter with cut-off frequency 15 Hz, thus ensuring that the important seizure information is kept (because the frequency of seizure is in the range 2.5 to 15 Hz [74] [75]); (3) down-sampling the reference EEG and up-sampling each column of the mixing matrix to ensure that they have the same data length; (4) measuring the correlation between reference EEG and columns of the mixing matrix.

Results and Discussion

SICA and the proposed CSICA were applied to the processed fMRI data. In each iteration of CSICA, the correlation between the column vectors of $\mathbf{W}^{-1}$ and the EEG reference vector was measured as the factor of constraint. Then, the unmixing matrix $\mathbf{W}$ was updated according to Eq. (6.3.13). The performances of the two algorithms were compared in terms of convergence, the correlation between the seizure EEG and the corresponding columns of the mixing matrix, and the mapping of the selected component.

Fig. 6.5 gives the algorithm convergence curve, and clearly shows that the proposed CSICA algorithm converges to the local minimum of the cost function, which is less than that for unconstrained SICA. Fig. 6.6 illustrates the region of activation obtained from both algorithms. The level of activity is represented by the normalized standard deviation (z-value). The activation area is the brain area in which the voxels have a higher z-value than the threshold level (1.5 in this experimental result). The mapping of the component (activated area) is then dis-

played by overlaying the area on top of the high resolution structural images. Based on the clinical expertise, the highlighted part in the left frontal area is introduced as the MRI scan noise, and the right temporal area is verified to be within the epileptic zone. This means that the detected BOLD is in line with the clinical findings. Also based on clinical investigations, the small patch at the right temporal region is more focused in the result obtained from CSICA.

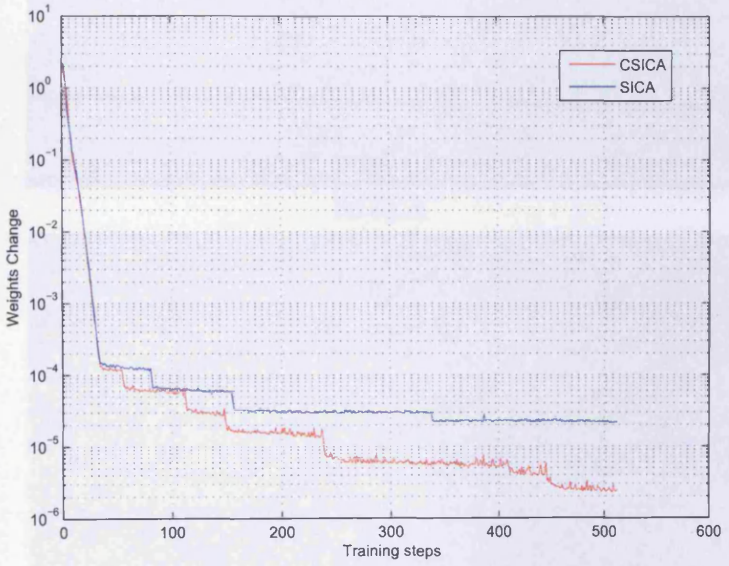

Figure 6.5. Comparison of algorithm convergence for SICA and CSICA.

Table 6.1 gives the maximum correlation coefficients between the column vectors of the mixing matrix and the EEGs, which were obtained by averaging five trials for each algorithm. It can be seen that the results from CSICA provide a higher correlation between the seizure signal and the corresponding column vectors of $\mathbf{W}^{-1}$ than that the results from SICA.

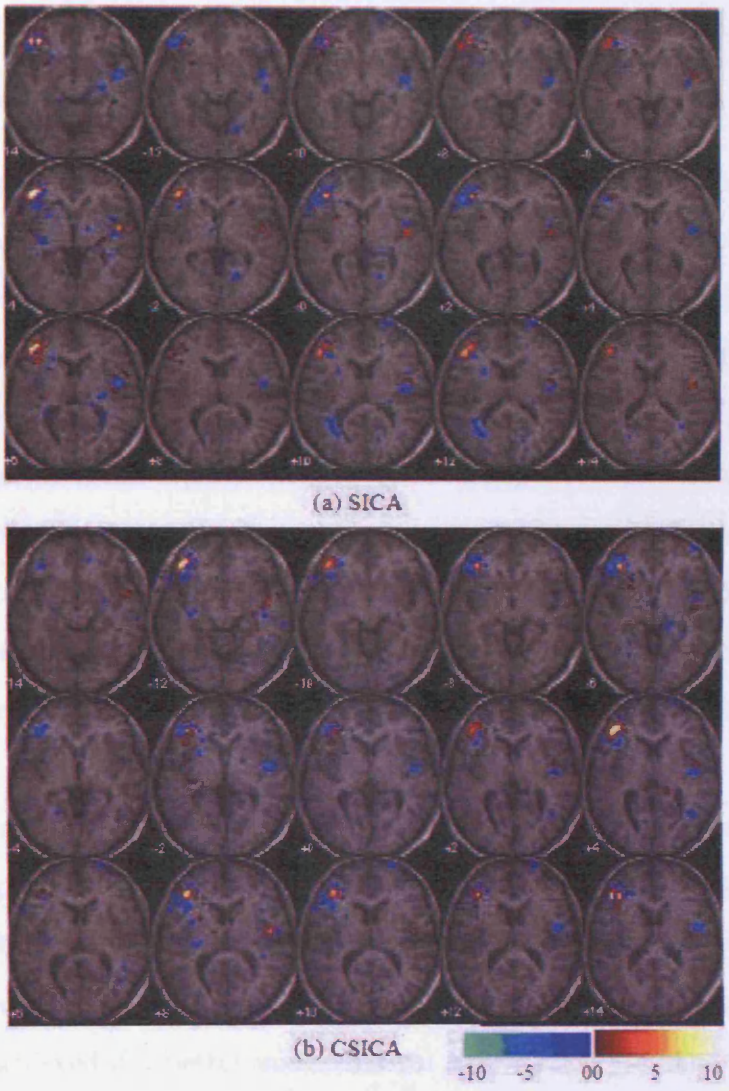

Figure 6.6. The BOLD obtained from separation of fMRI data by using (a) SICA and (b) the proposed CSICA, which incorporates the EEG signals as the constraint into the update equation.

Table 6.1. The maximum correlation coefficient between the EEG and the column vectors of mixing matrix.

SICA	CSICA
0.181	0.195

6.5 Conclusions

In this chapter, various techniques for fMRI analysis have been reviewed and the established techniques such as GLM and SICA have been discussed in terms of their mathematical frameworks. More importantly, for the first time, a novel constrained spatial ICA algorithm has been proposed which incorporates the simultaneously recorded seizure EEG into the fMRI separation process. The experimental results have shown that the BOLD region, as the result of seizure onset, has been detected using the proposed constrained SICA. This algorithm outperforms the existing unconstrained ICA algorithm in terms of convergence and closeness between the component time course and the seizure EEG signals.

The relationship between fMRI and EEG has indeed been a challenging problem to date, therefore in this study, this relationship was simply chosen by closeness between time course of fMRI component and processed EEG signal. Further improvements to the proposed method can be achieved if a better mathematical modelling of the relationship between EEG and fMRI can be developed. Another limitation of the proposed method is that the EEG signal used in this work was the scalp EEG, which is the signal that is mixed with noise and artifacts, and is therefore not a perfect choice for seizure reference. This may be the reason why the obtained results for the correlation measurement are not sufficiently significant. Further investigations can be carried out

by applying a proper ICA algorithm to extract the seizure component. These can be an agenda for future research in this area. Nevertheless, the results presented here are still very promising, and have shown a new direction for fusion of fMRI and EEG. The idea can be further exploited in both separation and localization of seizure signals in joint EEG-fMRI signal processing.

Chapter 7

CONCLUSION

7.1 Discussion

Perspective of Applications

The results presented in this work have shown a very promising perspective for seizure prediction based upon the non-invasive approach. Although BSS has been of theoretical interest in seizure signal separation [52]- [55] [63], very few studies [42] have attempted BSS for separation of EEGs for seizure prediction, because there are still many questions remaining in the application of BSS to brain signal separation. Apart from the limitation of ICA itself, the complexity of brain functions sometimes may make the results obtained from ICA difficult to be interpreted physiologically, which may lead to doubts about the accuracy of the estimated sources.

The work presented in this thesis has shown that as a consequence of applying a well developed separation algorithm, the predictability of seizure from the scalp EEG can be verified. The proposed CTICA algorithm has demonstrated a better performance compared to other ICA methods. First, the TICA model relaxes the assumption of independence and therefore is more suitable for brain signal separation. Second, CTICA introduces an averaged and band-limited reference sig-

nal, which further constrains the TICA model based on the spatial and frequency domain properties of the seizure signal. The reference signal can be constructed based on long time recorded EEGs, which can continuously capture the dynamic changes within the epileptic brain. Third, by imposing the constraint, the source closest to the reference can be obtained and the dynamic changes of the source can be exploited in the prediction. The presented results have suggested a great potential in applying the CTICA to real application of seizure prediction.

Fusion of EEG and fMRI is a relatively new topic in research field. There are very limited studies [121] which have attempted ICA to the combined EEG and fMRI. The results presented in this work have provided a stepping stone in the forefront of this new field. For the first time, the temporal information from EEG has been incorporated into the spatial ICA model for fMRI analysis. This provides a new technique in which the information from EEG and fMRI can be fused through a mathematical model. Not only this, the presented work also has established a new method for mapping of the spontaneous brain activity, which is the problem that can not be solved by using the popular approach of general linear model (GLM). The overall results may have more meaningful impact on the methodology development for the human brain function mapping in neuroscience.

Limitations and Future Work

First, the ICA model has its own limitations. Although the ambiguity of scaling can be overcome by data preprocessing or imposing some constraints on the sources and unmixing matrix, the evaluation of the exact number of sources remains an open question in all applications of ICA,

even though some methods have been suggested in the literature [8] - [16]. In the presented work, the number of sources was assumed to be equal or less than the number of sensors. The case when there are more sources than sensors, is of theoretical and practical interest. Further studies on this subject may help to improve the proposed methods.

Second, the TICA model has some limitations. Based on this model, the nearby sources can be grouped together in the output. However, the results have shown that it can also group the artifact with the desired source if they are geometrically close to each other and active at the same time. This is one reason that when TICA is applied to the real EEG data, the effect of grouping nearby sources might not be very ideal. The strategy to overcome this problem can be by developing a proper neighbourhood function based on the statistical properties of the desired source, by which the artifacts and ideal source can be clustered in the different groups even they are close to each other.

Third, much more work needs to be done in fusion of EEG and fMRI. Further exploration of the relation between EEG and fMRI, and developing more complex probabilistic models especially if larger data sets are available, may provide more solid foundation for combination for these two modalities. Further study may provide an engineering ground to fully exploit and illustrate the functional, anatomical, pathological, and physiological characteristics of the human brain.

In addition to these limitations, it is also worthwhile to apply the CTICA to more real epileptic EEG data sets, therefore the robustness of the algorithm can be further investigated.

7.2 Conclusions

In this thesis, the predictability of epileptic seizure based on the scalp EEGs has been investigated by applying BSS techniques and nonlinear analysis method. The proposed CTICA algorithm not only relaxed the assumption of independency of the sources, but also constrained the TICA model based on the spatial and frequency domain properties of the seizure signal by using an averaged and band-limited reference signal. The results have demonstrated that CTICA achieved a better separation performance for seizure EEGs than other ICA methods. The results based on the data from three epileptic patients have shown that the chaos measurement (using Lyapunov exponent) after application of the CTICA has similar trend as that estimated from the intracranial EEGs. Fusion of EEG and fMRI has also been studied. By applying a blind source extraction (BSE) algorithm, the effect of fMRI scanner artifacts are reduced effectively from simultaneously recorded EEGs. By introducing the EEG as a temporal constraint into the spatial ICA, the seizure BOLD has been detected effectively. The overall results from the present work have demonstrated a very promising technique for seizure prediction using combined EEG and fMRI analysis.

APPENDIX: EMBEDDING-SPACE DECOMPOSITION

Roberts et al. [51] proposed a method of embedding-space decomposition to measure the signal's complexity. In their study, this method was applied to track the changes of complexity in multichannel EEG time series. This method has been successfully applied to identification of the seizure components which are separated from ICA by James [53] and Paul [54]. Because epileptic seizure presents the nonlinear dynamic changes prior to seizure onset, one can expect to see the complexity change as a seizure signal becomes more apparent.

As for all nonlinear analysis methods, the EEG time series are firstly reconstructed based on Taken's delay-embedding theorem [23]. Given an EEG data segment $\mathbf{x}(t)$ with the number of time points N, then at time t_i, the vector $\mathbf{x}_i$ in the phase space can be constructed by:

$$\mathbf{x}_i = [x(t_i), x(t_i + \tau), ..., x(t_i + (p-1)\tau)]^T \qquad (8.2.1)$$

where the value τ is the selected time lag between the elements of each vector in the phase space, p is the dimension of the embedding phase

space, and $t_i \in [1, N-(p-1)\tau]$. According to Takens' Theorem, the embedding dimension p has to be at least equal to $(2d+1)$, where d is the attractor dimension. In Roberts' method, p was chosen large enough in order to capture as much information as possible. According to the literature, p varies from 20 to 90 in different experiments. In this thesis work, the parameters are chosen based on the experiment in [53], $\tau = 1$ and $p = 90$.

Secondly, subspace decomposition of the reconstructed matrix is performed by using singular value decomposition (SVD).

$$X = USV^T \tag{8.2.2}$$

where X is an $N \times p$ embedding matrix, U and V are orthogonal. S is a diagonal matrix with elements $S_{ii} = \sigma_i$, where σ_i is the singular values and $\sigma_i \geq 0$. S defines the singular value spectrum, which describes the signal and noise structure in the observed data. Therefore, for a number of consecutive data segment, the relative complexity can be reflected in the changes of singular value spectrum, which the change is measured by means of entropy. Normalising the singular values such that

$$\sigma = \sigma_i / \sum_{i}^{p} \sigma_i \tag{8.2.3}$$

The entropy is defined as

$$H = -\sum_{i=1}^{p} \sigma log\sigma \tag{8.2.4}$$

Choosing a logarithmic base of 2, the complexity, given the entropy

measure, is defined as

$$\Omega = 2^H \tag{8.2.5}$$

In this work, the parameters used for measuring the complexity were decided based on the results presented in [53] and [54]. The parameters include: embedding dimension $p = 90$, lag $\tau = 1$, length of segment to reconstruct an embedding matrix was chosen as 290, and an embedding matrix was reconstructed every 100ms.

A simple example showing this method is given in Fig. 8.1, which shows one generated signal and the complexity measured by method of embedding-space decomposition. It is seen that the complexity increases when the signal becomes more irregular. For the epileptic seizure analysis, the complexity is expecting to drop due to the seizure presents the transition from chaos to order when brain state changes from preictal to ictal stage.

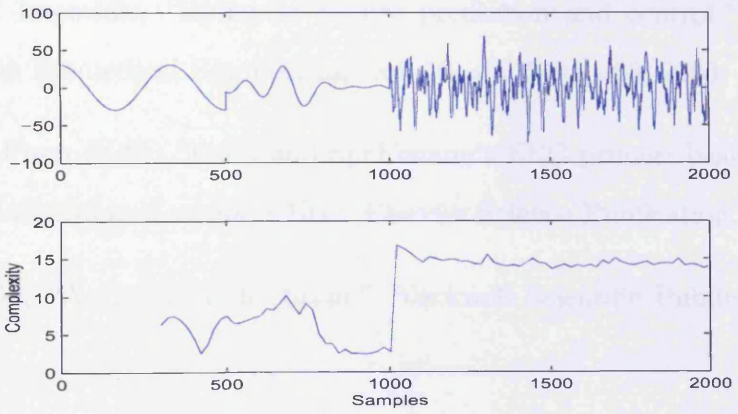

Figure 8.1. Measure of the complexity of the generated signal by embedding-space decomposition.

BIBLIOGRAPHY

[1] E. Niedermeyer and F. L. D. Silva "Electroencephalography: Basic Principle, Clinical Application, and Related Field," Williams and Wilkins, 1998.

[2] R. J. Porter, "Epilepsy, 100 elementary principles," London: Edward Arnold, 1998.

[3] R . S. J. Frackowiak, K. J. Friston, C. D. Firth, R. J. Dolan and J. C. Mazziotta, "Human brain function," Academic Press, 1997.

[4] L. D. Iasemidis, "Epileptic seizure prediction and control," IEEE Trans. on Biomedical Engineering, vol. 50, pp. 549 - 558, 2003.

[5] B. J. Fisch (Edit),"Fisch and Spehlmann's EEG primer: basic principles of digital and analog EEG," Elsevier Science Publication, 1999.

[6] S. Zeki, "A vision of the brain," Blackwell Scientific Publications, 1993.

[7] A. Hyvärinen and P. O. Hoyer, "Independent component analysis: algorithms and applications," Neural Networks, vol. 13, pp. 411 - 430, 2000.

[8] X. R. Cao and R. W. Liu, "General approach to blind source sepa-

ration," IEEE Transactions on Signal Processing, vol. 44, Issue 3, pp. 562 - 571, 1996.

[9] M. S. Lewicki and T. J. Sejnowski, "Learning overcomplete representations," Neural Computing, vol. 12, no. 2, pp. 337-365, 2000.

[10] Y. Luo, W. Wang, J. A. Chambers, S. Lambotharan and I. Proudler, "Exploitation of source nonstationarity in underdetermined blind source separation with advanced clustering techniques," IEEE Trans. on Signal Processing, Vol. 54, Issue 6, pp. 2198 - 2212, June 2006.

[11] A. Cichocki, J. Karhunen, W. Kasprzak and R. Viga, "Neural networks for blind separation with unknown number of sources," Neurocomputing, vol. 24, pp. 55 - 93, 1999.

[12] T. Y. Sun, C. C. Liu, S. T. Hsieh and S. J. Tsai, "Blind separation with unknown number of sources based on auto-trimmed neural network," Neurocomputing, available online, doi:10.1016/j.neucom.2007.07.036, 2008.

[13] J. Karhunen, A. Cichocki, W. Kasprzak and P. Pajunen, "On neural blind separation with noise suppression and redundancy reduction," Int. J. Neural Systems, vol. 8, pp. 219 - 237, 1997.

[14] X. Bai and B. He, "Estimation of Number of Independent Brain Electric Sources from the Scalp EEGs," IEEE Tran. on Biomedical Engineering, vol. 53, no. 10, pp. 1883 - 1892, 2006.

[15] L. J. Waldorp, H. M. Huizenga, C. V. Dolan, and P. C. M. Molenaar, "Estimated generalized least squares electromagnetic source analysis

based on a parametric noise covariance model [EEG/MEG]," IEEE Trans. Biomed. Eng., vol. 48, no. 6, pp. 737741, Jun. 2001.

[16] T. Knosche, E. Berends, H. Jagers and M. Peters, "Determining the number of independent sources of the EEG: A simulation study on information criteria," Brain Topography, vol. 11, pp. 111-124, 1998.

[17] J. F. Cardoso, A. Souloumiac and T. Paris, "Blind beamforming for non gaussian signals," IEE-Proccedings-F, vol. 140, no. 6, pp. 362 - 370, 1993.

[18] A. Belouchrani, K. Abed-Meraim, J. F. Cardoso and E. Moulines, "A blind source separation technique using second-order statistics," IEEE Trans. on signal processing, vol. 45, no. 2, pp. 434 - 444, 1997.

[19] W. G. Lennox, "Science and seizure," New York: Harper, 1946.

[20] S. S. Viglion and G. O. Walsh, "Epileptic seizure prediction," Electroencephalogr. Clin. Neurophysiol., vol. 39, pp. 435, 1975.

[21] H. H. Lange, J. P. Lieb, J. Engel, and P. H. Crandall, "Temporo-spatial patterns of preictal spike activity in human temporal lobe epilepsy," Electroencephalogr. Clin. Neurophysiol., vol. 56, pp. 543 - 555, 1983.

[22] J. Gotman, J. Ives, P. Gloor, A. Olivier, and L. F. Quesney, "Changes in interictal EEG spiking and seizure occurrence in humans," Epilepsia, vol. 23, pp. 432433, 1982.

[23] S. Haykin, J. Principe, "Making Sense of a Complex world," IEEE Signal Processing Magazine, pp, 66-81, May, 1998.

[24] F. Takens, "On the numerical determination of the dimension of an attractor," In D.Rand and L.S.Young, editors, "Dynamical Systems and Turbulence," Warwick 1980 Lecture Notes in Mathematics, vol. 898, pp. 366 - 381, Springer-Verlag, 1981.

[25] H. D. I. Abarbanel, T. W. Frison, and L. S. Tsimring, "Obtain Order in a World of Chaos, Time-Domain Analysis of Nonlinear and Chaotic Signals," IEEE Signal Processing Magazine pp. 49-65, May, 1998.

[26] Edited by M. Akay, "Nonlinear biomedical signal processing," volume II. Dartmouth College, Hanover, NH, 2000.

[27] K. Falconer "Fractal Geometry: Mathematical Foundations and Applications," John Wiley and Sons, ISBN 0-470-84862-6, 2003.

[28] L. D. Iasemidis, J. C. Principle, and J. C. Sackllares, "Measurement and quantification of spatio-temporal dynamics of human epileptic seizures," Nonlinear biomedical signal processing, vol.2, pp. 294-318, 2000.

[29] L. D. Iasemidis, D. S. Shiau, W. Chaovalitwongse and J. C. Sackellares,"Adaptive epileptic seizure prediction system," IEEE Trans. on Biomedical Engineering, vol. 50, pp. 616-626, 2003.

[30] A. Wolf, J. B. Swift, H. L. Swinney, and J. A. Vastano, "Determining Lyapunov exponents from a time series," Physica D, vol.16, pp. 285-317, 1985.

[31] L. D. Iasemidis, J. C. Sackllares, Z. H. P and W. J. Williams, "Phase space topograhy of the electrocorticogram and the Lyapunov exponent in partial seizures," Brain Topogr., vol. 2, pp. 187 - 201, 1990.

[32] K. Lehnertz and C. E. Elger, "Spatio-temporal dynamics of the primary epileptogenic area in temporal lobe epilepsy characterized by neuronal complexity loss," Electroencephalography and clinical Neurophysiology, vol. 95, pp. 108-117, 1995.

[33] K. Lehnertz, R. G. Andrzejak and J. Arnhold, "Nonlinear EEG Analysis in Epilepsy: Its Possible Use for Interictal Focus Localization, Seizure Anticipation, and Prevention," Journal of Clinical Neurophysiology, vol. 18(3), pp. 209 - 222, 2001.

[34] I. Osorio, M. A. F. Harrison, Y. C. Lai, "Observation on the application of the correlation dimension and correlation integral to the prediction of seizures," Journal of Clincal Neurophysiology, vol. 18, no. 3, pp. 269 - 274, 2001.

[35] M. L. V. Quyen, J. Martinerie, M. Baulac and F. J. Varela, "Anticipating epileptic seizure in real time by a nonlinear analysis of similarity between EEG recordings," Neuro Report, vol. 10, pp. 2149 - 2155, 1999.

[36] J. C. Sackellares, L. D. Iasemidis, D. S. Shiau, R. L. Gilmore and S. N. Roper, "Detection of the preictal transition from scalp EEG recordings," Epilepsia, vol. 40(S7), pp.176, 1999.

[37] D. S. Shiau and L. D. Iasemidis, "Detection of the preictal period by dynamical analysis of scalp EEG," Epilepsia, vol.44 (S.9), pp. 233-234, 2003.

[38] J. Gotman and P. Gloor, "Automatic recognition and quantification of interictal epileptic activity in the human scalp EEG," Electroencephalogr. Clin. Neurophysiol. vol. 41, pp. 513-529, 1976.

[39] L. M. Hively, V. A. Protopopescu and P. C. Gailey, "Timely detection of dynamic change in scalp EEG signals," Chaos, vol. 10, pp. 864 - 875, 2000.

[40] L. M. Hively and V. A. Protopopescu, "Channel-consistent forewarning of epileptic events from scalp EEG," IEEE Trans. on Biomedical Engineering, vol. 50, no. 5, pp. 584 - 593, 2003.

[41] M. L. V. Quyen, J. Martinerie, V. Navarro, M. Baulac and F. J. Varela, "Characterizing neurodynamic changes before seizures," J. Clin. Neurophysiol., vol. 18, no. 3, pp, 191-208, 2001.

[42] J. Corsini, L. Shoker, S. Sanei, and G. Alarcon, "Epileptic seizure predictability from scalp EEG incorporating BSS," IEEE Trans. on Biomedical Engineering, vol. 53, no. 5, pp. 1654 - 1669, 2006.

[43] B. Litt, R. Esteller, J. Echauz, M. D. Alessandro, R. Shor, T. Henry, P. Pennell, C. Epstein, R. Bakay, M. Dichter, and G. Vachtsevanos, "Epileptic seizures may begin hours in advance of clinical onset: a report of five patients," Neuron, vol. 30, pp. 5164, 2001.

[44] A. Petrosian, D. Prokhorov, R. Homan, R. Dashei and D. Wunsch, "Recurrent neural network based prediction of epileptic seizures in intra- and extracranial EEG," Neurocomputing, vol. 30, pp. 201 - 218, 2000.

[45] F. H. L da Silva, "EEG analysis: theory and practice," In: E. Niedermayer and F. H. L. D. Silva (Edit), "Electroencephalography, Basic Principles, Clinical Applications and Related Fields," Urban and Schwarzenberg, Baltimore, MD, pp. 871-897, 1987.

[46] F. H. L. D. Silva, W. Blanes, S. N. Kalitzin, J. Parra, P. Suffczynski, and D. N. Velis, "Dynamical diseases of brain systems: different routes to epileptic seizures," IEEE Trans. on Biomedical Engineering, vol. 50, pp. 540-548, 2003.

[47] S. Sanei and J. Chambers, "EEG Signal Processing," John Wiley - Sons, 2007.

[48] L. Zhukov, D. Weinstein and C. Johnson, "Independent component analysis for EEG source localization," IEEE Engineering in Medicine and Biology Magazine, vol. 19, Issue 3, pp. 87 - 96, 2000.

[49] M. A. Latif, S. Sanei, J. Chambers, and L. Shoker, "Localization of Abnormal EEG Sources Using Blind Source Separation Partially Constrained by the Locations of Known Sources" IEEE Signal Processing Letters, vol. 13, no. 3, pp. 117 - 120, 2006.

[50] L. Spyrou, M. Jing, S. Sanei, and A. Sumich "Separation and Localisation of P300 Sources and Their Subcomponents Using Constrained Blind Source Separation," EURASIP J. on Advances in Signal Processing, vol. 2007, pp. 1-10, 2007.

[51] S. J. Roberts, W. Penny and I. Rezek,"Temporal and spatial complexity measures for EEG based brain-computer interfacing," Medical and Biological Engineering and Computing, vol. 37, no. 1, pp. 93-99, 1998.

[52] A. J. R. Leal, A. I. Dias and J. P. Vieira "Analysis of the EEG dynamics of epileptic activity in gelastic seizures using decomposition in independent components," Clinical Neurophysiology, vol. 117, pp. 1595-1601, 2006.

[53] C. J. James and D. Lowe,"Using dynamical embedding to isolate seizure components in the ictal EEG," Science, Measurement and Technology, IEE Proceedings, vol. 147, issue 6, pp. 315 - 320, Nov. 2000.

[54] S. Paul, L. Marnane, G. Lightbody, G. Boylan and S. Connolly "A method for the blind separation of sources for use as the first stage of a neonatal seizure detection system," IEEE International Conference on Acoustics, Speech, and Signal Processing, 2005. (ICASSP '05), vol. 5, pp. 409 - 412, March 2005.

[55] C. W. Hesse and C. J. James, "Tracking Epileptiform Activity in the Multichannel Ictal EEG using Spatially Constrained Independent Component Analysis", 27th Annual International Conference of Engineering in Medicine and Biology Society (IEEE-EMBS 2005), pp. 2067 - 2070, 2005.

[56] L. Shoker, S. Sanei and J. Chambers, "Artifact Removal From Electroencephalograms Using a Hybrid BSS-SVM Algorithm, " IEEE Signal Processing Letters, vol. 12, no. 10, pp. 721 - 724, 2005.

[57] W. Nakamura, K. Anami, T. Mori, O. Saitoh, A. Cichocki and S. Amari, "Removal of ballistocardiogram artifacts from simultaneously recorded EEG and fMRI data using independent component analysis," IEEE Transactions on Biomedical Engineering, vol. 53, issue 7, pp. 1294 - 1308, July, 2006.

[58] W. D. Clercq, A. Vergult, B. Vanrumste, W. V. Paesschen and S. V. Huffel, "Canonical Correlation Analysis Applied to Remove Muscle Artifacts From the Electroencephalogram," IEEE Transactions on Biomedical Engineering, vol. 53, issue 12, pp. 2583 - 2587, Nov., 2006.

[59] N. Ille, P. Berg and M. Scherg, "Artifact correction of the ongoing EEG using spatial filters based on artifact and brain signal topographies," J. Clin. Neurophysiol., vol. 19, no. 2, pp. 113-124, 2002.

[60] N. Ille, R. Beucker and M. Scherg, "Spatially constrained independent component analysis for artifact correction in EEG and MEG," Neuroimage, vol. 13, S159, 2001.

[61] W. Lu and J. C. Rajapakse, "Constrained independent component analysis," in: T. Leen, T. Dietterich, V. Tresp (Eds.), Advances in Neural Information Processing Systems, Vol. 10, MIT Press, Cambridge, MA, 2001.

[62] C. J. James and O. J. Gibson, "Temporally constrained ICA: an application to artifact rejection in electromagnetic brain signal analysis," IEEE Transactions on Biomedical Engineering, vol. 50, Issue 9, pp. 1108 - 1116, 2003.

[63] C. W. Hesse and C. J. James,"On Semi-Blind Source Separation Using Spatial Constraints With Application in EEG Analysis," IEEE Tran. Biomedical Engineering, vol. 53, pp. 2525- 2533, 2006.

[64] W. Lu and J. C. Rajapakseb, "ICA with Reference," Neurocomputing, vol. 69, pp. 2244 - 2257, 2006.

[65] A. Hyvärinen, J. Karhunen and E. Oja, "Independent Component Analysis", Wiley-Interscince Publication, 2001.

[66] A. Hyvärinen, P. O. Hoyer and M. Inki, " Topographic Independent Component Analysis," Neural Computation, vol. 13, pp. 1527-1558, 2001.

[67] A. Hyvärinen, and P. O. Hoyer, "Emergence of phase and shift invariant features by decomposition of natural images into independent feature subspaces," Neural Computation, vol. 12, no. 7, pp. 1705 - 1720, 2000.

[68] S. Haykin, "Adaptive Filter Theory (Fourth Edition)", Prentic-Hall, Inc. Upper Saddle River, New Jersey, 2002.

[69] W. Lu and J. C. Rajapakse. "Eliminating indeterminacy in ICA," Neurocomputing, vol. 50, pp. 271 - 290, 2003.

[70] EEGLAB, http://sccn.ucsd.edu/eeglab/index.html

[71] C. P. Wnsworth, J. Syowart, G. Luwson, J. K. Brown, B. Mulgrew, R. A. Minns and M. Clark, "A New Method: To Determine the Applicability of Linear ICA to a Given Problem (Highlighted by an EEG Case Study Applied to Epilepsy)," IEEE Sensor Array and Multichannel Signal Processing Workshop, pp. 182-185, 2004.

[72] K. H. Knuth and A. Mohammad-Djafari "Bayesian source separation and localization," SPIE98 Proceedings: Bayesian Inference for Inverse Problems, San Diego, pp. 147 - 158, 1998.

[73] P. J. Franaszczuk, G. K. Bergey, P. J. Durka and H. M. Eisenberg, "Time-frequency analysis using the Matching Pursuit algorithm applied to seizures originating from the mesial temporal lobe," Electroencephalogr. Clin. Neurophysiol., vol. 106, pp. 513-521, 1998.

[74] G. Lantz, C. M. Michel, M. Seeck, O. Blanke, T. Landis, and I. Rose, "Frequency domain EEG source localization of ictal epileptiform activity in patients with partial complex epilepsy of temporal lobe origin," Clin. Neurophysiol., vol. 110, pp. 176 - 184, 1999.

[75] O. Blanke G. Lantz, M. Seeck, L. Spinelli, R. G. D. Peralta, G. Thut, T. Landis and C. M. Michel, "Temporal and Spatial Determination of EEG-Seizure Onset in the Frequency Domain," Clin. Neurophysiol., vol. 111, pp. 763-772, 2000.

[76] P. Wahlberg and G. Lantz, "Approximate time-variable coherence analysis of multichannel signals," Multidimensional Systems and Signal Processing, vol. 13, pp. 237-264, 2002.

[77] J. L. Fernández, G. Alarcón, C. D. Binnie, and C. E. Polkey,"Comparison of sphenoidal, foramen ovale and anterior temporal placements for detecting interictal epileptiform discharges in presurgical assessment for temporal lobe epilepsy," Clin. Neurophysiol., vol. 110, pp. 895-904, 1999.

[78] P. J. Allen, G. Polizzi, K. Krakow, D. R. Fish and L. Lemieux, "Identification of EEG events in the MR scanner: the problem of pulse artifact and a method for its subtraction," NeuroImage vol. 8. pp. 229 - 239, 1998.

[79] J. Sijbers, I. Michiels and M. Verhoye "Restoration of MR-induced artifacts in simultaneously recorded MR/EEG data," Magnetic Resonance Imaging, vol. 17, No. 9, pp. 1383-1391, 1999.

[80] A. Hoffmann, L. Jager, K. J. Werhahn, M. Jaschke, S. Noachtar and M. Reiser, "Electroencephalography during functional echo-planar imaging: Detection of epileptic spikes using post-processing methods," Magnetic Resonance in Medicine, vol. 44, Issue. 5, pp. 791-798, 2000.

[81] L. Lemieux, "EEG-correlated fMRI studies of epileptic activity", Tech. Rep., Institute of Neurology, University College of London, 2001.

[82] P. J. Allen, O. Josephs and R. Turner, "A method for removing imaging artifact from continuous EEG recorded during functional MRI," Neuroimage, vol. 12, pp. 230-239, 2000.

[83] A. Cichochi and S. Amari, "Adaptive blind signal and image processing, learning algorithm and application," John Wiley and Sons, 2002.

[84] G. A. Wright, "Magnetic Resonance Imaging," IEEE Signal Processing Magazine, pp. 56-65, January, 1997.

[85] Edited by P. Jezzard, P. M. Matthews and Stephen M. Smith, "Functional MRI : an introduction to methods," Oxford: Oxford University Press, 2002.

[86] "SPM5 Manual," Functional Imaging Laboratory, Institute of Neurology, UCL, 2005.

[87] S. P. Ahlfors, G. V. Simpson, A. M. Dale, J. W. Belliveau, A. K. Liu, A. Korvenoja, J. Virtanen, M. Huotilainen, R. Tootell, H. J. Aronen and R. J. Iimoniemi, "Spatiotemporal activity of a cortical network for processing visual motion revealed by MEG and fMRI," J. Neurophysiol., vol. 82, pp. 2545-2555, 1999.

[88] C. Phillips, M. D. Rugg and K. J. Friston, "Anatomically Informed Basis Functions for EEG Source Localization: Combining Functional and Anatomical Constraints," NeuroImage, Vol. 16, pp. 678-695, 2002.

[89] F. Babiloni, C. Babiloni, F. Carducci, G. L. Romani, P. M. Rossini, L. M. Angelone, and F. Cincottia, "Multimodal integration of high-resolution EEG and functional magnetic resonance imaging data: a simulation study," NeuroImage, Vol. 19, pp. 1-5, 2003.

[90] C. Christman, C. Koeppe, D. F. Braus and H. Flora, "A simultaneous EEG and fMRI study of painful electric stimulation," NeuroImage, Vol. 34, pp. 1428-1437, 2007.

[91] B. Horwitz and D. Poeppel, "How can EEG/MEG and fMRI/PET data be combined?," Hum. Brain Mapp., vol. 17, pp. 1-3, 2002.

[92] R. J. Schilling, J. J. Carroll and A. F. Al-Ajlouni, "Approximation of nonlinear systems with radial basis function neural networks" IEEE Tran. Neural Network, vol. 12, pp. 1-15, 2001,

[93] A. Babajani and H. Soltanian-Zadeh, "Integrated MEG/EEG and fMRI Model Based on Neural Masses," IEEE Tran on Biomedical Eng., vol. 53, no. 7, 2006.

[94] L. Lemieux, A. Salek-Haddadi, O. Josephs, P. Allen, N. Toms and C. Scott, "Event-related fMRI with simultaneous and continuous EEG: description of the method and initial case report," Neuroimage, vol. 14, no. 3, pp. 780-787, 2001.

[95] A. Salek-Haddadi, M. Merschhemke, L. Lemieux and D. Fish, "Simultaneous EEG-Correlated Ictal fMRI," Neuroimage, vol. 16(1), pp. 32-40, 2002.

[96] A. Salek-Haddadi , K. J. Friston , L. Lemieux and D. R. Fish, "Studying spontaneous EEG activity with fMRI," Brain Research Reviews, vol. 43, pp.111-133, 2003.

[97] O. Josephs, R. Turner and K. J. Friston, "Event-related fMRI," Hum. Brain Mapp., vol. 5, pp. 243-248, 1997.

[98] B. Diehl, A. Salek-Haddadi, D. R. Fish and L. Lemieux, "Mapping of spikes, slow waves, and motor tasks in a patient with malformation of cortical development using simultaneous EEG and fMRI," Magn. Reson. Imaging, Vol. 21, no. 10, pp. 1167-1173, 2003.

[99] G. Fuhrmann Alpert, F. T. Sun, D. Handwerker, M. Dsposito and R. T. Knighta, "Spatio-temporal information analysis of event-related BOLD responses," Neuroimage, vol. 34, pp. 1545-1561, 2007.

[100] C. Plummer, S. Harvey and M. Cook, "EEG source localization in focal epilepsy: Where are we now?," Epilepsia, vol. 49(2), pp : 201 - 218, 2008.

[101] K. Logothetis, J. Pauls, M. Augath, T. Trinath, and A. Oeltermann, "Neurophysiological Investigation of the Basis of the FMRI Signal," Nature, vol. 412, pp. 150-157, 2001.

[102] G. Horovitz, P. Skudlarski, and J. C. Gore, "Correlations and Dissociations Between BOLD Signal and P300 Amplitude in an Auditory Oddball Task: a Parametric Approach to Combining FMRI and ERP," Magn. Reson. Imaging, vol. 20, pp. 319-325, 2002.

[103] D. H. Mathalon, S. L. Whitfield and J. M. Ford, "Anatomy of an Error: ERP and FMRI," Biol. Psychol., vol. 64, pp. 119-141, 2003.

[104] V. Calhoun and T. Adali,"Fusion of Multisubject Hemodynamic and Event-Related Potential Data Using Independent Component Analysis," IEEE International Conference on Acoustics, Speech and Signal Processing (ICASSP) Proceedings, vol. 5, pp. 14-19, May 2006.

[105] K. Friston, A. Holmes, K. Worsley, J. B. Poline, C. Frith and R. Frackowiak, "Statistical parametric maps in functional imaging: a

general linear approach," Human Brain Mapping, vol. 2, pp.189 - 210, 1995.

[106] C. J. Price and K. J. Friston,"Cognitive conjunction: a new approach to brain activation experiment," NeuroImage, vol. 5, pp. 261-270, 1997.

[107] V. D. Calhoun, M. Stevens, G. D. Pearlson and K. A. Kiehl, "FMRI analysis with the general linear model: removal of latency-induced amplitude bias by incorporation of hemodynamic derivative terms," NeuroImage, vol. 22, pp. 252 - 257, 2004.

[108] A. Morcom, S. Kiebel, R. Henson, A. Henson, J Holmes and J. B. Poline, "The general linear model and Statistical Parametric Mapping I: Introduction to the GLM", Lecture Notes of SPM course, 2005.

[109] http://www.fil.ion.ucl.ac.uk/spm/, website of Statistic Parameter Mapping (SPM).

[110] http://www.fmrib.ox.ac.uk/fsl/index.html, website of FMRIB Software Library (FSL).

[111] http://icatb.sourceforge.net/, website of Group ICA of fMRI Toolbox (GIFT).

[112] http://sccn.ucsd.edu/fmrlab/, website of FMRLAB.

[113] http://www.sph.sc.edu/comd/rorden/mricro.html, website of MRIcro.

[114] M. J. McKeown, S. Makeig, G. G. Brown, T. P. Jung, S. S. Kindermann, A. J. Bell, and T. J. Sejnowski, "Analysis of fMRI data by blind

separation into independent spatial components," Hum. Brain Map., vol. 6, no. 3, pp. 160 - 188, 1998.

[115] C. Beckmann and S. M. Smith, "Probabilistic independent component analysis for functional magnetic resonance imaging," IEEE Trans Med Imaging vol. 23, pp. 137-142, 2004.

[116] M. J. McKeown and T. J. Sejnowski, "Independent component analysis of fMRI data: Examining the assumptions," Hum. Brain Map., vol. 6, no. 5, pp. 368 - 372, 1998.

[117] M. J. McKeown, L. K. Hansen, and T. J. Sejnowsk, "Independent component analysis of functional MRI: What is signal and what is noise?," Curr. Opin. Neurobiol., vol. 13, no. 5, pp. 620-629, 2003.

[118] B. B. Biswal and J. L. Ulmer, "Blind source separation of multiple signal sources of fMRI data sets using independent component analysis," J. Comput. Assist. Tomogr., vol. 23, no. 2, pp. 265-271, 1999.

[119] K. Suzuki, T. Kiryu and T. Nakada, "Fast and precise independent component analysis for high field fMRI time series tailored using prior information on spatiotemporal structure," Hum. Brain Map., vol. 15, no. 2, pp. 407-421, 2002.

[120] V. D. Calhoun and T. Adali,"Unmixing fMRI with independent component analysis," IEEE Eng. in Medicine and Biology Magazine, pp. 79-90, March/April, 2006.

[121] V. D. Calhoun, T. Adali, G. D. Pearlson and J. J. Pekar, "Spatial and temporal independent component analysis of functional MRI data containing a pair of task-related waveforms," Human Brain Mapping, vol.13, pp. 43-53, 2001.

[122] J. R. Duann, T. P. Jung, W. J. Kuo, S. Makeig, J. C. Hsieh and T. J. Sejnowski, "Single-trial variability in event-related bold signals," NeuroImage, vol. 15, no. 4, pp. 823-835, 2002.

[123] J. Reidl, J. Starke, D. B. Omer, A. Grinvald and H. Sporsa,"Independent component analysis of high-resolution imaging data identifies distinct functional domains," NeuroImage, Vol. 34, pp. 94 - 108, 2007.

[124] D. Hu, L. Yan, Y. Liu, Z. Zhou, K. J. Friston, C. Tan, and D. Wu,"Unified SPM-ICA for fMRI analysis," NeuroImage, vol. 25, no. 3, pp. 746 - 755, 2005.

[125] W. Lu and J. C. Rajapakse "Approach and Applications of Constrained ICA", IEEE Tran. on Neural Network, vol. 16, no. 1, pp. 203 - 212, 2005.

[126] V. D. Calhoun, T. Adali, M. Stevens, K. A. Kiehl, and J. Pekar, "Semi-blind ICA of fMRI: A method for utilizing hypothesis-derived time courses in a spatial ICA analysis," NeuroImage, vol. 25, no. 2, pp. 527-538, 2005.

[127] J. V. Stone, J. Porrill, N. R. Porter, and I. D. Wilkinson, "Spatiotemporal independent component analysis of event-related FMRI data using skewed probability density functions," NeuroImage, vol. 15, no. 2, pp. 407 - 421, 2002.

[128] F. A. Galit, F. T. Sun, H. Daniel, M. Desposito and R. T. Knight, "Spatio-temporal information analysis of event-related BOLD responses," NeuroImage, vol. 34, pp. 1545 - 1561, 2007.

[129] S. LaConte, S. Strother, V. Cherkassky, J. Anderson and X. Hu, "Support vector machines for temporal classification of block design fMRI data, " NeuroImage, vol. 26, pp. 317 - 329, 2005.

[130] Z. Wang, A. R. Childress, and J. A. Detre, "Boost up the detection sensitivity of ASL perfusion fMRI through support vector machine," The 28th IEEE Engineering in Medicine and Biology Society (EMBS), pp. 1006 - 1009, Aug., 2006.

[131] Y. Fan, D. Shen and C. Davatzikos, "Detecting Cognitive States from fMRI Images by Machine Learning and Multivariate Classification," Computer Vision and Pattern Recognition Workshop, pp. 89 - 89, June 2006.

[132] Y. Ji, H. B. Liu, X. K. Wang, and Y. Y. Tang, "Cognitive states classification from fMRI data using support vector machines," Proc. Machine Learning and Cybernetics, vol 5, pp. 2919 - 2926, Aug., 2004.

[133] A. J. Bell and T. J. Sejnowski, "An information-maximization approach to blind separation and blind deconvolution," Neural Computation, vol. 7, pp. 1129 - 1159, 1995.

[134] T. W. Lee, M. Girolami and T. J. Sejnowski, "Independent Component Analysis Using an Extended Infomax Algorithm for Mixed Subgaussian and Supergaussian Sources," Neural Computation, vol. 11, pp. 417-441, 1999.

[135] S. Amari, T. P. Chen and A. Cichocki "Nonholonomic Orthogonal Learning Algorithms for Blind Source Separation," Neural Computation, vol. 12, pp. 1463-1484, 2000.

[136] V. D. Calhoun, T. Adali, and G. D. Pearlson, "Independent component analysis applied to fMRI data: A generative model for validating results," J. VLSI Signal Process. Syst., vol. 37, pp. 281 - 291, 2004.

[137] N. Correa, T. Adali, Y. Li and V. D. Calhoun, "Comparison of blind source separation algorithms for fMRI using a new matlab toolbox: GIFT," in Proc. IEEE Int. Conf. Acoustics, Speech, Signal Processing (ICASSP), Philadelphia, PA, pp. 401 - 404, 2005.

[138] Y. Li, T. Adal, V. D. Calhoun,"Estimating the number of independent components for functional magnetic resonance imaging data," Human Brain Mapping, vol. 28, Issue 11, pp. 1251-1266, November 2007.